Mathematical methods for magnetoencephalography forward and inverse modeling with enhanced spatial resolutions

Wan Jin Yeo

A dissertation
submitted in partial fulfillment of the
requirements for the degree of

Doctor of Philosophy

University of Washington

2022

Reading Committee:
J. Nathan Kutz, Chair
Samu Taulu, Chair
Marcel Den Nijs

Program Authorized to Offer Degree:
Department of Physics

University of Washington

Abstract

Mathematical methods for magnetoencephalography forward and inverse modeling with enhanced spatial resolutions

Wan Jin Yeo

Co-Chairs of the Supervisory Committee:
J. Nathan Kutz
Department of Applied Mathematics

Samu Taulu
Department of Physics

Next-generation magnetoencephalography (MEG) sensors, optically-pumped magnetometers (OPMs), can be placed closer to the head and are expected to measure signals with improved spatial resolutions. This introduces many challenges and opportunities. For one, presently-used methods for lower frequency signals, especially approximations, may now require improvements in order to adequately resolve the new signals' higher frequency components. Moreover, underlying errors may become more pronounced, since they are also measured with higher resolutions. The Nyquist sampling theorem indicates that a denser sensor array is required for OPM systems; however, this may not always be practical, hence inquiries into areas such as sensor selection are can also be opened.

In this dissertation, three mathematical considerations that may be found in each of the three contexts described above are assessed. First, we consider cubature approximations of the flux signal. Novel (near)-analytical methods of flux evaluations are developed, and the errors due to cubature approximations are evaluated. Second, we consider the effects of inaccurate boundary element head models on the signal and source localizations at varying sensor array distances. An approximate signal-to-noise ratio bound is established such that any sufficiently noiseless signal above bound will experience a noticeable effect from head

model inaccuracies. Third, we propose using the QR pivoting algorithm to determine a sparse number of optimal sensor locations, deviating from the usual strive towards denser sensor arrays. As part of establishing the theory that leads up to these three specific considerations, we also derive novel quasi-static magnetic equations that are the general forms of current equations used in MEG. From these equations, the translational non-invariances of open current segments can be observed, which leads to many implications in forward and inverse models especially when it comes to source interpretations.

TABLE OF CONTENTS

Page

List of Figures iv

Chapter 1: Introduction 1

Chapter 2: Theoretical background 5
2.1 The electro-quasi-static magnetic scalar potential and magnetic field 5
2.1.1 The far-field approximation: a simple check 8
2.1.2 An alternative form of the line integral for flat loops: an aside 9
2.2 Electromagnetism in MEG 10
2.2.1 The primary and volume currents 11
2.2.2 Geselowitz's formula 13
2.2.3 The magneto- and electro-quasi-static form of Geselowitz's formula . 14
2.2.4 Formulating the volume current as a line current 14
2.2.5 The current triangle formulation for spherical head models 16
2.2.6 Sarvas' formula 17

Chapter 3: The translational non-invariance of magnetic contributions by open current segments 18
3.1 Effects of origin translations in the magnetic forward problem 18
3.1.1 Translational invariance of $U(\mathbf{r})$ and $\mathbf{B}(\mathbf{r})$ for closed current loops . . 19
3.1.2 Translational non-invariance of $u(\mathbf{r})$ and $\mathbf{b}(\mathbf{r})$ for open current segments 20
3.1.3 Verification of the translational non-invariance of $\tilde{u}(\tilde{\mathbf{r}})$ 21
3.1.4 Translational invariance of the electric forward problem: an aside . . 22
3.2 Effect on ECD inverse models 25
3.2.1 Validity of ECD fits 26
3.2.2 Verification of the validity of ECD fits 27
3.2.3 Unconstrained ECD fit procedure 29

3.2.4 Results . . . 32
3.2.5 Origins in the plane of the current triangle . . . 34
3.3 Further discussions into the implications in MEG methods . . . 35
3.3.1 Assigning physical meaning to current segments . . . 35
3.3.2 Co-registration errors and mitigations . . . 38
3.3.3 Sensor orientations . . . 40

Chapter 4: Near-analytical magnetic flux calculations . . . 41
4.1 Vector spherical harmonic expansion of the magnetic field . . . 42
4.1.1 Magnetic flux through planar pick-up loops . . . 44
4.1.2 Volumetric magnetic flux through cylindrical sensing volumes . . . 47
4.2 Higher l degree portions correspond to higher spatial frequency bands . . . 48
4.2.1 Improved forward and inverse models . . . 50
4.2.2 Analytical first-order multipole moment errors: an aside . . . 52
4.3 Line integral formula for an arbitrary sensor geometry . . . 54
4.3.1 Rectangular/square sensors . . . 57
4.3.2 Circular sensors . . . 58
4.4 Analytical recursion formula for tangential circular sensors . . . 59
4.5 Passive rotations of vector fields . . . 62
4.5.1 Passive rotation of v_{lm} for tangential circular sensors along z-axis . . . 63
4.6 Nonzero v_{lm} terms for tangential square sensors along the z-axis . . . 64
4.7 Cubature approximation errors . . . 66
4.7.1 Errors for each l degree . . . 67
4.7.2 Varying sensor distances . . . 68
4.7.3 Varying sensor sizes . . . 69
4.7.4 Comments . . . 70
4.8 Cylindrical harmonics . . . 71

Chapter 5: Effects of inaccurate head models on forward and inverse model accuracies 74
5.1 Boundary Element Method overview . . . 75
5.1.1 Triangularizing the head model . . . 76
5.1.2 Linearization of discretized electric potentials . . . 77
5.1.3 Matrix deflation . . . 79

5.1.4 Discretization of the magnetic field . . . 81
5.2 Subspace angle as a signal error and spatial complexity measure . . . 82
5.3 BEM simulation results . . . 84
5.3.1 Simulation setup . . . 84
5.3.2 Total signal error at varying sensor array distances . . . 85
5.3.3 The signal error portion and its spatial complexity . . . 89
5.3.4 Source localization and orientation errors . . . 90
5.4 Analytical first-order errors for CC BEM: an aside . . . 97
5.4.1 Perturbations to mesh vertices . . . 97
5.4.2 Perturbations to conductivity . . . 99

Chapter 6: Near-optimal sensor selection . . . 101
6.1 Problem statement . . . 103
6.2 Low-rank subspaces and SVD . . . 104
6.3 Coefficient estimation and signal reconstruction . . . 106
6.4 QR pivoting algorithm . . . 107
6.5 Signal reconstruction and source localization using QR-selected sensors . . . 110
6.5.1 2000 nAm and 200 nAm phantom signals . . . 111
6.5.2 Using 2000 nAm basis for 200 nAm signal . . . 118
6.5.3 Sensor selection on binaural stimulation signal . . . 120
6.6 Limitations and further comments . . . 121

Chapter 7: Conclusion . . . 124

LIST OF FIGURES

Figure Number Page

1.1 General setup of SQUID and OPM sensor arrays. The former resides within a dewar and is a few centimeters from the head, whereas the latter can be placed directly on the head. 3

3.1 Illustration on how an open current segment has a non-invariant magnetic scalar potential and magnetic field when different origins are chosen. In the coordinate system with origin O, the current segment is non-radial and hence not magnetically silent. However, with respect to the translated origin O', the current segment becomes radial and is magnetically silent because $d\mathbf{L}' = 0$ when $\mathbf{r}'$ is parallel to $d\mathbf{l}'$. 22

3.2 (Left) Current triangle setup and the 12 computational origins considered. (Right) Show the varying $\tilde{u}_i(\tilde{\mathbf{r}})$ contribution by each line segment of the current triangle at various origins. Each edge and their corresponding $\tilde{u}_i(\tilde{\mathbf{r}})$ contributions have matching colors. Only non-radial current segments have non-zero contributions. The magenta line shows the translationally invariant $U(\mathbf{r})$ of the closed loop. 23

3.3 Shows the maximum ECD GOF attainable at each origin point that lies along an arbitrary current triangle when the dipole solutions are constrained to be parallel along the triangle edges. When the origin coincides with a triangle vertex, the dipole with maximum GOF lies approximately at the middle of the opposite edge. Each vertex origin is marked by an "x", and the ECD location is marked by a solid circle with matching color. 29

3.4 (Left) Magnetometer sensor array setup and current triangle configuration used for the unconstrained exhaustive ECD search. (Right) Unconstrained ECD fit results when the origin choice coincides with one of the triangle vertices. Each of the three origins is marked by an "x", and the corresponding ECD fit result is marked by a solid square with matching color. The center of each triangle edge is marked by a hollow circle. The unconstrained fits shown here are in agreement with the constrained fits shown in Figure 3.3. 30

3.5 LE_{ECD} and GOF_{ECD} plots for the ECD fits at various origin choices. The current triangle had vertices at $(0, 0, 0)$ cm and $(\pm 0.25, 0, 3.3)$ cm on the xz plane. LE increases when the origin choice is further from the $(0, 0, 0)$ cm origin, but GOF is high for all origins in the xz plane, especially in areas near the triangle vertices. GOF falls off much quicker for origin translations in directions perpendicular to the triangle plane. LE is comparable for origin translations of the same amount in both the xz plane and the xy plane. . . . 33

3.6 For all origins that lie in the current triangle plane, the distance between the origin and ECD fit, $||\mathbf{r}'_{ECD,i} - \mathbf{r}_{origin,i}||$, is inversely proportional to the norm of the ECD moment projected onto the line perpendicular to $\mathbf{r}'_{ECD,i} - \mathbf{r}_{origin,i}$. Since all of these fits have high GOF, it implies there for every origin in the original current triangle's plane, there exists an equivalent current triangle with two radial edges and equivalent surface area that reproduces the reference signal. 36

3.7 (First row) Illustrates two magnetically-silent radial volume current edges being introduced in a spherical head model to form a closed current loop with the primary current. This is equivalent to a translated origin case where all edges are now non-radial; all three edges now have non-zero signal contributions. (Second, third rows) Deep and near-radial current sources are more sensitive to co-registration errors respectively; a small origin translation is sufficient to render them radial and magnetically silent. 39

4.1 Plots of the real part of spherical harmonic modes Y_{lm} on a sphere, from degrees $l = 1$ to $l = 4$. Higher l degree subspaces correspond to higher spatial frequencies, since the orthonormal m-order basis modes that span the space are more spatially complex. 49

4.2 (Top row) Topographic plots of l-degree signal RE due to tangentially-displaced dipole positions. The original dipole position corresponds to the center of the xy plane. (Bottom row) Areas of convergence for RE ≤ 0.8. For higher l degrees, the steepness of descent into the true solution increases, corresponding to a smaller area of convergence. 53

4.3 Plots of $v_{32,m}$ terms for: (a) a tangential square sensor, and (b) a tangential circular sensor, both on the z-axis. For the square sensor, $v_{32,m} \neq 0$ only when m is a multiple of 4, including $m = 0$. For the circular sensor, $v_{32,0}$ is nonzero. 66

4.4 Relative error plots of $v_{l,0}$ for a (a) tangential square sensor and (b) tangential circular sensor, both located on the z-axis. The errors increase as l increases, which means that cubature approximations of higher frequency signal portions become increasingly inaccurate. Fewer sampling points result in larger errors as well. 68

4.5 Relative error plots of $v_{8,0}$ for a (a) tangential square sensor and (b) tangential circular sensor with varying distances from the origin, both located on the z-axis. The error of l degree signal portions increase as the sensor is placed closer to the origin. 70

4.6 Relative error plots of $v_{8,0}$ for a (a) tangential square sensor and (b) tangential circular sensor with varying sensor sizes. The errors increase as side length increases, since the sampling points are further apart and hence resolve the given spatial frequency component with decreased accuracies. 71

5.1 The BEM setup: the blue mesh shows a triangulated sphere of radius 9 cm that has its vertices randomly perturbed by up to 10%, and the red arrow shows a dipolar source located at $(6, 0, 0)$ cm. A spherical sensor array of radius 10 cm with 324 randomly-oriented square pick-up loops is also shown. 86

5.2 In the noiseless case, the subspace angle between $\boldsymbol{\phi}$ and $\boldsymbol{\phi}'$ decreases as sensor array distances increase. Signals measured by distant sensor arrays are thus less impacted by head model inaccuracies. Also, as mesh perturbations increase, the subspace angle increases as expected. 87

5.3 Plots of $\boldsymbol{\phi}$, $\boldsymbol{\phi}'$, and $\delta\boldsymbol{\phi} = \boldsymbol{\phi}' - \boldsymbol{\phi}$ for the following setups: (first row) the 2 cm source, a 10% mesh perturbation, and varying sensor array distances from 10 cm to 15 cm, and (second row) the 2 cm source, the 10 cm sensor array, and varying mesh perturbations from 0% to 10%. As sensor array distance increases, signal error decreases for the same amount of mesh perturbation. As mesh perturbations increase, signal errors increase. 88

5.4 A plot of the volume-to-primary current contributions towards the total signal measured with the 10 cm sensor array for a 10% mesh perturbation. The values are higher for the 2 cm and 8 cm sources than the 4 cm and 6 cm sources, resulting in higher total signal errors as shown in Figure 5.2. 89

5.5 (Top row) The total signal $\boldsymbol{\phi}$ can be explained well with a $L = 12$ degree truncation of $\mathbf{S}_{1:L}$ for all source distances. (Bottom row) The signal error portion $\delta\boldsymbol{\phi}$ due to a 10% mesh perturbation are higher and requires a higher L degree truncation to explain than $\boldsymbol{\phi}$. This means $\delta\boldsymbol{\phi}$ have higher higher spatial complexities than $\boldsymbol{\phi}$, and the higher spatial frequency components of signals are more sensitive to head model inaccuracies. Closer sensor distances also have higher subspace angles, corresponding to increased signal errors in agreement with Figure 5.2. 91

5.6 ECD fit results for a 2 cm source case. (Left column) The position and orientation errors of the ECD fit for the noiseless signal case. Closer sensor arrays have increased errors, agreeing with the behavior of the noiseless signal error itself. (Middle column) For a noise level of SNR $\approx$ 6 dB, ECD fit errors start to increase slightly for increased sensor array distances, indicating that the improved localization made possible with higher SNR is starting to outweigh the the poorer localization due to more inaccurate noiseless signals. (Right column) For a 20 fT constant noise level (above 6 dB), ECD fit errors decrease for decreased sensor array distances. The effect of higher SNR has now fully outweighed the effects of the increased noiseless signal error. 93

5.7 ECD fit results for a 4 cm source case. The description of this figure is similar to Figure 5.6. 94

5.8 ECD fit results for a 6 cm source case. The description of this figure is similar to Figure 5.6. 95

5.9 ECD fit results for a 8 cm source case. The description of this figure is similar to Figure 5.6. 96

6.1 (Green arrows) Usual pipeline for signal reconstruction and source localization that utilizes the entire sensor array. (Blue arrows) Proposed pipeline for full-state signal reconstruction and source localization with sparse sampling. Principled sensor selection can be done using QR pivoting on a low-dimensional SVD basis representation of a prior/simulated dataset. $\mathbf{x}$ denotes the full-state signal measurement, $\mathbf{\Phi}$ denotes the rank-r truncated left singular SVD basis of $\mathbf{x}$, $\hat{\mathbf{a}}$ denotes corresponding the (noisy) coefficients of $\mathbf{\Phi}$, and $\mathbf{P}$ (obtained from $\mathbf{P}'$) denotes the permutation matrix that selects rows of $\mathbf{\Phi}$. 103

6.2 All curves are averaged over the 32 phantom dipolar source results. (a) Plots for the 200 nAm case. The dashed red curve shows the singular value spectrum, and the solid black curve shows the RE of the reconstructed signals. The elbow of the singular value spectrum occurs at approximately 2-10 modes, with agrees with the minimum range of the RE curve. The RE curve increases afterwards, peaking at around 35 modes, before decreasing again. The blue dotted curve shows the RE when the 2000 nAm SVD basis was used for signal reconstruction. Again, low RE is observed between 2-10 modes before it increases, this time peaking much higher at a value above 35 modes. (b) Plots for the 2000 nAm case. The behavior of the curves are similar to the 200 nAm case. 112

6.3 Image plots of the original signal (left column) and reconstructed signal (middle column) for a (-5.97,0,2.29) cm, 200 nAm phantom dipolar source. The 2-mode 2-sensor QR reconstruction has similar performance to the 2-mode 306-sensor SVD reconstruction, indicating the redundancy of dense sensor arrays. (Right column) Plots of the first 2 SVD modes. The first mode captures most of the spatiotemporal dynamics of the original signal, showing how low-dimensional signals only have a few significant and informative modes. 114

6.4 (a) Original signals for each of the 200 nAm 32 phantom dipolar sources. (b) 2-mode QR reconstructed signals, with the 2 selected sensors indicated by the red dots. There is a high reconstruction accuracy of the signal patterns, and sensor selection appears to be source-dependent, with at least one always being selected close to the source activity. 116

6.5 (a) Original signals for each of the 2000 nAm 32 phantom dipolar sources. Note the more distinct dipolar field patterns due to the higher SNR. (b) 2-mode QR reconstructed signals, with the 2 selected sensors indicated by the red dots. There is a very high reconstruction accuracy of the signal patterns, and the selected sensors are nearly all identical for sources with the same tangential coordinates but at different depths. 117

6.6 Position errors (left) and orientation errors (right) of ECD fits using various reconstructed 200 nAm signals. All cases except when using 2000 nAm basis had higher localization errors for deep sources, especially the 35-mode QR case, indicating that using more modes/sensors does not guarantee better performance. For more superficial sources, all cases including the 2-mode QR case had similar localization performance, indicating a redundancy in sensors. 118

6.7 Position errors (left) and orientation errors (right) of ECD fits using 2000 nAm signals. All cases performed identically well due to the high SNR. 119

6.8 (a) RE plot for the p-mode reconstructed binaural signal (black curve), and the singular value plot of the full-state data (red curve). The RE plot follows the singular value spectrum, indicating that the number of modes/sensors can be selected from the latter. (b) Superior (left) and posterior (right) views of the head MRI. The ECD result using the full 274-sensor original signal (red) and 30-mode QR reconstructed signal (green) are shown. The performances are near-identical with a 1.41 mm and 0.80° discrepancy, indicating sensor redundancy. 122

ACKNOWLEDGMENTS

First and foremost, I would like to thank my advisors Samu Taulu and Nathan Kutz.

Samu introduced me to the fascinating field of magnetoencephalography three years ago. I could not have asked for a more patient and kinder mentor to help me navigate through this field. He has been extremely encouraging towards any new ideas I propose (no matter how silly) and has always shown genuine interest in developing those ideas with me. He has also influenced the way I approach problems through our weekly meetings where we parse out research problems.

Nathan, with his infectious optimism and collaborative nature, has influenced me to analyze problems more holistically. The lively and fruitful meetings with him are a respite from work; I have never left a meeting with him not feeling motivated and energized. He has also always been incredibly supportive of my work and is eager to help whenever I get stuck on something.

I would also like to thank my committee for their constructive feedback during the general and final exams: Geoffrey Boynton, Marcel den Nijs, Shih-Chieh Hsu, Adrian KC Lee, and Paul Wiggins.

A big thank you to all the collaborators and colleagues whom I have had the joy of working with: Eric Larson, Yao-Rui Yeo, Joonas Iivanainen, Peter Schwindt, Julia Stephen, Jim McKay, Amir Borna, Aaron Miller, Gonzalo Ferrandez Quinto, and Eardi Lila.

I would like to thank all my friends here in graduate school. It is sad to part ways, but I am comforted knowing that I have made lifelong friends.

Last but not least, thank you to my family for always being there.

DEDICATION

To my family.

Chapter 1

INTRODUCTION

The human brain, with its billions of neurons and trillions of inter-neuronal connections [67, 68, 131], is undoubtedly the most complex organ of the human body. The way it processes the vast amounts of information it receives constantly still eludes us for the most part. In an attempt to decode the mysteries of brain processing, numerous functional imaging methods have been developed to detect measurable indicators of brain activity. Some of these methods include functional magnetic resonance imaging (fMRI) [50, 97], position emission tomography (PET) [7, 109, 115], functional near-infrared spectroscopy (fNIS) [41, 96], electroencephalography (EEG) [89, 145], and magnetoencephalography (MEG) [24, 59, 63, 77].

This dissertation focuses on MEG, which is a non-invasive method of detecting the magnetic fields above the head produced by the electric currents of brain activity. The signal measured is then used to infer the underlying brain activity locations and spatiotemporal dynamics via inverse models [28, 29, 43–46, 60, 102, 106, 107, 117, 130, 151, 152]. These inverse models are non-unique [66] and hence pose many complications in obtaining reliable results. However, with the help of forward models that construct the signal, an understanding of the behavior and useful decompositions of the signal allows us to apply reasonable inverse model constraints for more accurate results. This dissertation primarily discusses the mathematical techniques used in the forward calculations of MEG signals. As we will discuss shortly, the advancement of instrumentation that allow for higher-resolution signals to be measured calls for the re-examination of the validity and accuracy of these mathematical methods when used for these signals.

The magnetic fields produced by the brain are extremely weak, and are on the order

of femtoteslas in the region immediately outside the head [17, 21, 59]. Sensors with high sensitivities are thus required to discernibly pick up these signals. Superconducting quantum interference devices (SQUID) are an example of sensors with sufficiently high sensitivity [24, 91], and is currently the most widely-employed sensor type. The signal measured by a SQUID sensor is the magnetic flux through a flat pick-up loop. In order to maintain its superconducting state, SQUIDs must be operated at cryogenic temperatures and are thus confined within dewars containing liquid helium (boiling point of around 4 K). The necessity of these thick-walled dewars to insulate the head from the liquid helium renders the closest possible distance between SQUID sensors and the scalp to be around 2 cm [74]. As will be elaborated in Section 4.2, this distance between the sensors and the head/neural activity is a factor that compromises the detection of high spatial resolution signals. The spatially complex components of the weak magnetic fields decay quickly as a function of distance to below either the sensing capabilities of the sensor, or sensor noise levels.

Recently, advancements have been made in developing another viable sensor candidate, namely, optically pumped magnetometers (OPM) [4, 11, 14, 70, 74, 85, 87, 90, 126, 146, 157]. As opposed to a SQUID sensor, the signal measured by an OPM is the total magnetic field within a cylindrical sensing volume along some sensing direction. OPMs are able to operate at room temperatures and thus may be placed directly on the scalp without causing harm to the subject; its reduced distance to the head/neural activity allows for the detection of signals with higher spatial resolutions. This improvement in signal resolution, in addition to the perpetual strive towards improving sensor sensitivities for increased signal-to-noise ratios (SNR), mean that current methods that utilize approximationsor coarse-grained approaches may need to be revised in order to resolve the now-detectable high spatial frequency signal components. Only then can the additional information provided by these high-resolution signals be fully harnessed for improved signal reconstructions and inverse models. New challenges or capabilities that arise from this new technology may also warrant the development of new methods. For instance, OPMs have the flexibility of placing sensors anywhere on the head (as opposed SQUID sensor arrays which are rigid); it may thus be advantageous to further the area of

MEG sensor design.

Figure 1.1 shows the general setup of SQUID (left) and OPM (right) sensor arrays. It is inspired by Figure 1 of [82]. The MRI image of the head is generated using Brainstorm [141].

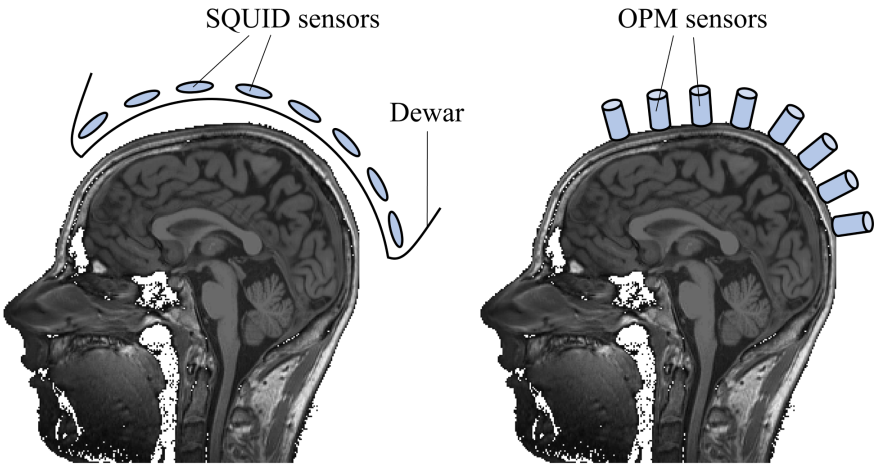

Figure 1.1: General setup of SQUID and OPM sensor arrays. The former resides within a dewar and is a few centimeters from the head, whereas the latter can be placed directly on the head.

The organization of this dissertation is as follows. In Chapter 2, the overarching electromagnetic theory in MEG is presented. A novel form of the quasi-static magnetic scalar potential and magnetic field are derived, and they are shown to be the generalized forms of equations that are presently used in the field of MEG. This is under the widely-made assumption that neural activity can be modeled as a current loop; we offer a quantitative justification that this assumption is valid.

In our generalized derivation of the magnetic field, a previously unreported source of forward and inverse model interpretation error is also revealed – computational origin choice. Our formalism indicates that open current segment contributions to the magnetic scalar potential and magnetic field are translationally non-invariant. This leads to non-unique forward and inverse models in different origin choices, which may have extensive implications in the fundamental interpretations and implementations of common MEG methods, as

discussed in Chapter 3.

After the electromagnetic background for MEG is established, three specific topics that may face potential issues associated with next-generation OPM sensor arrays and its improved signal resolutions are considered.

First, cubature approximations that are presently used for flux calculations are discussed in Chapter 4. Analytical forms to calculate the signal contributions from individual spatial frequency bands are formulated so that one may have near-analytical evaluations of the magnetic flux to arbitrary accuracy. This was then used to assess the errors of cubature approximations in the context of closer sensor arrays and higher resolution signals.

Next, in Chapter 5, we study how head model inaccuracies may affect signal reconstruction and source localization accuracies when sensor arrays are placed closer to the head. This was done in the boundary element method (BEM) framework, via perturbing a spherical head model to varying degrees and calculating the errors at varying sensor array distances.

Finally, we propose the use of a data-driven sparse sensor selection algorithm in Chapter 6, specifically for cases of focal neural sources that result in signals exhibiting latent low-dimensional spatiotemporal dynamics. This algorithm involves the QR pivoted factorization on the singular value decomposition (SVD) basis of the signal. Since OPMs allows for the flexible placement of sensors, this approach may be helpful for sparse MEG sensor array designs. It is also a deviation from perceptions driven by the Nyquist sampling theorem, which suggest that sensor array densities should increase to resolve higher spatial resolutions signals.

In Chapter 7, we conclude by summarizing the findings presented in this dissertation, and discuss future directions. Note that in between each chapter, the notations are re-set and re-defined; the only exception is between Chapters 2 and 3.

Chapter 2

THEORETICAL BACKGROUND

We first derive general expressions for the electro-quasi-static magnetic scalar potential and magnetic field in a source-less region. In Section 2.2, their validity for use in the context of MEG will be elaborated.

2.1 The electro-quasi-static magnetic scalar potential and magnetic field

The magnetic field due to a steady current flow with amplitude I along a closed loop $\mathcal{C}$ is given by the Biot-Savart law

$$\mathbf{B}(\mathbf{r}) = \frac{\mu_0}{4\pi} \int_{\mathcal{C}} \frac{I d\mathbf{l}' \times (\mathbf{r} - \mathbf{r}')}{|\mathbf{r} - \mathbf{r}'|^3}, \tag{2.1}$$

where $\mathbf{r} = (r_x, r_y, r_z)$ is the field point, $\mathbf{r}' = (r'_x, r'_y, r'_z)$ are source points along $\mathcal{C}$, and μ_0 is the vacuum permeability. Under the electro-quasi-static approximation, i.e., setting $\partial\mathbf{E}/\partial t = \mathbf{0}$, the curl of the magnetic field satisfies

$$\boldsymbol{\nabla} \times \mathbf{B}(\mathbf{r}) = \mathbf{0} \tag{2.2}$$

in any source-free region where $\mathbf{J} = 0$ due to Ampere's law. This allows us to write $\mathbf{B}$ as the gradient of a magnetic scalar potential U,

$$\mathbf{B}(\mathbf{r}) = -\mu_0 \boldsymbol{\nabla} U(\mathbf{r}). \tag{2.3}$$

Note that the Biot-Savart law does not strictly apply to closed current loops (see, e.g., [55, 80, 116, 159] for further treatments and discussions of the Biot-Savart law). However, since we want it to hold true simultaneously with Ampere's law, which requires a closed

current loop, we have defined the Biot-Savart law (2.1) from the start with a closed loop $\mathcal{C}$ for convenience.

The additional condition of a curl-less magnetic field (2.2) allows us to rewrite the Biot-Savart law via the gradient theorem as follows (this is a strategy used by Sarvas in [127] as well). Assuming $\mathbf{B}(\mathbf{r})$ is smooth (i.e. no change in permeability), (2.2) indicates that $\mathbf{B}(\mathbf{r})$ is conservative. Since $\mathbf{B}(\mathbf{r})$ is (proportional to) the gradient of $U(\mathbf{r})$, we may arbitrarily choose a path to integrate over it in the gradient theorem to obtain $U(\mathbf{r})$. For convenience, let us integrate along the radial path along $\mathbf{e}_r = \mathbf{r}/||\mathbf{r}|| \equiv \mathbf{r}/r$. This leads to

$$U(\mathbf{r}) = -\int_0^\infty \boldsymbol{\nabla} U(\mathbf{r} + t\mathbf{e}_r) \cdot \mathbf{e}_r \, dt \tag{2.4}$$

$$= \frac{1}{\mu_0} \int_0^\infty \mathbf{B}(\mathbf{r} + t\mathbf{e}_r) \cdot \mathbf{e}_r \, dt. \tag{2.5}$$

Substituting in Biot-Savart law (2.1) gives

$$\begin{aligned} U(\mathbf{r}) &= \frac{I}{4\pi} \int_0^\infty \int_{\mathcal{C}} \frac{d\mathbf{l}' \times (\mathbf{r} + t\mathbf{e}_r - \mathbf{r}') \cdot \mathbf{e}_r}{|\mathbf{r} + t\mathbf{e}_r - \mathbf{r}'|^3} \, dt \\ &= \frac{I}{4\pi} \int_0^\infty \int_{\mathcal{C}} \frac{(\mathbf{r} - \mathbf{r}') \times \mathbf{e}_r \cdot d\mathbf{l}'}{|\mathbf{r} + t\mathbf{e}_r - \mathbf{r}'|^3} \, dt \qquad (2.6) \\ &= \frac{I}{4\pi} \int_{\mathcal{C}} (\mathbf{r}' \times d\mathbf{l}' \cdot \mathbf{e}_r) \int_0^\infty \frac{dt}{|\mathbf{r} + t\mathbf{e}_r - \mathbf{r}'|^3}, \qquad (2.7) \end{aligned}$$

where we have used the scalar triple product to simplify the expressions in the second and third equalities. Let $\mathbf{a} = \mathbf{r} - \mathbf{r}'$, $k = \mathbf{a} \cdot \mathbf{e}_r$ and $y = t + k$. Then $dy = dt$ and we have

$$\int_0^\infty \frac{dt}{|\mathbf{r} + t\mathbf{e}_r - \mathbf{r}'|^3} = \int_k^\infty \frac{dy}{(y^2 + a^2 - k^2)^{3/2}} = \frac{1}{a(a+k)}. \tag{2.8}$$

If we further define the quantities

$$F(\mathbf{r},\mathbf{r}') \equiv a(ra + \mathbf{a}\cdot\mathbf{r}) \tag{2.9}$$

$$\boldsymbol{\nabla} F(\mathbf{r},\mathbf{r}') = \left(\frac{a^2}{r} + \frac{\mathbf{a}\cdot\mathbf{r}}{a} + 2a + 2r\right)\mathbf{r} - \left(a + 2r + \frac{\mathbf{a}\cdot\mathbf{r}}{a}\right)\mathbf{r}', \tag{2.10}$$

which are chosen for consistency of notation with Sarvas [127], then we see that (2.8) is equivalently

$$\frac{1}{a(a+k)} = \frac{r}{F(\mathbf{r},\mathbf{r}')}. \tag{2.11}$$

Finally, if we define $d\mathbf{L}' \equiv -I(\mathbf{r}'\times d\mathbf{l}')$, then the magnetic scalar potential may now be written as

$$U(\mathbf{r}) = -\frac{1}{4\pi}\int_{\mathcal{C}} \frac{d\mathbf{L}'\cdot\mathbf{r}}{F(\mathbf{r},\mathbf{r}')}. \tag{2.12}$$

The magnetic field $\mathbf{B}$ can be obtained via (2.3),

$$\mathbf{B}(\mathbf{r}) = \frac{\mu_0}{4\pi}\int_{\mathcal{C}} d\mathbf{L}'\cdot\boldsymbol{\nabla}\left[\frac{\mathbf{r}}{F(\mathbf{r},\mathbf{r}')}\right], \tag{2.13}$$

where the gradient is taken with respect to $\mathbf{r}$. The gradient portion is a 3×3 Jacobian matrix, with entries defined as

$$\begin{aligned}\left\{\boldsymbol{\nabla}\left[\frac{\mathbf{r}}{F(\mathbf{r},\mathbf{r}')}\right]\right\}_{i,j} &= \frac{\partial_{r_j} r_i}{F(\mathbf{r},\mathbf{r}')} + r_i\partial_{r_j}\left(\frac{1}{F(\mathbf{r},\mathbf{r}')}\right) \\ &= \frac{\delta_{ij}}{F(\mathbf{r},\mathbf{r}')} - \frac{r_i\partial_{r_j}F(\mathbf{r},\mathbf{r}')}{F^2(\mathbf{r},\mathbf{r}')},\end{aligned} \tag{2.14}$$

where $i,j,= x,y,z$, and δ_{ij} is the Kronecker delta function. Thus,

$$B_j(\mathbf{r}) = \frac{\mu_0}{4\pi}\int_{\mathcal{C}}\sum_i dL_i'\left[\frac{\delta_{ij}}{F(\mathbf{r},\mathbf{r}')} - \frac{r_i\partial_{r_j}F(\mathbf{r},\mathbf{r}')}{F^2(\mathbf{r},\mathbf{r}')}\right],$$

i.e.,

$$\mathbf{B}(\mathbf{r}) = \frac{\mu_0}{4\pi} \int_{\mathcal{C}} d\mathbf{L}' \cdot \left[\frac{\mathbb{I}}{F(\mathbf{r}, \mathbf{r}')} - \frac{\mathbf{r} \boldsymbol{\nabla} F(\mathbf{r}, \mathbf{r}')}{F^2(\mathbf{r}, \mathbf{r}')} \right]. \tag{2.15}$$

To our knowledge, equations (2.12) and (2.15) are novel.

In both equations, $d\mathbf{L}'$ indicates that whenever segments of $\mathcal{C}$ have $\mathbf{r}'$ parallel to $d\mathbf{l}'$, then $U(\mathbf{r}) = 0$ and $\mathbf{B}(\mathbf{r}) = \mathbf{0}$. In other words, straight line current segments that are radial with respect to the origin have zero field contribution. Only non-radial components of a current loop have nonzero contributions to the $U(\mathbf{r})$ and $\mathbf{B}(\mathbf{r})$ fields. This observation has implications in MEG forward and inverse model interpretations, as we will see in Chapter 3. We also note that the same conclusion can be reached via an expansion of the magnetic field using vector spherical harmonics (VSH) [143], which will be seen later on in Section 4.1.

2.1.1 The far-field approximation: a simple check

As a simple check for correctness, we show that in the far-field approximation, (2.12) and (2.15) reduce to the expected expressions for a magnetic dipole. First, note that the vector area $\mathbf{K}$ is defined

$$\mathbf{K} = -\frac{1}{2I} \int_{\mathcal{C}} d\mathbf{L}', \tag{2.16}$$

and that the magnetic dipole moment is $\mathbf{m} = I\mathbf{K}$. When $|\mathbf{r}| >> |\mathbf{r}'|$, we see that (2.9) and (2.10) are approximately

$$F(\mathbf{r}, \mathbf{r}') \approx 2r^3 \tag{2.17}$$

$$\boldsymbol{\nabla} F(\mathbf{r}, \mathbf{r}') \approx 6r\mathbf{r}. \tag{2.18}$$

By substituting the above into (2.12) and (2.15), it is easy to see that in the far-field region, they are approximately

$$U(\mathbf{r}) \approx \frac{1}{4\pi}\frac{\mathbf{m}\cdot\hat{\mathbf{r}}}{r^2} \tag{2.19}$$

and

$$\mathbf{B}(\mathbf{r}) \approx -\frac{\mu_0}{4\pi}\frac{1}{r^3}\left[3(\mathbf{m}\cdot\hat{\mathbf{r}})\hat{\mathbf{r}} - \mathbf{m}\right] \tag{2.20}$$

respectively, as desired.

2.1.2 An alternative form of the line integral for flat loops: an aside

As an aside here, we also show that in the case where the closed loop is flat and the origin is in the plane of the loop, equations (2.12) and (2.15) can be written as an equivalent line integral that is integrated with respect to outward pointing vectors of the loop (not necessarily normal), instead of along its tangential direction. This is an extension to a similar current setup considered in Figure 3.3(f) of [63].

Let us denote the area unit normal vector of the flat loop to be $\mathbf{n}_A$. Green's theorem tells us that (2.12) may be written as

$$U(\mathbf{r}) = \frac{I}{4\pi}\iint_{A_\mathcal{C}} \boldsymbol{\nabla}' \times \left[\frac{\mathbf{r}\times\mathbf{r}'}{F(\mathbf{r},\mathbf{r}')}\right]\cdot\mathbf{n}_A \, dA, \tag{2.21}$$

where $\boldsymbol{\nabla}'$ acts only on the primed coordinates, and $A_\mathcal{C}$ denotes the area enclosed by the closed loop $\mathcal{C}$. Using the vector identity $\boldsymbol{\nabla}'(\mathbf{x}\times\mathbf{y}) = \mathbf{x}(\boldsymbol{\nabla}'\cdot\mathbf{y}) - \mathbf{y}(\boldsymbol{\nabla}'\cdot\mathbf{x}) + (\mathbf{y}\cdot\boldsymbol{\nabla}')\mathbf{x} - (\mathbf{x}\cdot\boldsymbol{\nabla}')\mathbf{y}$ with $\mathbf{x} = \mathbf{r}$ and $\mathbf{y} = \mathbf{r}'/F(\mathbf{r},\mathbf{r}')$, we have

$$U(\mathbf{r}) = \frac{I}{4\pi}\iint_{A_\mathcal{C}} \left\{(\mathbf{r}\cdot\mathbf{n}_A)\boldsymbol{\nabla}'\cdot\left(\frac{\mathbf{r}'}{F(\mathbf{r},\mathbf{r}')}\right) - \left[(\mathbf{r}\cdot\boldsymbol{\nabla}')\frac{\mathbf{r}'}{F(\mathbf{r},\mathbf{r}')}\right]\cdot\mathbf{n}_A\right\} \, dA. \tag{2.22}$$

If the origin is in the plane of the loop, i.e. if $\mathbf{n}_A\cdot\mathbf{r}' = 0$, then the second term in the integrand vanishes. This may be seen from applying the the product rule $(d\mathbf{x})\cdot\mathbf{y} = d(\mathbf{x}\cdot\mathbf{y}) - (d\mathbf{y})\cdot\mathbf{x}$,

with $\mathbf{x} = \mathbf{r}'/F(\mathbf{r},\mathbf{r}')$ and $\mathbf{y} = \mathbf{n}_A$. The above equation thus becomes

$$U(\mathbf{r}) = \frac{I}{4\pi}(\mathbf{r}\cdot\mathbf{n}_A)\iint \boldsymbol{\nabla}'\cdot\left(\frac{\mathbf{r}'}{F(\mathbf{r},\mathbf{r}')}\right)\,dA, \tag{2.23}$$

and the 2D divergence theorem tells us that it may again be reverted into a line integral

$$U(\mathbf{r}) = \frac{I}{4\pi}(\mathbf{r}\cdot\mathbf{n}_A)\int_{\mathcal{C}}\frac{\mathbf{r}'}{F(\mathbf{r},\mathbf{r}')}\cdot\mathbf{n}_l\,dl', \tag{2.24}$$

where $\mathbf{n}_l$ is the outward pointing normal along the loop. By taking the gradient of this magnetic scalar potential expression, we finally obtain the magnetic field,

$$\mathbf{B}(\mathbf{r}) = -\frac{\mu_0 I}{4\pi}\int_{\mathcal{C}}(\mathbf{r}'\cdot\mathbf{n}_l)\boldsymbol{\nabla}\left(\frac{\mathbf{r}}{F(\mathbf{r},\mathbf{r}')}\right)\cdot\mathbf{n}_A\,dl', \tag{2.25}$$

where the gradient in the integrand is given by (2.14). We see that when $\mathbf{r}'$ is perpendicular to $\mathbf{n}_l$, i.e. when the current segment is radial, then $\mathbf{B}$ vanishes. This is consistent with what is expected from (2.15).

Note that (2.23) implies that loop-preserving transformations of the parametrization, $\mathbf{r}' \to \mathbf{r}' + F(\mathbf{r},\mathbf{r}')\boldsymbol{\nabla}\times\mathbf{z}$ where $\mathbf{z}$ is some arbitrary vector field, yields an invariant magnetic scalar potential $U(\mathbf{r})$ (and thus invariant magnetic field $\mathbf{B}(\mathbf{r})$) in our setup. This is in agreement with the non-uniqueness of magnetic inverse models; as pointed out by von Helmholtz [66], there exists more than one current distribution that produces the same magnetic field. For instance, an arbitrary number of toroidal current loops may be added without changing the magnetic field pattern outside of the toroid.

2.2 Electromagnetism in MEG

The results in the previous section, Section 2.1, hold for electro-quasi-static approximation, but they only apply for current loops. In this section, we present the conventional neuronal current configuration used in MEG, then assert that they can be equivalently expressed as a closed current loop as well. Thus, the electro-quasi-static expressions (2.12) and (2.15) hold in the context of MEG. These equations are also seen to be able to reproduce and/or are

consistent with Geselowitz's formula and Sarvas' formula, two well-known formulas used in MEG.

First, we note that MEG sensors are located outside of the head, which is assumed to be a source-less region. Moreover, the electro- and magneto-quasi-static approximations are valid since the characteristic length scale of the electric and magnetic field spatial variations are much larger than the size of the head [59, 122]. Thus, in addition to (2.2) and (2.3) being valid under the electro-quasi-static and source-less assumptions, the magneto-quasi-static approximation (i.e. $\partial\mathbf{B}/\partial t = \mathbf{0}$) means that in the context of MEG, Faraday's law reads

$$\boldsymbol{\nabla} \times \mathbf{E}(\mathbf{r}) = \mathbf{0}. \tag{2.26}$$

and the electric field $\mathbf{E}$ may be written as the gradient of an electric scalar potential V,

$$\mathbf{E}(\mathbf{r}) = -\boldsymbol{\nabla} V(\mathbf{r}). \tag{2.27}$$

2.2.1 The primary and volume currents

It is customary to express the total neuronal current density $\mathbf{J}(\mathbf{r}')$ as the sum of a primary current component $\mathbf{J}_{pri}(\mathbf{r}')$ and a volume current component $\mathbf{J}_{vol}(\mathbf{r}')$,

$$\mathbf{J}(\mathbf{r}') = \mathbf{J}_{pri}(\mathbf{r}') + \mathbf{J}_{vol}(\mathbf{r}'). \tag{2.28}$$

The primary current corresponds to physiologically interesting active brain sources, whereas the volume current corresponds to the passive return currents that necessarily complete current loops together with the primary current (due to the conservation of charge). The current density is defined within the head, which is commonly modelled as a multi-layered conducting medium with closed and bounded surfaces [31, 61, 108, 113, 135, 154].

The primary current density $\mathbf{J}_{pri}(\mathbf{r}')$ is often modeled as one or more focal sources, with each represented by either a short and straight line segment, or an electric current dipole. If

we assume N dipolar primary sources, each of them may be written as $\mathbf{D}_i\delta(\mathbf{r}' - \mathbf{r}'_{D,i})$, where $\mathbf{D}_i$ and $\mathbf{r}'_{D,i}$ are the moment and location of the i^{th} current dipole respectively, $i = 1, \ldots, N$. The primary current density in this case will be

$$\mathbf{J}_{pri}(\mathbf{r}') = \sum_{i=1}^{N} \mathbf{D}_i\delta(\mathbf{r}' - \mathbf{r}'_{D,i}) \tag{2.29}$$

where $\delta(\mathbf{x})$ refers to the Dirac delta function.

Biologically, each of these measurable focal sources corresponds to the net temporal summation of post-synaptic dendrite currents in close proximity to each other [59, 77], not action potentials as intuition may assume. The post-synaptic dendrite currents are electrically dipolar in nature and last for tens of milliseconds, whereas axonal action potentials are quadrupolar in nature [34, 64, 124] (due to backpropagation [81, 139]) and last for only a few miliseconds. Hence, the latter has more rapidly decaying magnetic fields as a function of distance, and its short lifespan makes it unlikely that a sufficient number of neurons fire at the same time to cause a temporal summation strong enough to be measured .

The volume currents $\mathbf{J}_{vol}(\mathbf{r}')$ correspond to the ohmic currents in the surrounding conductive medium, driven by the electric fields associated with the changing membrane potentials during neuronal activity [99, 122, 156]. Within a medium of conductivity σ, the volume current is given by

$$\mathbf{J}_{vol}\left(\mathbf{r}'\right) = \sigma\mathbf{E}\left(\mathbf{r}'\right) = -\sigma\nabla V\left(\mathbf{r}'\right), \tag{2.30}$$

where the last equality is obtained from (2.27).

One common forward calculation method is the boundary element method (BEM), which typically uses triangulated, decimated surface meshes for the head model so that the electric potential, which is implicitly defined and difficult to determine in the continuous case, may be more easily calculated through some assumptions, such as uniform conductivity within compartments [98, 118, 136].

2.2.2 Geselowitz's formula

Let us assume that the head is modeled as a bounded conductor G with piecewise conductivities σ_j in N_S regions, $j = 1, \ldots, N_S$, and each of these regions is bounded by surface S_j. From the decomposition of the total current density into primary and volume portions, the magnetic field may be expressed as

$$\mathbf{B}(\mathbf{r}) = \mathbf{b}_{pri}(\mathbf{r}) + \mathbf{b}_{vol}(\mathbf{r}) \tag{2.31}$$

where

$$\mathbf{b}_{pri}(\mathbf{r}) = \frac{\mu_0}{4\pi} \int_G \mathbf{J}_{pri}\left(\mathbf{r}'\right) \times \frac{\mathbf{r} - \mathbf{r}'}{\left|\mathbf{r} - \mathbf{r}'\right|^3}\, dv', \tag{2.32}$$

$$\mathbf{b}_{vol}(\mathbf{r}) = -\frac{\mu_0}{4\pi} \sum_{j=1}^{N_S} \left(\sigma_j' - \sigma_j''\right) \int_{S_j} V\left(\mathbf{r}'\right) \mathbf{n}_j'\left(\mathbf{r}'\right) \times \frac{\mathbf{r} - \mathbf{r}'}{\left|\mathbf{r} - \mathbf{r}'\right|^3}\, dS', \tag{2.33}$$

and $\mathbf{n}_j'(\mathbf{r}')$ is the outward unit normal of surface S_j, σ_j' and σ_j'' are the inner and outer conductivities with respect to S_j, and $V(\mathbf{r}')$ is the electric scalar potential on S_j. Equation (2.31), with its terms defined by (2.32) and (2.33), is known as *Geselowitz's formula* [49].

In Geselowitz's formula, $\mathbf{b}_{pri}$ (2.32) corresponds to the primary current contribution to the magnetic field, whereas $\mathbf{b}_{vol}$ (2.33) corresponds to the volume current contribution. Geselowitz's formula can be derived by substituting the total current expression (2.28) into Biot-Savart law (2.1), then using vector identities and Stoke's theorem to obtain its final form. If we assume N dipole sources as in (2.29), then the primary current contribution of Geselowitz's formula (2.32) collapses due to the Dirac delta function to become

$$\mathbf{b}_{pri}(\mathbf{r}) = \frac{\mu_0}{4\pi} \sum_{i=1}^{N} \mathbf{D}_i \times \frac{\mathbf{r} - \mathbf{r}'_{D,i}}{\left|\mathbf{r} - \mathbf{r}'_{D,i}\right|^3}. \tag{2.34}$$

For simplicity, we will assume $N = 1$ subsequently and drop the dipole-specific subscripts.

Note that Geselowitz's formula also implies that volume currents can be equivalently

expressed as surface current densities on S_j with outward orientations $\mathbf{n}'_j(\mathbf{r}')$; as such, the accuracy of head models are intrinsically tied to the accuracy of volume current contributions. This topic will be explored in detail in Chapter 5.

2.2.3 The magneto- and electro-quasi-static form of Geselowitz's formula

Geselowitz's formula assumes the magneto-quasi-static approximation only. Here, we show a form of it that satisfies the electro-quastatic approximation as well. By assuming that (2.31) can be written in the form of (2.3) and following the steps of (2.5), we see that the magnetic scalar potential for the primary and volume contributions are

$$u_{pri}(\mathbf{r}) = -\frac{1}{4\pi}\int_G \frac{\mathbf{J}_{pri}(\mathbf{r}')\times\mathbf{r}'\cdot\mathbf{r}}{F(\mathbf{r},\mathbf{r}')}\,dv' \tag{2.35}$$

$$u_{vol}(\mathbf{r}) = \frac{1}{4\pi}\sum_{j=1}^{n}\left(\sigma'_j-\sigma''_j\right)\int_{S_j} V(\mathbf{r}')\,\frac{\mathbf{n}'_j(\mathbf{r}')\times\mathbf{r}'\cdot\mathbf{r}}{F(\mathbf{r},\mathbf{r}')}\,dS', \tag{2.36}$$

and the magnetic field contributions are

$$\mathbf{b}_{pri}(\mathbf{r}) = \frac{\mu_0}{4\pi}\int_G\left(\frac{F(\mathbf{r},\mathbf{r}')\mathbf{J}_{pri}\times\mathbf{r}'-\mathbf{J}_{pri}\times\mathbf{r}'\cdot\mathbf{r}\nabla F(\mathbf{r},\mathbf{r}')}{F^2(\mathbf{r},\mathbf{r}')}\right)dv' \tag{2.37}$$

$$\mathbf{b}_{vol}(\mathbf{r}) = -\frac{\mu_0}{4\pi}\sum_{j=1}^{n}\left(\sigma'_j-\sigma''_j\right)\int_{S_j} V(\mathbf{r}')\,\frac{F(\mathbf{r},\mathbf{r}')\mathbf{n}'_j(\mathbf{r}')\times\mathbf{r}'-\mathbf{n}'_j(\mathbf{r}')\times\mathbf{r}'\cdot\mathbf{r}\nabla F(\mathbf{r},\mathbf{r}')}{F^2(\mathbf{r},\mathbf{r}')}\,dS'. \tag{2.38}$$

As a check, we verify that radially-oriented current segments have zero contributions, consistent with (2.12) and (2.15). Indeed, when $\mathbf{J}_{pri}$ is parallel to $\mathbf{r}'$ in the primary current case, or when $\mathbf{n}'_j(\mathbf{r}')$ is parallel to $\mathbf{r}'$ in the volume current case, $\mathbf{b}_{pri}=\mathbf{0}$ and $\mathbf{b}_{vol}=\mathbf{0}$ respectively.

2.2.4 Formulating the volume current as a line current

As previously stated in Section 2.2.1, a focal primary current source may be modeled as a short line current segment of current I. The start and end of the this current segment represent a sink and source respectively, with the associated volume current emanating from the source and ending at the sink [76, 78]. However, the formulations of Section 2.1 hold for

current loops only, hence in order for them to also hold in the context of MEG, it is necessary to show that the volume current may be equivalently written as a line current that forms a closed loop with the primary current.

By Kirchoff's junction rule, the volume current may be equivalently represented as a finite sum of P line current contributions, each flowing from the source to the sink. Let the p^{th} line current have current I_p and be parametrized from $t \in [0,1]$ as $\mathbf{r}'_p(t)$, with $\mathbf{h}'_p(t)$ as the vector that points in the tangential direction of the line current. From the volume current expression equivalent to (2.35) (which is the precursor to (2.36) before Stoke's theorem was performed), the contribution of the volume current towards the magnetic scalar potential may thus be written as

$$u_{vol}(\mathbf{r}) = -\frac{1}{4\pi}\sum_{p=1}^{P} I_p q_p(\mathbf{r}) \tag{2.39}$$

where

$$q_p(\mathbf{r}) = \int_0^1 \frac{\mathbf{r}'_p(t) \times \mathbf{r} \cdot \mathbf{h}'_p(t)}{F(\mathbf{r}, \mathbf{r}'_p(t))} dt, \tag{2.40}$$

and $\sum_{p=1}^{P} I_p = I$ necessarily. We want to show that the sum over all P line integrals in the above equation can be reduced to one equivalent line integral with current I.

Let us consider two of these distinct line currents, say $I_1\mathbf{r}'_1(t)$ and $I_2\mathbf{r}'_2(t)$, and their corresponding line integrals $q_1(\mathbf{r})$ and $q_2(\mathbf{r})$. We may then consider a set of lines parametrized from $w \in [0,1]$ that sweep out an open surface $\mathbf{s}'(t,w)$ with $\mathbf{r}'_1$ and $\mathbf{r}'_2$ forming its boundary; i.e., $\mathbf{s}(t,0) = \mathbf{r}'_1(t)$ and $\mathbf{s}(t,1) = \mathbf{r}'_2(t)$. The intermediate value theorem tells us that there must exist a $w = w_{eq}$ (the subscript "eq" denotes "equivalent"), i.e., a line $\mathbf{s}(t, w_{eq}) = \mathbf{r}'_{eq}(t)$ with tangential direction vector $\mathbf{h}'_{eq}(t)$, such that

$$q_{eq}(\mathbf{r}) \equiv \int_0^1 \frac{\mathbf{r}'_{eq}(t) \times \mathbf{r} \cdot \mathbf{h}'_{eq}(t)}{F(\mathbf{r}, \mathbf{r}'_{eq}(t))} dt = \frac{I_1 q_1(\mathbf{r}) + I_2 q_2(\mathbf{r})}{I_1 + I_2} \tag{2.41}$$

$$\implies (I_1 + I_2) q_{eq}(\mathbf{r}) = I_1 q_1(\mathbf{r}) + I_2 q_2(\mathbf{r}). \tag{2.42}$$

This means that within the conductor, the total magnetic scalar potential contribution from

two line currents can always be equivalently expressed as the contribution from one line current with a current density that is the sum of the original currents'. With this result, the sum in (2.39) can be collapsed in a pair-wise manner to obtain an equivalent line current with current density I that produces an equivalent magnetic scalar potential (and hence equivalent magnetic field).

Therefore, volume currents may always be represented by a line current that form a closed loop with the primary current; we may now write $\mathbf{J}dv' = |\mathbf{J}|d\mathbf{l}' = Id\mathbf{l}'$ for the total current density. The formulations from Section 2.1 thus hold, with $d\mathbf{l}' = d\mathbf{l}'_{pri} + d\mathbf{l}'_{vol}$. Moreover, we readily see how (2.37) and (2.35) (for the total current density $\mathbf{J}$ instead of $\mathbf{J}_{pri}$, before Stoke's theorem was invoked for the volume current portion) are equivalent to (2.15) and (2.12) respectively. This asserts that (2.12) and (2.15) are the generalized forms of the electro- and magneto-quasi-static Geselowitz's formula, since they were derived without head model assumptions.

2.2.5 The current triangle formulation for spherical head models

Now, let us assume a spherical head model. In this special case, the current density can always be written as a triangle loop with one vertex coinciding with the center of the sphere. This result, which has been presented in [76, 78], is a specific case of the conclusion made in the previous section. I.e., an equivalent line current for the volume currents within a spherical conductor is two radial straight line segments that intersect at its center.

If the origin is set to be at the center of the sphere, then $\mathbf{n}'(\mathbf{r}') = \mathbf{r}'/r'$. By a direct inspection of the specialized Geselowitz's formula that was derived (2.38), we see that the volume current contribution to the magnetic field $\mathbf{b}_{vol}(\mathbf{r})$ vanishes with this substitution due to the cross product. I.e., $\mathbf{B}(\mathbf{r}) = \mathbf{b}_{pri}(\mathbf{r})$ everywhere outside the conductor and $\mathbf{b}_{vol}(\mathbf{r}) = \mathbf{0}$. In the past, this observation was made in a less direct manner as follows (see, e.g., [56, 127]): the original Geselowitz's formula (2.33) indicates that the radial component of the volume current contribution $\mathbf{b}_{vol}(\mathbf{r}) \cdot \mathbf{e}_r$ is zero when $\mathbf{n}'(\mathbf{r}') = \mathbf{r}'/r'$ due to the scalar triple product; this tells us $u_{vol} = 0$ from (2.5), which in turn leads to $\mathbf{b}_{vol} = \mathbf{0}$ from (2.3). We also know

from (2.15) that radial current segments give zero magnetic field contributions. This means that the volume current for a spherical head model with origin set at its center can always be modeled as two radial segments that connect from the center of the sphere to either ends of the primary current line segment, forming a current triangle.

If the head model is not spherically symmetric, the current triangle formulation does not hold in general. There will always be regions of the head model where $\mathbf{n}'(\mathbf{r}') \neq \mathbf{r}'/r'$, which results in nonzero volume current contributions. Magnetically silent radial current segments thus cannot account for these nonzero contributions, and the construction of an equivalent current loop, which now requires nontrivial (and likely non-unique [66]) inclusions of non-radial segments, becomes less straightforward. There may be exceptions in the case where symmetries can be exploited, e.g. axially symmetric head models [56].

2.2.6 Sarvas' formula

In addition to assuming a spherical head model and a current triangle source formulation, let us now also assume that the primary current segment is infinitesimally short, i.e., a dipolar primary current source $\mathbf{D}\delta(\mathbf{r}' - \mathbf{r}'_D)$. As we have just discussed, the volume current has a zero contribution if the origin is taken to be at the center of the sphere. The total magnetic field outside the conductor is given by the primary current contribution, which may be found in this case via substituting the dipolar current form into either (2.15) or (2.37),

$$\begin{aligned}\mathbf{B}(\mathbf{r}) &= \mathbf{b}_{pri} \\ &= \frac{\mu_0}{4\pi}\left[\frac{F(\mathbf{r},\mathbf{r}'_D)\mathbf{D}\times\mathbf{r}'_D - \mathbf{D}\times\mathbf{r}'_D\cdot\mathbf{r}\boldsymbol{\nabla}F(\mathbf{r},\mathbf{r}'_D)}{F^2(\mathbf{r},\mathbf{r}'_D)}\right].\end{aligned} \tag{2.43}$$

This is precisely *Sarvas' formula* [127]. Again, we see that (2.15) may be considered as a generalized form of the magnetic field in MEG contexts, since Sarvas' formula can be obtained from it with assumptions (in this case, assuming a spherical head and dipolar source).

Chapter 3

THE TRANSLATIONAL NON-INVARIANCE OF MAGNETIC CONTRIBUTIONS BY OPEN CURRENT SEGMENTS

In this chapter, we delve deeper into the effects of the observation from (2.12) and (2.15) that radial current segments are magnetically silent. Since the concept of being radial is always relative to an origin choice, this means that the magnetic scalar potential and magnetic field contributions of open current segments are translationally non-invariant.

This has implications in forward and inverse models of MEG, especially when there is a disagreement between the true origin of the physical setup and the origin that is reported and used for computations (*co-registration errors*). In the presence of such co-registration errors, source currents are inaccurately localized via inverse models, and any physical interpretations assigned to them may be misleading.

Although the contents of this chapter do not strictly pertain to the issue of signal resolutions nor next-generation sensor instrumentation considerations, it highlights a fundamental source of systematic error that affects many methods implemented in resolution-based analyses. One of these methods is the equivalent current dipole (ECD) inverse model, which will be elaborated further in Section 3.2. In Chapter 5, ECD fits are used to determine how inaccurate high-resolution signals due to head model inaccuracies affect source localization performances, and in in Chapter 6, they are performed on signals reconstructed from sparse sensor array measurements in order to assess their performance and potential future implementation in high-resolution signal measurements.

3.1 Effects of origin translations in the magnetic forward problem

First, we formally establish that the magnetic scalar potential $U(\mathbf{r})$ and magnetic field $\mathbf{B}(\mathbf{r})$ of closed current loos are translationally invariant. Then, we show that the open current

segment contributions are translationally non-invariant and has interpretation effects on ECD inverse model fits.

3.1.1 Translational invariance of $U(\mathbf{r})$ and $\mathbf{B}(\mathbf{r})$ for closed current loops

Recall (2.6), which is the magnetic scalar potential $U(\mathbf{r})$ due to a closed current loop. If we translate the origin by $\mathbf{r}_t$, i.e.

$$\mathbf{r} \to \tilde{\mathbf{r}} = \mathbf{r} - \mathbf{r}_t \tag{3.1}$$

$$\mathbf{r}' \to \tilde{\mathbf{r}}' = \mathbf{r}' - \mathbf{r}_t, \tag{3.2}$$

where tildes denote translated coordinates, then we have

$$\tilde{U}(\tilde{\mathbf{r}}) = \frac{I}{4\pi} \int_0^\infty \int_{\mathcal{C}} \frac{(\mathbf{r} - \mathbf{r}') \times \mathbf{e}_{\tilde{r}} \cdot d\mathbf{l}'}{|\mathbf{r} + t\mathbf{e}_{\tilde{r}} - \mathbf{r}'|^3} \, dt \tag{3.3}$$

$$= \frac{1}{\mu_0} \int_0^\infty \mathbf{B}(\mathbf{r} + t\mathbf{e}_{\tilde{r}}) \cdot \mathbf{e}_{\tilde{r}} \, dt \tag{3.4}$$

$$= U(\mathbf{r}) \tag{3.5}$$

where the last equation holds by the fundamental theorem of calculus, since $\mathbf{B}$ due to a closed current loop is conservative. Since the scalar potentials are equivalent, (2.3) indicates that the magnetic fields corresponding to the original and translated coordinate systems are necessarily equal as well, i.e. $\tilde{\mathbf{B}}(\tilde{\mathbf{r}}) = \mathbf{B}(\mathbf{r})$. Note that (3.4) also tells us that any arbitrary integration path taken to infinity in any direction will yield invariant results; this is consistent with the path independence of (2.5).

Therefore, under the electro-quasi-static assumption in a source-free region, there is translational symmetry for the magnetic potentials and magnetic fields produced by closed current loops.

3.1.2 Translational non-invariance of $u(\mathbf{r})$ and $\mathbf{b}(\mathbf{r})$ for open current segments

The result of having translationally invariant magnetic contributions above do not extend to open current segments. For clarity, we will denote the magnetic scalar potential and magnetic field for open segments with lowercase letters, i.e. $u(\mathbf{r})$ and $\mathbf{b}(\mathbf{r})$ respectively.

Let us consider an open segment $\mathcal{D}$ here in place of the closed loop $\mathcal{C}$. The integral bounds of (3.3) now become $\mathcal{D}$. Since (2.2) holds only for closed loops, the magnetic field in this case is not necessarily conservative. Therefore, (3.5) is not generally true for $u(\mathbf{r})$, and the magnetic scalar potential is hence not always invariant under translations. In other words, $\tilde{u}(\tilde{\mathbf{r}})$ is not necessarily equal to $u(\mathbf{r})$ for open current segments. We may explicitly write this result out as follows.

Let us define

$$\bar{F}(\mathbf{r}, \mathbf{r}', \mathbf{r}_t) \equiv a(\tilde{r}a - ra - \mathbf{a} \cdot \mathbf{r}_t). \tag{3.6}$$

Under a coordinate translation by $\mathbf{r}_t$,

$$\tilde{F}(\tilde{\mathbf{r}}, \tilde{\mathbf{r}}') = F(\mathbf{r}, \mathbf{r}') + \bar{F}(\mathbf{r}, \mathbf{r}', \mathbf{r}_t), \tag{3.7}$$

$$d\tilde{\mathbf{L}}' = -I(\tilde{\mathbf{r}}' \times d\mathbf{l}') = d\mathbf{L}' + I\mathbf{r}_t \times d\mathbf{l}', \tag{3.8}$$

and thus the translated version of (2.12) becomes

$$\tilde{u}(\tilde{\mathbf{r}}) = -\frac{1}{4\pi} \int_{\mathcal{D}} \frac{d\tilde{\mathbf{L}}' \cdot \tilde{\mathbf{r}}}{\tilde{F}(\tilde{\mathbf{r}}, \tilde{\mathbf{r}}')} \tag{3.9}$$

$$= -\frac{1}{4\pi} \int_{\mathcal{D}} \left[(d\mathbf{L}' \cdot \mathbf{r} - (d\mathbf{L}' + I\mathbf{r} \times d\mathbf{l}') \cdot \mathbf{r}_t) \cdot \left(\frac{1}{F(\mathbf{r}, \mathbf{r}')} + \frac{\bar{F}(\mathbf{r}, \mathbf{r}', \mathbf{r}_t)}{F(\mathbf{r}, \mathbf{r}')\tilde{F}(\tilde{\mathbf{r}}, \tilde{\mathbf{r}}')} \right) \right] \tag{3.10}$$

$$= u(\mathbf{r}) + \bar{u}(\mathbf{r}, \mathbf{r}_t), \tag{3.11}$$

where

$$\bar{u}(\mathbf{r},\mathbf{r}_t)=\frac{1}{4\pi}\int_{\mathcal{D}}\left[\frac{\bar{F}(\mathbf{r},\mathbf{r}',\mathbf{r}_t)d\mathbf{L}'\cdot\mathbf{r}}{F(\mathbf{r},\mathbf{r}')\tilde{F}(\tilde{\mathbf{r}},\tilde{\mathbf{r}}')}+\frac{(d\mathbf{L}'+I\mathbf{r}\times d\mathbf{l}')\cdot\mathbf{r}_t}{\tilde{F}(\tilde{\mathbf{r}},\tilde{\mathbf{r}}')}\right] \tag{3.12}$$

is not necessarily zero. This tells us that open current segment contributions toward the magnetic scalar potential are not necessarily invariant under coordinate translations. As a simple check, we see that when there is no coordinate translation, i.e. when $\mathbf{r}_t=\mathbf{0}$, then $\bar{F}=0$, and hence $\bar{u}=0$ as expected.

Now, we show the translational non-invariant in the case of $\tilde{\mathbf{b}}(\tilde{\mathbf{r}})$ as well. A simple rearrangement of (3.11) gives us $u=\tilde{u}-\bar{u}$. Clearly then, $\boldsymbol{\nabla}\bar{u}(\mathbf{r},\mathbf{r}_t)\neq\mathbf{0}$, since

$$\mathbf{b}(\mathbf{r})=-\mu_0\boldsymbol{\nabla}u(\mathbf{r})\neq-\mu_0\boldsymbol{\nabla}\tilde{u}(\tilde{\mathbf{r}}). \tag{3.13}$$

This indicates that a translation by $-\mathbf{r}_t$ results in a difference of the magnetic field produced by an open line segment by $-\boldsymbol{\nabla}\bar{u}(\tilde{\mathbf{r}},\mathbf{r}_t)$.

Note that from (3.8), it is clear that in the translated coordinate system where $\mathbf{r}'\to\tilde{\mathbf{r}}'$, radial current segments with respect to the translated origin ($d\mathbf{l}'$ parallel to $\tilde{\mathbf{r}}'$) are magnetically silent as well. Figure 3.1 summarizes the main results of the previous two sections, Sections 3.1.1 and 3.1.2.

3.1.3 Verification of the translational non-invariance of $\tilde{u}(\tilde{\mathbf{r}})$

We now verify the results in the previous section numerically. This is done by considering the contributions from a simple triangle current loop and its individual edges in various origin choices as follows.

The triangle loop was defined by specifying three random vertices of up to length 5 cm from $(0,0,0)$ cm. The contribution from each edge was defined as $\tilde{u}_i(\tilde{\mathbf{r}})$, $i=1,2,3$. Then, 12 origins were used to evaluate the contributions of each edge: 9 origins were spaced evenly on the triangle loop (labeled with origin indices 1 to 9), and 3 random origins of up to 5 cm from $(0,0,0)$ cm that do not lie on the triangle were specified (indices 10 to 12). The field point

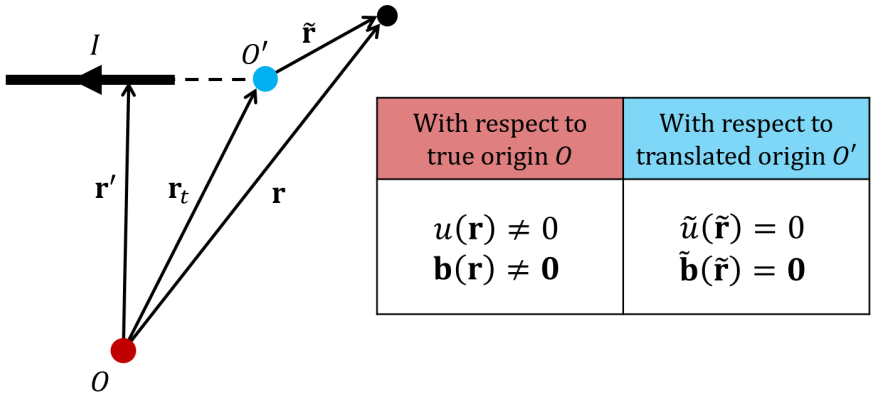

Figure 3.1: Illustration on how an open current segment has a non-invariant magnetic scalar potential and magnetic field when different origins are chosen. In the coordinate system with origin O, the current segment is non-radial and hence not magnetically silent. However, with respect to the translated origin O', the current segment becomes radial and is magnetically silent because $d\mathbf{L}' = 0$ when $\mathbf{r}'$ is parallel to $d\mathbf{l}'$.

was randomly picked to be 12 cm away from $(0, 0, 0)$ cm, and the magnetic scalar potential for each triangle edge was evaluated with (3.9).

The physical setup of the triangle and origin points are shown in the left subplot of Figure 3.2, and the contributions from each edge when evaluated with respect to each of the 12 origins using are shown in the right subplot of Figure 3.2. We see that indeed, $\tilde{u}_i(\tilde{\mathbf{r}})$ is not invariant for each edge under coordinate translations. However, the closed loop contribution when all three components are added together is invariant under coordinate translations (magenta line), as expected from Section 3.1.1. When for origins located at the vertices or along an edge, only the non-radial edges relative to that origin had non-zero scalar potential contributions as expected.

3.1.4 Translational invariance of the electric forward problem: an aside

As an aside, we explore the electric counterpart of our magnetic considerations. We show here that the contributions towards the electric scalar potential and electric field by charges under the magneto-quasi-static assumption are always translationally invariant. This applies to EEG setups, which measure (the difference of) electric scalar potentials.

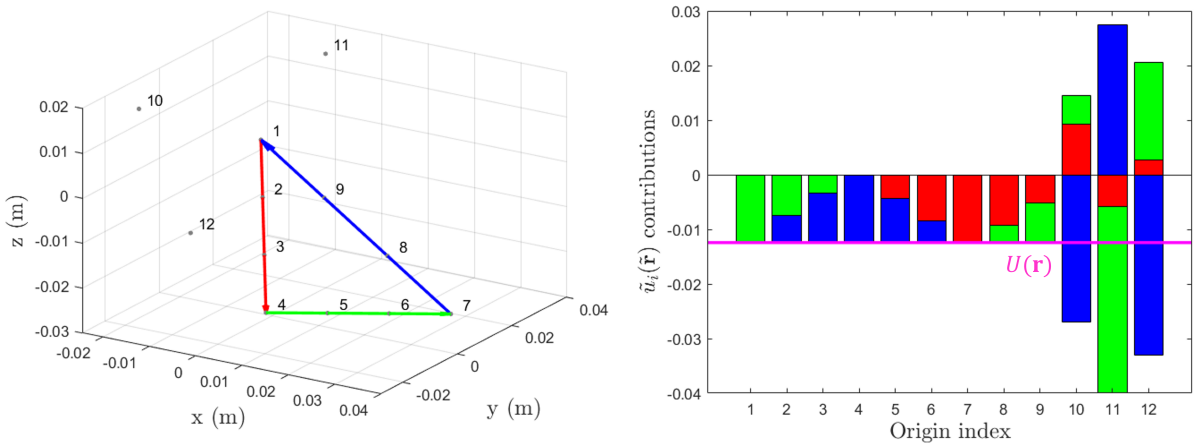

Figure 3.2: (Left) Current triangle setup and the 12 computational origins considered. (Right) Show the varying $\tilde{u}_i(\tilde{\mathbf{r}})$ contribution by each line segment of the current triangle at various origins. Each edge and their corresponding $\tilde{u}_i(\tilde{\mathbf{r}})$ contributions have matching colors. Only non-radial current segments have non-zero contributions. The magenta line shows the translationally invariant $U(\mathbf{r})$ of the closed loop.

Coulomb's law states that the electric field of a line charge with charge density $\lambda(\mathbf{r}')$ along a line segment $\mathcal{D}$ is given by

$$\mathbf{E}(\mathbf{r}) = \frac{1}{4\pi\epsilon_0}\int_{\mathcal{D}} \frac{\lambda(\mathbf{r}')(\mathbf{r}-\mathbf{r}')}{|\mathbf{r}-\mathbf{r}'|^3}\, dl', \tag{3.14}$$

where ϵ_0 is the vacuum permittivity. Let us assume a straight line charge of length l, with constant charge density $\lambda(\mathbf{r}') = \lambda$. This charge segment can be parametrized as $\mathbf{r}' = \mathbf{r}'_0 + \mathbf{h}'t'$, $t' \in [0, l]$, where $\mathbf{r}'_0$ is the position of one end of the line segment and $\mathbf{h}'$ is the vector pointing towards the other end. Its electric field contribution can thus also be written as

$$\mathbf{E}(\mathbf{r}) = \frac{\lambda}{4\pi\epsilon_0}\int_0^l \frac{\mathbf{r}-\mathbf{r}'_0-\mathbf{h}'t'}{|\mathbf{r}-\mathbf{r}'_0-\mathbf{h}'t'|^3}\, dt'. \tag{3.15}$$

Under magneto-quasi-static approximation, (2.26) and (2.27) allow us to find the electric

scalar potential via the gradient theorem approach as presented in Section 2.1,

$$V(\mathbf{r}) = -\int_0^\infty \boldsymbol{\nabla} V(\mathbf{r} + t\mathbf{e}_r) \cdot \mathbf{e}_r \, dt \tag{3.16}$$

$$= \int_0^\infty \mathbf{E}(\mathbf{r} + t\mathbf{e}_r) \cdot \mathbf{e}_r \, dt. \tag{3.17}$$

If we let $\mathbf{a}_E = \mathbf{r} - \mathbf{r}'_0 - \mathbf{h}'t'$, $k_E = \mathbf{a}_E \cdot \mathbf{e}_r$ and $y_E = t + k_E$, then we have

$$V(\mathbf{r}) = \frac{\lambda}{4\pi\epsilon_0} \left(\int_0^l k \int_0^\infty \frac{1}{|\mathbf{a}_E + \mathbf{e}_r|^3} \, dt dt' + \int_0^l \int_0^\infty \frac{t}{|\mathbf{a}_E + t\mathbf{e}_r|^3} \, dt dt' \right). \tag{3.18}$$

The inner integral in the first term is given by (2.8), whereas the inner integral of the second term is easily evaluated in a similar manner to be

$$\int_0^\infty \frac{t}{|\mathbf{a}_E + t\mathbf{e}_r|^3} \, dt = \frac{1}{a_E + k}. \tag{3.19}$$

Thus, we have

$$V(\mathbf{r}) = \frac{\lambda}{4\pi\epsilon_0} \int_0^l \frac{1}{a_E} \, dt'. \tag{3.20}$$

Since a_E is independent of origin choice, this expression indicates that the electric scalar potential of an open straight line charge (and hence the electric field as well) is translationally invariant. Note that the condition of a source-less region is not required in this electric forward model.

This result is expected to be consistent with the current loop magnetic field counterpart; point charges are analogous to current loops (magnetic dipoles) since they are the the fundamental electric and magnetic sources respectively. This result also tells us that the subsequent discussions about complications arising from translational non-invariance of open line sources do not apply for electric measurements such as EEG measurements.

For completeness, we evaluate the integral of (3.20) and state its final form. Let $\mathbf{b} = \mathbf{r} - \mathbf{r}'_0$,

$c = \mathbf{b} \cdot \mathbf{h}'$, and $z = t' - c$ so $dz = dt'$. Then, the magnetic scalar potential is found to be

$$V(\mathbf{r}) = \frac{\lambda}{8\pi\epsilon_0} \ln \left(\frac{\sqrt{l^2 - 2lc + b^2} + (l - c)}{\sqrt{l^2 - 2lc + b^2} - (l - c)} \cdot \frac{b + c}{b - c} \right). \tag{3.21}$$

This expression is presented in many electromagnetism textbooks, though likely in slightly different forms. For instance, see Problem 2.25 in [55].

3.2 Effect on ECD inverse models

We have shown that closed current loops have invariant contributions to the magnetic field under coordinate translations, but not its individual segments/open current segments. This has effects on MEG ECD inverse models as will be shown in this section. For simplicity, we have considered a spherical head model.

In general, ECD fits attempt to fit the signal produced by one or more electric dipole sources (calculated using Sarvas' formula (2.43)) to a reference measured signal. This is done by finding an ideal location and orientation for the dipoles so that the error between the signal produced by the dipoles and the reference signal is minimized.

Two methods in which the ideal dipole locations/orientations may be found are by directly varying their locations/orientations in an iterative manner to minimize the signal error, or by setting up a grid of plausible dipole locations, then exhaustively finding a grid point that results in the lowest signal error for some ideal orientation there. The former iterative method has the advantage of being more computationally efficient; however it runs the risk of converging to a local minimum that is not at the desired solution [25] (see Figure 4.2, which show multiple local minima if using the relative error metric (4.27)). The latter exhaustive method circumvents this issue, but may not accurately find the global solution if the grid is coarse. Having a fine grid also tends to be computationally slow. In our case, we employ the latter exhaustive search, since our main goal is to find the global solution. The fit procedure that we implemented will be further detailed in Section 3.2.3. For a detailed introduction to ECD fits for neural activity, one may refer to [128].

3.2.1 Validity of ECD fits

Before presenting the results of the MEG ECD fits, the validity of ECD fits should first be discussed. In literature, it is often assumed that dipoles can accurately reproduce the signals produced by models of focal neural sources. This assumption is, of course, true by definition if the focal sources are modeled as electric dipoles. However, for sources modeled by finite lengths of currents, the validity of this assumption becomes less trivial.

We justify that for a straight line current segment, there exists an equivalent dipole that exactly reproduces its magnetic field.

Let us define a straight line current segment with length l, current strength I, and parametrization $\mathbf{r}'(t) = \mathbf{r}'_0 + \mathbf{h}'t$, $t \in [0, l]$, where $\mathbf{r}'_0$ is the position of the starting end of the segment and $\mathbf{h}'$ is the unit vector pointing in the direction of current flow. By (2.1), the magnetic field produced by this current source may be written in a form mathematically similar to (2.7),

$$\mathbf{b}(\mathbf{r}) = \frac{\mu_0 I}{4\pi} \left[\mathbf{h}' \times (\mathbf{r} - \mathbf{r}'_0)\right] \int_0^l \frac{dt}{|\mathbf{r} - \mathbf{r}'_0 - \mathbf{h}'t|^3}. \tag{3.22}$$

The mean value theorem for integrals with scalar field integrands tells us that there must exist a $t = t_D \in [0, l]$ such that the above magnetic field produced by an open line segment (3.22) is equivalently

$$\mathbf{b}(\mathbf{r}) = \frac{\mu_0 I l}{4\pi} \frac{\mathbf{h}' \times (\mathbf{r} - \mathbf{r}'_0)}{|\mathbf{r} - \mathbf{r}'_0 - \mathbf{h}'t_D|^3}. \tag{3.23}$$

This is precisely the form of the magnetic field produced by a dipole, given by (2.34) with $N = 1$, $\mathbf{D} = Il\mathbf{h}'$, and $\mathbf{r}_D = \mathbf{r}'_0 + \mathbf{h}'t_D$. There is thus a guaranteed ECD fit with strength Il that produces an identical signal as a line segment. The equivalent dipole lies on the line segment itself, and has orientation that points along the current flow.

In theory, by the principle of superposition, multi-dipole inverse models are valid for source configurations made up of straight line segments; an N-edged current loop will have an

exact N dipole fit. However, since the mean value theorem only guarantees a solution along the line and not an exact position, the dipole solutions are are likely informative only for short line segments where the position variation is restricted to be small. Moreover, constraints are expected to be required to accurately find these solutions, again due to the ill-posed nature of inverse problems [66].

As discussed in Section 2.2.5, for a spherical head model with the current triangle formulation and origin taken to be at the center of the sphere, the only contributing current segment is the non-radial primary current. A single dipole ECD fit is thus sufficient to locate this primary current segment, and the resulting dipole is justifiably interpreted as the primary current source. In MEG, this is one of the most commonly used and validated source localization methods, even in clinical settings [6, 62, 95]. However, in Section 3.2.3, we show that the physical interpretation of a single dipole ECD fit as the primary current should be made with caution, especially if the exact location of the computational origin is not known accurately. Despite the ECD fit being valid with an exact solution at certain shifted origin points, the localized dipoles may correspond to volume current contributions or possibly have no meaning at all.

Note that the ability of an iterative ECD fit algorithm to find an exact solution on the straight line segment may depend on factors such as a sufficiently accurate initial guess, the objective function choice, and the stability of the solution.

3.2.2 Verification of the validity of ECD fits

Here, we perform a simple computational verification of our claim above in Section 3.2.1 that for a triangular current loop with origin at any of its vertices, there always exists a dipole on the opposite edge that exactly reproduces the magnetic field of that edge.

An arbitrary current triangle with current strength $I = 1$ A was first specified, with each vertex being up to 5 cm away from the $(0, 0, 0)$ cm origin. Each edge was discretized into 50 points, and each point was taken to be an origin. For each origin, the signal due to a dipole located at every other point was calculated. As suggested by (3.23) about the exact solution,

each of these dipoles was set to have strength I multiplied by that edge's length, as well as orientation parallel to the edge it was located on. Let us denote the signal produced by such a dipole (relative to some origin) to be $\boldsymbol{\phi}_D$.

The forward magnetic field of the entire triangle loop (that was then used to calculate the reference flux signal) was obtained by performing the closed loop Biot-Savart line integral. This calculation was done with respect to the $(0, 0, 0)$ cm origin for convenience and used for all origin cases; we know from Section 3.1.1 it will be translationally invariant. Let us denote this reference signal as $\boldsymbol{\phi}_{ref}$.

The MEG sensor array that was considered was the standard placement of the 102 magnetometers of the Elekta Neuromag TRIUX system (Megin, Helsinki, Finland). Each magnetometer is square with side length 2.1 cm, and the signal for each sensor was calculated via a 9-point cubature sampling approximation of the magnetic field over the sensor area (see Chapter 4 for more details). The sensor array is shown in the left subplot of Figure 3.4.

Let the error between $\boldsymbol{\phi}_{ref}$ and $\boldsymbol{\phi}_D$ be quantified by

$$\epsilon = \frac{\|\boldsymbol{\phi}_{ref} - \boldsymbol{\phi}_D\|^2}{\|\boldsymbol{\phi}_{ref}\|^2} \tag{3.24}$$

which ranges from $\epsilon = 0$ when $\boldsymbol{\phi}_{ref} = \boldsymbol{\phi}_D$ to $\epsilon = 1$ when $\boldsymbol{\phi}_D = \mathbf{0}$ or $\boldsymbol{\phi}_D = -2\boldsymbol{\phi}_{ref}$. This means that we may define a goodness of fit (GOF),

$$\text{GOF} = 1 - \epsilon, \tag{3.25}$$

with GOF $= 0$ indicating the worst possible agreement between $\boldsymbol{\phi}_{ref}$ and $\boldsymbol{\phi}_D$, and GOF $= 1$ indicating perfect agreement.

Figure 3.3 shows the highest GOF value attainable at every origin for some dipole along the triangle. We see that indeed, when the origins are at the triangle vertices, GOF ≈ 1. Each of the three vertex origins is marked by a colored "x", and the dipole that yielded the highest GOF value is marked with a solid circle with the corresponding color. The dipoles

reside on the opposite edge of each vertex as expected from 3.2.1.

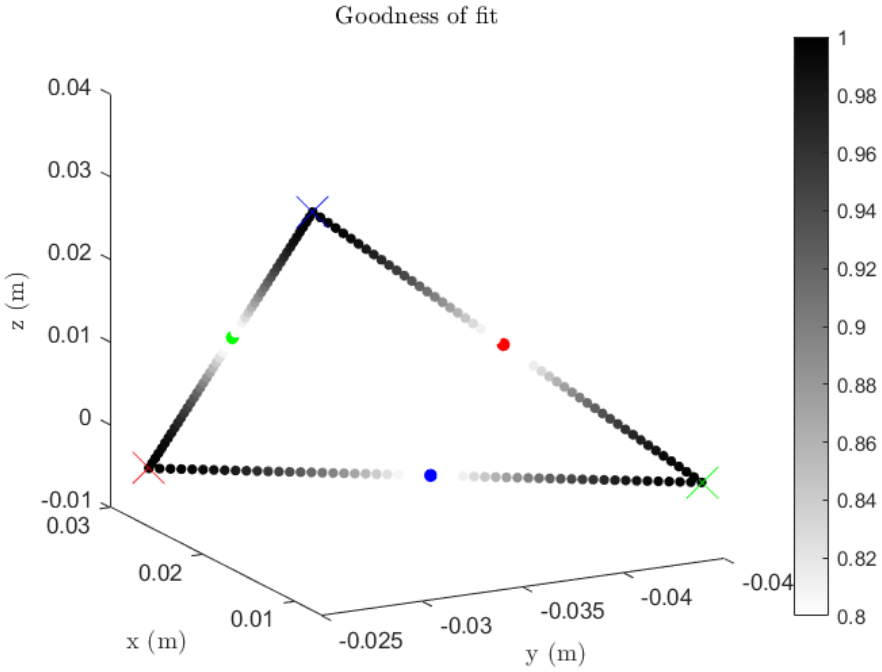

Figure 3.3: Shows the maximum ECD GOF attainable at each origin point that lies along an arbitrary current triangle when the dipole solutions are constrained to be parallel along the triangle edges. When the origin coincides with a triangle vertex, the dipole with maximum GOF lies approximately at the middle of the opposite edge. Each vertex origin is marked by an "x", and the ECD location is marked by a solid circle with matching color.

For origins on the triangle that do not coincide with the vertices, the highest attainable GOF for dipole sources also located on the triangle and parallel along its edges is less than 1, reaching a minimum for origins near the center of each edge. In Section 3.2.5 later on however, we observe via an unconstrained ECD fit that there exist dipoles not necessarily lying on the triangle that yield a high GOF whenever the origin lies in the plane of the triangle.

3.2.3 Unconstrained ECD fit procedure

The validity of the ECD inverse method is now verified for source models involving straight line current segments, including triangle current loops. We now proceed to show how the property of open current segments having translationally non-invariant magnetic contributions

affects the results of a simple unconstrained MEG ECD fit.

We again considered a spherical head model with a current triangle source. The three triangle vertices were defined to be at $(0, 0, 0)$ cm and $(\pm 0.25, 0, 3.3)$ cm, corresponding to the deep-source of the Elekta Neuromag dry phantom (Megin Oy, Helsinki, Finland), and the current strength was arbitrarily set to be 1 A. Conventionally, the short horizontal edge at $z = 3.3$ cm is interpreted to be the primary current segment. The sensor array and method of calculating the forward signal was identical to the previous section (Section 3.2.2). The left subplot of Figure 3.4 shows the current triangle and sensor array setup.

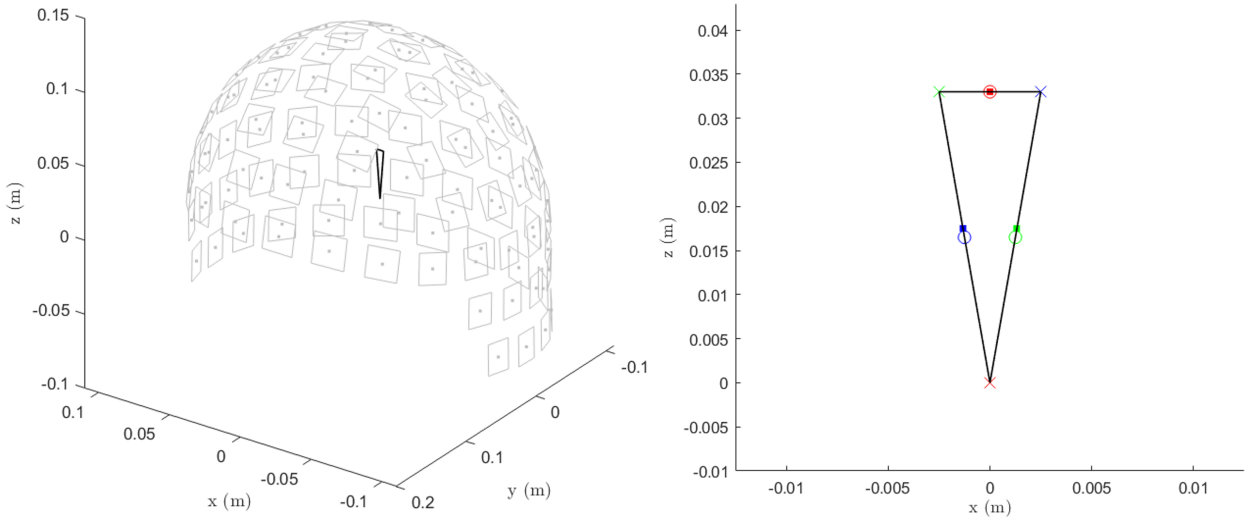

Figure 3.4: (Left) Magnetometer sensor array setup and current triangle configuration used for the unconstrained exhaustive ECD search. (Right) Unconstrained ECD fit results when the origin choice coincides with one of the triangle vertices. Each of the three origins is marked by an "x", and the corresponding ECD fit result is marked by a solid square with matching color. The center of each triangle edge is marked by a hollow circle. The unconstrained fits shown here are in agreement with the constrained fits shown in Figure 3.3.

Two planes of 20×20 grids of translated origins was defined: one in the $y = 0$ (xz) plane from $x \in [-3, 3]$ cm and $z \in [-1, 5]$ cm, and the other in the $z = 0$ (xy) plane from x, $y \in [-3, 3]$ cm. These planes are parallel and perpendicular to the plane defined by the current triangle respectively. Let us denote the $(0, 0, 0)$ cm origin (center of the sphere) to be

the "reference origin".

As mentioned in Section 3.2, we opted for an exhaustive search for the optimal dipole location instead of an iterative search. Every grid point in both the xz and xy planes was set to be a translated origin, and for each of these origins, an optimal xz grid point (not equal to itself) was identified as the ECD location, where some dipole orientation minimizes the error between $\boldsymbol{\phi}_{ref}$ and $\boldsymbol{\phi}_D$ to give the highest attainable GOF. This procedure is described as below.

Let us consider one particular origin, and an xz grid point not equal to this origin. First, the corresponding topography matrix $\boldsymbol{\gamma}_D$ at that xz grid point (or *lead field*) was calculated. The lead field of a given point is a matrix of size $N_S \times 3$, with each column corresponding to the signal measured by a N_S-sensor array due to a unit dipole located at that point oriented in each of the 3 orthogonal coordinate directions. In our case then, the lead field $\boldsymbol{\gamma}_D$ is a 102×3 matrix. If we define $\boldsymbol{\alpha}_D$ to be a 3×1 vector corresponding to the dipole strength in each of the 3 orthogonal coordinate directions, we may write

$$\boldsymbol{\phi}_D = \boldsymbol{\gamma}_D \boldsymbol{\alpha}_D. \tag{3.26}$$

Note that $\boldsymbol{\alpha}_D$ is unit-less by construction; however, it has exactly the same values as the dipole moment. We will simply refer to $\boldsymbol{\alpha}_D$ as the dipole moment from hereon. The dipole moment $\boldsymbol{\alpha}_D = \boldsymbol{\alpha}_{D,est}$ that minimizes the objective function ϵ (3.24) was then obtained,

$$\boldsymbol{\alpha}_{D,est} = \underset{\boldsymbol{\alpha}_D}{\operatorname{argmin}} \left(\frac{\|\boldsymbol{\phi}_{ref} - \boldsymbol{\gamma}_D \boldsymbol{\alpha}_D\|^2}{\|\boldsymbol{\phi}_{ref}\|^2} \right). \tag{3.27}$$

This was done using Matlab's fminsearch with an arbitrary initial guess of $\boldsymbol{\alpha}_D = (1, 1, 1)$; the results obtained were found to be insensitive to this initial guess. Then, the GOF was found with (3.25),

$$\text{GOF} = 1 - \epsilon(\boldsymbol{\alpha}_{D,est}). \tag{3.28}$$

This process is repeated for all other xz grid points for this particular origin. The xz grid point and optimized dipole moment corresponding to the highest GOF was determined to be the ECD solution for this origin. Let us denote this highest GOF value as GOF_{ECD}, and the corresponding optimal dipole position and moment as $\mathbf{r}'_{ECD}$ and $\boldsymbol{\alpha}_{ECD}$ respectively.

Note that the immediate solution $\mathbf{r}'_{ECD}$ that an ECD fit provides is relative to the translated origin. In order to compare this with the expected true solution $\mathbf{r}'_{D,true}$, which is relative to the reference origin, one needs to translate $\mathbf{r}'_{ECD}$ back into the reference coordinate system (or choose a common coordinate system to work in). For notational simplicity, we have denoted all $\mathbf{r}'_{ECD}$ used here refer to the ECD fit solution that has already been appropriately translated back into the reference coordinate system.

Finally, the localization error (LE) of the ECD solution was found via taking the Euclidean distance between $\mathbf{r}'_{ECD}$ and the expected ECD solution $\mathbf{r}'_{D,true}$,

$$\text{LE}_{ECD} = \left\|\mathbf{r}'_{ECD} - \mathbf{r}'_{D,true}\right\|. \tag{3.29}$$

The expected solution was set to be at the center of the short horizontal edge, $\mathbf{r}'_{D,true} = (0, 0, 3.3)$ cm; this is inferred from our results as shown in Figure 3.3, which indicates that the exact ECD fit should lie approximately in the center of the edge.

The above procedure is repeated for all other origins. The final result is thus a GOF_{ECD}, LE_{ECD}, $\mathbf{r}'_{ECD}$, and $\boldsymbol{\alpha}'_{ECD}$, assigned to each origin.

3.2.4 Results

The LE_{ECD} and GOF_{ECD} results for each origin of the xz and xy grids are shown in Figure 3.5.

The first column of Figure 3.5 shows the LE_{ECD} and GOF_{ECD} values for origins in the xz plane. Despite the LE having a minimum only at the reference origin, the GOF has a maxima not only at this reference origin, but also the region around the other two triangle vertices. This may be explained as follows. When the origin coincides with any of the three triangle vertices, only the opposite edge is non-radial and hence contributes entirely to the total magnetic field of the loop. From Section 3.2.1, this means that there is an exact ECD

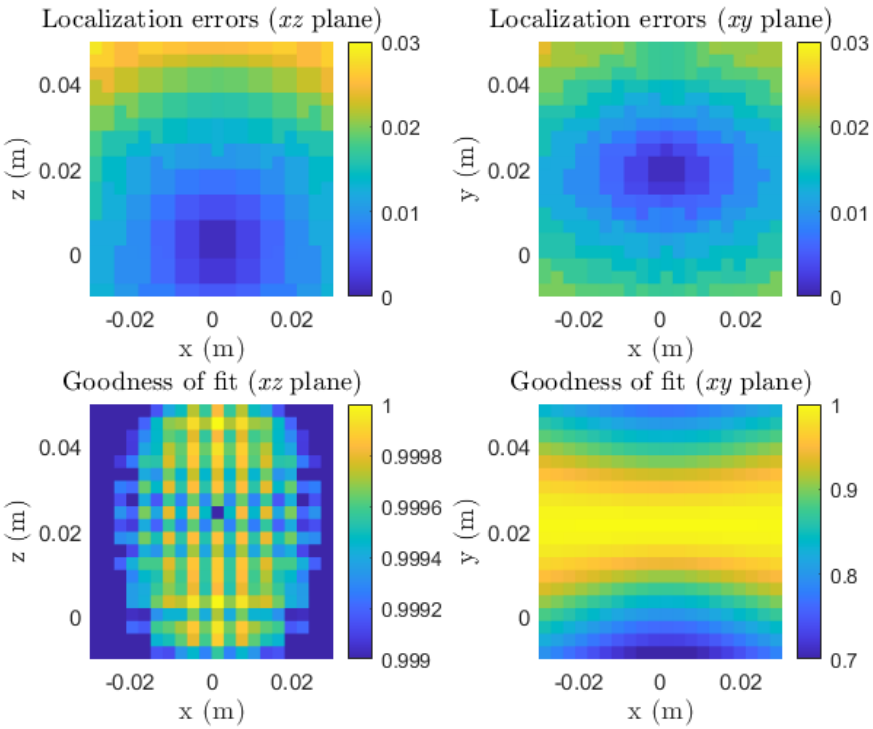

Figure 3.5: LE_{ECD} and GOF_{ECD} plots for the ECD fits at various origin choices. The current triangle had vertices at $(0, 0, 0)$ cm and $(\pm 0.25, 0, 3.3)$ cm on the xz plane. LE increases when the origin choice is further from the $(0, 0, 0)$ cm origin, but GOF is high for all origins in the xz plane, especially in areas near the triangle vertices. GOF falls off much quicker for origin translations in directions perpendicular to the triangle plane. LE is comparable for origin translations of the same amount in both the xz plane and the xy plane.

solution that lies on the opposite edge, resulting in a high GOF. However, this means a high LE as well for the two origins not at $(0, 0, 0)$ cm.

The locations of the ECD fits when the origin coincides with the three triangle vertices are shown in the right subplot of Figure 3.4. Each origin is denoted by a colored "x", and the corresponding ECD fit is denoted by a solid square marker with the matching color. The hollow circles denote the center of each edge. We see that indeed, an unconstrained ECD fit localizes the dipole to the opposite edge as expected, which is consistent with the theory in Section 3.2.1 and its verification in Section 3.2.2.

The second column of Figure 3.5 shows the LE and GOF for origins in the xy plane. We see that the LE amounts are similar to the results of xz plane. However, the GOF decays much more rapidly for origins that are translated away from the xz plane. This may be explained by how a single dipole/current line segment cannot replicate the signal produced by more than one current segment when the origin does not coincide with one of the three triangle vertices and does not lie on the triangle's plane.

The results of Figure 3.5 indicate that GOF is generally not an accurate indicator of LE in any way. If one performs an ECD fit and obtains a high GOF, any conclusions about the dipole's LE (and hence physical interpretation) should still be made with caution.

We also note again that other objective function choices may be used to obtain an ECD fit. We found that by iteratively minimizing the subspace angle between $\boldsymbol{\phi}_{ref}$ and $\boldsymbol{\phi}_D$ via varying the dipole position $\mathbf{r}_D$, Figure 3.5 was replicated. In this instance of using an iterative method, the convergence to any potentially existing local minima was avoided.

3.2.5 Origins in the plane of the current triangle

An interesting observation is that in the bottom left subplot of Figure 3.5, the GOF values for all origins are high and approximately 1 for all origins in the xz plane. Upon further inspection of $\boldsymbol{\alpha}'_{ECD}$, the ECD fits were all found to be oriented in the xz plane. We also know from the cross product in (2.43) that only the tangential projection of the dipole has nonzero contribution to the signal. This implies that there exists an infinite number of (near)-perfect

ECD fits in the plane of the triangle if the origin choice also lies in the same plane; each of these solutions has the same tangential dipole moment component and location as the original ECD fit, but varying radial components.

To inspect the purely tangential dipole, we projected $\boldsymbol{\alpha}'_{ECD}$ onto the line perpendicular to the line connecting the origin and $\mathbf{r}'_{ECD}$ in the xz plane (of the triangle). Let us denote the projected $\boldsymbol{\alpha}'_{ECD}$ for the i^{th} xz grid origin to be $\boldsymbol{\alpha}'_{ECD_\perp,i}$, the origin position to be $\mathbf{r}_{origin,i}$, and the ECD fit position to be $\mathbf{r}'_{ECD,i}$ (these are all defined relative to the reference origin). We notice that $||\boldsymbol{\alpha}'_{ECD_\perp,i}||$ is approximately inversely proportional to $||\mathbf{r}'_{ECD,i} - \mathbf{r}_{origin,i}||$, as shown in Figure 3.6. The GOF for the projected dipole is necessarily (and verified to be) equivalent to the unprojected $\boldsymbol{\alpha}'_{ECD}$ case.

From the results in Section 3.2.1, the observations above are equivalent to saying that when the origin lies in the plane of the current triangle there exists infinite number of current triangles also in the same plane, each having two radial edges, that produces approximately the same signal as the reference signal. At least one of these triangles (the triangle constructed from the tangential projection of the ECD fit) has the same surface area as the original triangle.

The infinite triangles observation is consistent with the non-uniqueness of inverse models. The constant surface area observation for the triangle constructed from the tangential projection of the ECD fit is plausible in the sense that in the far-field approximation, having the same surface area guarantees that the magnetic field contribution of the equivalent triangle agrees with that of the original triangle. Both are equal to the field corresponding to a magnetic dipole with moment $\mathbf{m} = I\mathbf{K}$ as shown in Section 2.1.1.

3.3 Further discussions into the implications in MEG methods

3.3.1 Assigning physical meaning to current segments

It is commonly stated in the field of MEG that for a spherical head model, the radial component of the magnetic field has no contribution from volume currents and that radially oriented MEG sensors are only sensitive to the tangential components of the primary current

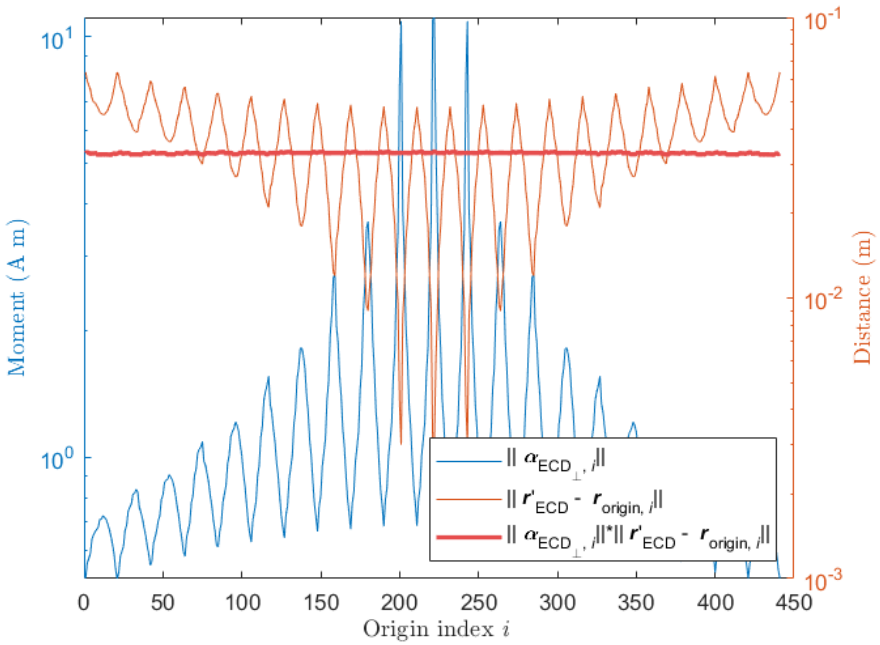

Figure 3.6: For all origins that lie in the current triangle plane, the distance between the origin and ECD fit, $||\mathbf{r}'_{ECD,i} - \mathbf{r}_{origin,i}||$, is inversely proportional to the norm of the ECD moment projected onto the line perpendicular to $\mathbf{r}'_{ECD,i} - \mathbf{r}_{origin,i}$. Since all of these fits have high GOF, it implies there for every origin in the original current triangle's plane, there exists an equivalent current triangle with two radial edges and equivalent surface area that reproduces the reference signal.

[2, 3, 8, 59, 77, 79]. The Sarvas approach of obtaining the full magnetic field via only its radial component (shown in Section 2.1) also leads to a common conclusion that we can reconstruct the entire magnetic field with just the primary current contribution.

However, from our formalism, the above statements are only true when the origin is taken to be at the center of the sphere. We have shown that in a source-less region and under the electro-quasi-static field approximation, an alternative formula to the Biot-Savart law can be derived in which radially-oriented current segments are magnetically silent. A simple shift in origin can thus force volume current segments to become non-radial, meaning that all components of the magnetic field, including the radial component, contain volume current contributions. This is regardless of the head conducting geometry.

In the case of a current triangle for a spherical head model, we have shown that while an origin at the center of the spherical head model results in primary current contributions only ($\mathbf{B}(\mathbf{r}) = \mathbf{b}_{pri}(\mathbf{r})$, $\mathbf{b}_{vol}(\mathbf{r}) = \mathbf{0}$), it is possible to choose an origin that coincides with either of the other two triangle vertices, leading to volume current contributions only ($\tilde{\mathbf{B}}(\tilde{\mathbf{r}}) = \tilde{\mathbf{b}}_{vol}$, $\tilde{\mathbf{b}}_{pri}(\tilde{\mathbf{r}}) = \mathbf{0}$). It is thus possible to obtain the full magnetic field from volume current contributions only at specific choices of origins. The sensitivity of MEG sensors to different components of the underlying current is just a matter of convention of origin choice used in the forward model.

Moreover, as mentioned briefly in Sections 3.2.1 and 3.2.4, this causes misleading physical interpretations of inverse model solutions if the computational origin is not known definitively. For an origin coinciding with a triangle vertex opposite to a volume current edge, an ECD fit localizes the dipole to the volume current edge with high GOF (but significant LE as well) as seen in the right subplot of Figure 3.4. If one were to interpret this fit as a primary current based on the high GOF, it results in an incorrect physical interpretation. Furthermore, in Section 3.2.5, we also observed that for any origin that lies in the plane of the triangle, there are infinite near-perfect dipoles (or, equivalently, current triangles) in the same plane, due to the fact that an arbitrary amount of the magnetically-silent radial dipole moment component (up to the boundary of the head) can be introduced. These equivalent current triangles with

high GOF do not coincide with the primary current edge as can be seen by the high LE in Figure 3.5, and may not necessarily mean anything physically at all. Assigning any meaning to these equivalent currents may again, be misleading.

3.3.2 Co-registration errors and mitigations

In practice, physical misinterpretations are especially relevant in scenarios with a co-registration error, where the reported computational origin does not agree with the true origin. Short, near-radial and/or deep primary current segments are more prone to ECD fit errors and misinterpretations, since a smaller co-registration error may more easily result in the primary current segment becoming radial and magnetically silent.

From Figure 3.5, we see that compared to the plane parallel to the current triangle, co-registration errors in directions perpendicular to the current triangle result in a fast decay of GOF despite having comparable LE. This suggests that for an unconstrained ECD fit, one may (with high caution) infer that there is a co-registration error off the plane of the triangle if the GOF is low. More care may need to be taken to minimize co-registration errors in the plane of the current triangle, since the consistently high GOF provides little information about the LE that may be used for correcting the co-registration error.

In Figure 3.7, we show source configurations that yield equivalent MEG signal contributions in the spherical head case, as well as how short, near-radial and/or deep primary current segments are more sensitive to co-registration errors. In the figure, black colored arrows represent current segments with non-zero MEG signal contributions, whereas gray colored arrows represent radial/magnetically silent current segments. Black colored dots represent the computational origin in question, and a black colored circle represents the corresponding spherical head model that has the black dot located at its center. Gray colored dots and circles represent the computational origin and corresponding spherical head model used in a previous equality. Red dotted arrows represent the origin translations. This figure is an extension of Figure 1.5(d) presented in [63], and similar figures presented in [76, 78].

In order to mitigate the errors of potential co-registration errors, for forward signal

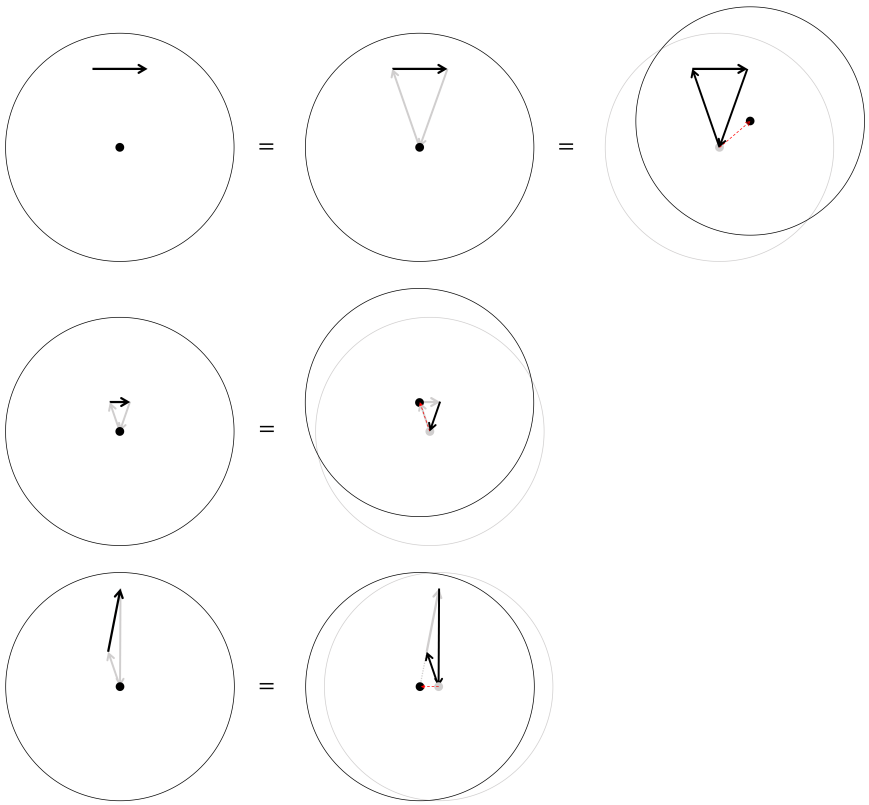

Figure 3.7: (First row) Illustrates two magnetically-silent radial volume current edges being introduced in a spherical head model to form a closed current loop with the primary current. This is equivalent to a translated origin case where all edges are now non-radial; all three edges now have non-zero signal contributions. (Second, third rows) Deep and near-radial current sources are more sensitive to co-registration errors respectively; a small origin translation is sufficient to render them radial and magnetically silent.

calculations, the translational invariance of closed current loop magnetic contributions suggest that the contribution from the entire current should always be considered, instead of just primary (or seemingly non-radial) current segments. This fully mitigates any non-invariant calculations of forward models, even in the event that unknown co-registration errors are present.

For the inverse model, as mentioned in Section 3.2.1, there is in theory an exact N-dipole ECD fit for the signal produced by any closed current loop with N straight edges, though constraints are likely required to find them. Constrained multi-dipole ECD fits may thus be able to mitigate the effects of co-registration errors on ECD fits by accurately identifying (one point of) every primary and volume current segment. Further investigation into multi-dipole fits for current loops is left as future work. Since single dipole ECD fits have been used with success as also mentioned in Section 3.2.1, the effects of co-registration errors as described in this chapter are likely more relevant with deep and near-radial focal neural sources.

3.3.3 Sensor orientations

Our results may also have an influence in deciding sensor orientations. There have been discussions into how radially-oriented sensors have higher sensitivity to primary currents, whereas tangentially-oriented sensors have higher sensitivity to volume currents [18, 74]. It has also been shown that sensor arrays with diversely-oriented sensors improves the performance of source reconstruction and software shielding capabilities [72, 114]. It was suggested that the detection of a mixture of both primary and volume contributions with such a sensor array may be a reason behind the improved performance over arrays with purely radially-oriented sensors [72]. From our discussions above, due to the freedom to choose a computational origin in our formalism, it is possible to alter primary and volume current contributions independently of sensor orientations via origin shifts. Origin choice needs to be taken into consideration, before conclusions about the sensitivity of differently positioned/oriented sensors to primary or volume currents can be made. There is thus room for investigations into the priority of sensors and their orientations for inverse modeling with respect to origin choice.

Chapter 4

NEAR-ANALYTICAL MAGNETIC FLUX CALCULATIONS

As mentioned in the introduction, in order to utilize the increased spatial information provided by MEG signals measured by closer sensors to the head, it is important to investigate whether the accuracy of currently implemented approximation methods can resolve these higher-resolution signals sufficiently. In this chapter, the accuracy of approximations used to calculate the magnetic flux through circular and square pick-up loops is assessed in relation to novel near-analytical methods of magnetic flux evaluations. Due to their equivalence, "signal" and "(magnetic) flux" will be used interchangeably in this chapter.

In MEG, the measured magnetic flux signal through a magnetometer is either the surface integral or volume integral of the magnetic field over the sensor geometry; the former corresponds to SQUID pick-up loops, and the latter corresponds to OPM sensing volumes. Even with the help of computational software, these integrals are difficult to evaluate directly due to their complicated forms, and numerical approximations are hence utilized. However, by their very definition, numerical approximations are not exact and result in forward signal calculation errors. Depending on the method of approximation, these errors may become especially large when considering increasingly spatially complex magnetic fields.

Currently, cubature approximations are used to calculate the signal for MEG pick-up loops (see [1, 26, 74]). That is, the signal is calculated by taking the sum of the integrand evaluated at a discrete number of weighted sampling points across the sensor surface. Although it is possible to improve the accuracy of the approximation by increasing the number of sampling points, this may become increasingly time-consuming, especially when different source configurations are considered and each requires a separate evaluation of the flux. Another issue that may arise when using cubature approximations to sample spatially complex magnetic fields is

aliasing. The distances between the discrete sampling points may fall below the spatial Nyquist sampling rate, and hence high frequency components of the signal may become aliased. This results in artificial low frequency signal patterns, which act as unexplained noise that decreases the forward signal resolutions [132, 147]. Being able to calculate the fluxes analytically without the use of discrete sampling points will avoid this problem entirely.

In this chapter, we first express the quasi-static magnetic field in terms of a VSH basis expansion. The VSH representation decomposes the magnetic field into spatial frequency bands which correspond to the various harmonic l degrees. Then, for each l degree, we show that their flux contribution surface integral can be simplified into a line integral. This allows for an easier evaluation by computational software, as long as the pick-up loop, which can be arbitrarily shaped, has a known parametrization. An iterative method to exactly calculate the flux contribution from each l degree is additionally developed for the special case of circular tangential sensors. Finally, the relative errors of cubature approximations for the flux measured by tangential circular and square sensor are evaluated for each l degree. These relative errors are calculated with respect to exact evaluations of the flux using our analytical formulae.

4.1 Vector spherical harmonic expansion of the magnetic field

In this section, we present the multipolar VSH decomposition of the magnetic field relevant for MEG measurements. As mentioned, the VSH decomposition fundamentally organizes the field into spatial frequency bands. This is similar to the Fourier series, and allows for analyses to be done in the spatial frequency domain.

First, let the field coordinates be $\mathbf{r} = (R, \theta, \phi)$, and let us assume the electro-quasi-static approximation within a source-free region as shown in Chapter 2. Hence, (2.3) holds. Together with $\nabla \cdot \mathbf{B} = 0$ (no magnetic monopoles), this means that the magnetic scalar potential U necessarily satisfies Laplace's equation, i.e., $\nabla^2 U = 0$. When solved in spherical coordinates,

it gives us an expansion of U in terms of (surface) spherical harmonics Y_{lm},

$$U(\mathbf{r}) = \sum_{l=1}^{\infty}\sum_{m=-l}^{l} \alpha_{lm}\frac{Y_{lm}(\theta,\phi)}{R^{l+1}} + \sum_{l=1}^{\infty}\sum_{m=-l}^{l} \beta_{lm}R^{l}Y_{lm}(\theta,\phi), \tag{4.1}$$

where the spherical harmonics are defined by

$$Y_{lm}(\theta,\phi) = \sqrt{\frac{2l+1}{4\pi}\frac{(l-m)!}{(l+m)!}}e^{im\phi}P_l^m(\cos\theta), \tag{4.2}$$

with $l \in \mathbb{N}$, $-l \leq m \leq l$, and P_l^m are the Legendre polynomials defined by

$$P_l^m(x) = \frac{(-1)^m}{2^l l!}(1-x^2)^{m/2}\frac{d^{m+l}}{dx^{m+l}}(x^2-1)^l. \tag{4.3}$$

Notice that $l = 0$ has been excluded in the expansion (4.1) due to the absence of magnetic monopoles. Substituting (4.1) into (2.3) gives us

$$\begin{aligned}\mathbf{B}(\mathbf{r}) &= -\mu_0\sum_{l=1}^{\infty}\sum_{m=-l}^{l}\alpha_{lm}\frac{\boldsymbol{\nu}_{lm}(\theta,\phi)}{R^{l+2}} - \mu_0\sum_{l=1}^{\infty}\sum_{m=-l}^{l}\beta_{lm}R^{l-1}\boldsymbol{\omega}_{lm}(\theta,\phi)\\ &\equiv \mathbf{B}_{in}(\mathbf{r}) + \mathbf{B}_{out}(\mathbf{r}),\end{aligned} \tag{4.4}$$

where the coefficients α_{lm} and β_{lm} (or *multipole moments*), which may be obtained using orthogonality relations of the VSH, are [142]

$$\alpha_{lm} = \frac{i}{2l+1}\sqrt{\frac{l}{l+1}}\int_{v'} R'^{l}\mathbf{X}_{lm}^{*}\cdot\mathbf{J}_{in}\,dv' \equiv \frac{i}{2l+1}\sqrt{\frac{l}{l+1}}A_{\alpha_{lm}}, \tag{4.5}$$

$$\beta_{lm} = \frac{i}{2l+1}\sqrt{\frac{l+1}{l}}\int_{v'} \frac{\mathbf{X}_{lm}^{*}}{R'^{l+1}}\cdot\mathbf{J}_{out}\,dv' \equiv \frac{i}{2l+1}\sqrt{\frac{l+1}{l}}A_{\beta_{lm}}. \tag{4.6}$$

The notations used to define these multipole moment expressions are as follows: i is the imaginary unit, $\boldsymbol{\nu}_{lm}$, $\boldsymbol{\omega}_{lm}$, $\mathbf{X}_{lm}$ are vector spherical harmonics defined as the components of

$\nabla(Y_{lm}/R^{l+1})$ and $\nabla(R^l Y_{lm})$ [69],

$$\begin{aligned}
\boldsymbol{\nu}_{lm}(\theta,\phi) &= -(l+1)Y_{lm}(\theta,\phi)\mathbf{e}_r + \frac{\partial Y_{lm}(\theta,\phi)}{\partial\theta}\mathbf{e}_\theta + \frac{imY_{lm}(\theta,\phi)}{\sin\theta}\mathbf{e}_\phi \\
&\equiv \sqrt{(l+1)(2l+1)}\mathbf{V}_{lm}(\theta,\phi), \qquad (4.7)\\
\boldsymbol{\omega}_{lm}(\theta,\phi) &= lY_{lm}(\theta,\phi)\mathbf{e}_r + \frac{\partial Y_{lm}(\theta,\phi)}{\partial\theta}\mathbf{e}_\theta + \frac{imY_{lm}(\theta,\phi)}{\sin\theta}\mathbf{e}_\phi \\
&\equiv \sqrt{l(2l+1)}\mathbf{W}_{lm}(\theta,\phi), \qquad (4.8)\\
\mathbf{x}_{lm}(\theta,\phi) &= \frac{m}{\sin\theta}Y_{lm}\mathbf{e}_\theta + i\frac{\partial Y_{lm}}{\partial\theta}\mathbf{e}_\phi \\
&\equiv -\sqrt{l(l+1)}\mathbf{X}_{lm}(\theta,\phi), \qquad (4.9)
\end{aligned}$$

and $\mathbf{J}_{in}$ and $\mathbf{J}_{out}$ are source current distributions with radial distance smaller or greater than the sensor array radial distance respectively. We have also defined $A_{\alpha_{lm}}$ and $A_{\beta_{lm}}$ to be the respective volume integrals over the source space in the multipole moment expressions.

Let primed coordinates $\mathbf{r}' = (R', \theta', \phi')$ refer to source coordinates. As hinted by the notations $\mathbf{B}_{in}$, $\mathbf{B}_{out}$, $\mathbf{J}_{in}$ and $\mathbf{J}_{out}$, the first expansions of (4.1) and (4.4), denoted with the subscripts "*in*", correspond to contributions where $R' < R$. In other words, they correspond to contributions from sources within the head, assuming no sources within the sensor-scalp gap. The second expansions, denoted with the subscripts "*out*", correspond to contributions from beyond the sensor array radius where $R' > R$. With the source-less sensor-scalp gap assumption, the second expansion term equivalently corresponds to contributions from all sources outside the head. We can verify this by observing that terms of the first expansion necessarily converge to zero as $1/R^{l+2}$ when $R \to \infty$, whereas terms of the second expansion converge as R^{l-1} when $R \to 0$.

4.1.1 Magnetic flux through planar pick-up loops

In the case of SQUID MEG systems, planar pick-up loops are utilized for signal detection. The magnetic flux signal $\boldsymbol{\Phi}_{surf}$ obtained from such a sensor with surface $\mathcal{C}$ and orientation

$\mathbf{n} = (n_x, n_y, n_z)$ is given by the surface integral of the magnetic field across $\mathcal{C}$,

$$\mathbf{\Phi}_{surf} = \int_{\mathcal{C}} \mathbf{B}(\mathbf{r}) \cdot \mathbf{n} \; dS. \tag{4.10}$$

Similar to (4.4), the flux $\mathbf{\Phi}_{surf}$ may be separated into two components $\mathbf{\Phi}_{in}$ and $\mathbf{\Phi}_{out}$ that correspond to contributions from sources within and outside the head,

$$\begin{aligned} \mathbf{\Phi}_{surf} &= \int_{\mathcal{C}} \mathbf{B}_{in}(\mathbf{r}) \cdot \mathbf{n} \; dS + \int_{\mathcal{C}} \mathbf{B}_{out}(\mathbf{r}) \cdot \mathbf{n} \; dS \\ &\equiv \mathbf{\Phi}_{in} + \mathbf{\Phi}_{out} \\ &= -\mu_0 \sum_{l=1}^{\infty} \sum_{m=-l}^{l} \alpha_{lm} \int_{\mathcal{C}} \frac{\boldsymbol{\nu}_{lm}(\theta, \phi)}{R^{l+2}} \cdot \mathbf{n} \; dS - \mu_0 \sum_{l=1}^{\infty} \sum_{m=-l}^{l} \beta_{lm} \int_{\mathcal{C}} R^{l-1} \boldsymbol{\omega}_{lm}(\theta, \phi) \cdot \mathbf{n} \; dS. \end{aligned} \tag{4.11}$$

This can be written more compactly in matrix form as

$$\mathbf{\Phi}_{surf} = \begin{bmatrix} \mathbf{S}_{in} & \mathbf{S}_{out} \end{bmatrix} \begin{bmatrix} \mathbf{a} \\ \mathbf{b} \end{bmatrix}, \tag{4.12}$$

where

$$\mathbf{S}_{in} = \int_{\mathcal{C}} \left[\frac{\boldsymbol{\nu}_{1,-1}}{R^3} \; , \; \frac{\boldsymbol{\nu}_{1,0}}{R^3} \; , \; \frac{\boldsymbol{\nu}_{1,1}}{R^3} \; , \; \frac{\boldsymbol{\nu}_{2,-2}}{R^4} \; , \; \ldots \right] \cdot \mathbf{n} \; dS, \tag{4.13}$$

$$\mathbf{S}_{out} = \int_{\mathcal{C}} \left[\boldsymbol{\omega}_{1,-1} \; , \; \boldsymbol{\omega}_{1,0} \; , \; \boldsymbol{\omega}_{1,1} \; , \; R\boldsymbol{\omega}_{2,-2} \; , \; \ldots \right] \cdot \mathbf{n} \; dS, \tag{4.14}$$

$$\mathbf{a} = -\mu_0 \left[\alpha_{1,-1} \; , \; \alpha_{1,0} \; , \; \alpha_{1,1} \; , \; \alpha_{2,-2} \; , \; \ldots \right]^T, \tag{4.15}$$

$$\mathbf{b} = -\mu_0 \left[\beta_{1,-1} \; , \; \beta_{1,0} \; , \; \beta_{1,1} \; , \; \beta_{2,-2} \; , \; \ldots \right]^T. \tag{4.16}$$

This matrix representation is the foundation of the Signal Space Separation (SSS) methodology, which was first presented in [142].

In this form, we see that $\mathbf{S}_{in}$ and $\mathbf{S}_{out}$ contain the l degree basis vectors that span the signal subspace due to contributions from sources located inside and outside the head respectively.

Since they are independent of any source coordinates, they can be constructed solely with knowledge about the sensor geometry. On the other hand, the multipole moment vectors $\mathbf{a}$ and $\mathbf{b}$ contain information about the source distribution only.

For a fixed sensor configuration, the basis matrices thus needs to be calculated only once; the forward signal for any source configuration may then be obtained via updating the multipole moments. This is a faster operation than re-calculating the flux whenever the source configuration changes. As such, the elements of the basis matrices are what we aim to accurately calculate. To implement such a forward calculation, the series (4.11) must be truncated at an appropriate degree of $l = L$ such that the signal space is spanned sufficiently accurately by the bases matrices. It has been determined that a truncation degree of $L = 8$ for $\mathbf{S}_{in}$ and $L = 4$ for $\mathbf{S}_{out}$ is sufficient for typical SQUID-based MEG system applications [144].

We are typically only interested in signals due to activity within the head, so from here on, we only consider $\mathbf{S}_{in}$ which specifies $\mathbf{\Phi}_{in}$. The subsequent discussions for the rest of the chapter follow analogously for $\mathbf{S}_{out}$. Denote each entry of $\mathbf{S}_{in}$ as v_{lm}. Converting $\boldsymbol{\nu}_{lm}$ from spherical coordinates to Cartesian coordinates, then carrying out the dot product with sensor orientation $\mathbf{n}$, we have

$$v_{lm} = \int_{\mathcal{C}} \frac{1}{R^{l+2}} \left[-(l+1) Y_{lm} c_R(\theta, \phi) + \frac{\partial Y_{lm}}{\partial \theta} c_\theta(\theta, \phi) + \frac{imY_{lm}}{\sin\theta} c_\phi(\theta, \phi) \right] dS, \tag{4.17}$$

where

$$c_R(\theta, \phi) = n_x \sin\theta \cos\phi + n_y \sin\theta \sin\phi + n_z \cos\theta, \tag{4.18}$$

$$c_\theta(\theta, \phi) = n_x \cos\theta \cos\phi + n_y \cos\theta \sin\phi - n_z \sin\theta, \tag{4.19}$$

$$c_\phi(\theta, \phi) = -n_x \sin\phi + n_y \cos\phi. \tag{4.20}$$

The accurate evaluation of these signal basis matrix elements is beneficial for many applications utilizing the VSH expansion. Most trivially, it allows for a more accurate forward flux

calculation $\mathbf{\Phi}_{in} = \mathbf{S}_{in}\mathbf{a}$ up to truncation degree L (assuming we have knowledge about the source and thus can calculate $\mathbf{a}$). It also provides a more effective filtering of external interferences in SSS applications [142, 144]. The current method to calculate (4.17) is via cubature approximations which results in increasingly inaccurate evaluations of the higher l degree basis vectors as seen in Section 4.7. From Section 4.3 and beyond, improved near-analytical evaluation methods are presented.

In our discussions above, only one sensor has been considered, and so the basis matrix $\mathbf{S}_{in}$ is $1 \times ((L+1)^2 - 1)$-dimensional and the multipole moment vector $\mathbf{a}$ is $((L+1)^2 - 1) \times T$-dimensional, where T is the number of temporal sampling points. This can be extended to more realistic applications with an array of N sensors, where $\mathbf{S}_{in}$ will be $N \times ((L+1)^2 - 1)$-dimensional and $\mathbf{a}$ will be $((L+1)^2 - 1) \times T$-dimensional.

4.1.2 Volumetric magnetic flux through cylindrical sensing volumes

As opposed to a flux measurement across a pick-up loop, the signal measured by OPM sensors is the volumetric flux of the magnetic field across a cylindrical sensing volume $\mathcal{V}$, projected along some sensing direction $\tilde{\mathbf{n}}$. The sensing direction can be modulated and is independent of sensor coordinates. Hence, instead of a surface integral, the volumetric flux is instead obtained via the volume integral

$$\mathbf{\Phi}_{vol} = \int_{\mathcal{V}} \mathbf{B}(\mathbf{r}) \cdot \tilde{\mathbf{n}} dV. \tag{4.21}$$

We may express $\tilde{\mathbf{n}}$ as a rotation of $\mathbf{n}$, i.e. $\tilde{\mathbf{n}} = \mathcal{R}\mathbf{n}$ where $\mathcal{R}$ is a rotation matrix. The rotation matrix can be obtained by using Rodrigues' rotation formula (see Section 4.5), with rotation axis $\mathbf{k} = \mathbf{n} \times \tilde{\mathbf{n}}$ and angle of rotation $\theta_s = \arccos(\mathbf{n} \cdot \tilde{\mathbf{n}}/|\mathbf{n}||\tilde{\mathbf{n}}|)$. So we equivalently have

$$\mathbf{\Phi}_{vol} = \int_{\mathcal{V}} \mathbf{B}(\mathbf{r}) \cdot \mathcal{R}\mathbf{n} dV. \tag{4.22}$$

Furthermore, the cylindrical volume can be discretized into k cross-sectional "slices" of $\mathcal{V}$. The volume integral may thus be approximated as a sum of k surface integrals over cross-sectional

areas $\mathcal{C}_i$, $i = 1, \ldots, k$, multiplied by their thicknesses Δw_i,

$$\mathbf{\Phi}_{vol} \approx \sum_{i=1}^{k} \Delta w_i \int_{\mathcal{C}_i} \mathbf{B}(\mathbf{r}) \cdot \mathcal{R}\mathbf{n} dS. \tag{4.23}$$

This expression, along with the fact that $\mathcal{R}$ has constant entries, mean that the discussions in this chapter which are for pick-up loops may still be used to approximate the volumetric flux that OPMs measure. It is expected that the sum of analytical flux evaluations over cross-sectional areas will yield more accurate results than that of cubature approximations over the cylindrical volume, since the cubature approximation is reduced from three dimensions to one dimension. The l degre truncation required for OPMs is also expected to be higher due to higher signal resolutions as we will discuss in the next section (Section 4.2).

In Section 4.8, we suggest the possibility of using cylindrical harmonics to analytically evaluate the volume integrals for OPMs instead of spherical harmonics, since it may more naturally describe the fields within the cylindrical sensor geometry.

4.2 Higher l degree portions correspond to higher spatial frequency bands

In this section, we discuss how each spherical harmonic l degree in the expansion (4.1) corresponds to spatial frequency bands; the higher the l degree, the higher the spatial frequency.

This may be qualitatively seen from the plots of the real part of spherical harmonic basis modes on a sphere as shown in Figure 4.1. For higher l degrees, the m-order orthonormal basis modes are more spatially complex. The l-degree subspace which they span are thus more spatially complex as well, corresponding to having a higher spatial frequency. Note that negative m-order modes are not shown since they exhibit the same patterns as the positive m-order modes up to a sign flip; by our adopted spherical harmonics definition, $Y_{lm}^* = (-1)^m Y_{l,-m}$. The plots were done with the code provided in [120].

Quantitatively, we know that for some l degree, the spherical harmonics Y_{lm} are the corresponding eigenfunctions to the $-l(l+1)$ eigenvalue of the Helmholtz equation defined with the surface Laplacian operator (or, *Laplace-Beltrami operator*) $\nabla^2_{(\theta,\phi)} = R^2\nabla^2 - R\partial_R^2 R$

[105, 119],

$$\nabla^2_{(\theta,\phi)} Y_{lm} = -l(l+1)Y_{lm}. \tag{4.24}$$

The eigenvalue is the negative squared of the wave number/spatial frequency on a spherical surface [5, 121], thus each l-degree subspace corresponds to the $\sqrt{l(l+1)}$ spatial frequency band. Since the components of an l-degree VSH consist of combinations of these l-degree (scalar) spherical harmonics Y_{lm}, this means that the higher l-degree expansion terms of (4.4) correspond to higher spatial frequency basis modes that span the total magnetic field as well.

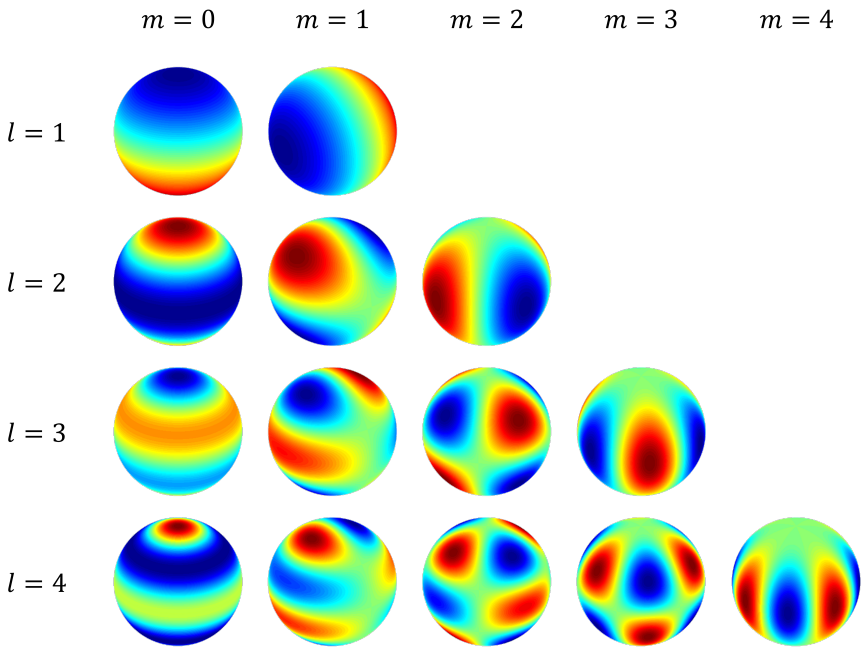

Figure 4.1: Plots of the real part of spherical harmonic modes Y_{lm} on a sphere, from degrees $l = 1$ to $l = 4$. Higher l degree subspaces correspond to higher spatial frequencies, since the orthonormal m-order basis modes that span the space are more spatially complex.

We very briefly note here that determining the spatial frequency bands of each component of the VSH may be a useful contribution towards future work regarding ideal sensor orientations as discussed in Section 3.3.3. It can be seen easily that the radial component of the VSHs are eigenfunctions corresponding to the $-l(l+1)$ eigenvalues of the Helmholtz equation (4.24)

as well, and hence measurements in the radial direction of the magnetic field offer signal resolutions up to the $\sqrt{l(l+1)}$ spatial frequency band for some l. However, the exact spatial frequency bands for the tangential components of the VSHs are less are less clear. As such, further investigations can be made to determine the relative spatial resolutions that each magnetic field component has to offer.

The $1/R^{l+2}$ decay behaviour of each l-degree term in the first expansion of (4.4) tells us that higher spatial frequency components of the magnetic field produced by sources within the head decay quicker as a function of distance. This is the reason why higher resolution signals are expected to be measured for closer sensor array distances to the head; these high spatial frequency components will now be at detectable levels since they have not decayed to be below noise or sensor sensitivity levels. If we let R_1 be a sensor distance that is closer to the head than R_2 ($R_1 < R_2$), then the relative signal amplitude for each l degree for the further sensor compared to the closer sensor is $((1/R_2)/(1/R_1))^{l+2} = (R_1/R_2)^{l+2}$. Since $R_1/R_2 < 1$, this quantity converges to zero as $l \to \infty$.

4.2.1 Improved forward and inverse models

We also present an illustration as to how including higher l degree portions of the basis matrix and multipole moments allow for forward signals with improved spatial resolutions. In turn, improved inverse solutions are expected.

Let us assume a dipolar primary current source, described by (2.29) with $N = 1$. Let us further specify the components of the dipole location and moment as $\mathbf{D} = (a_r, a_\theta, a_\phi)$ and $\mathbf{r}'_D = (R'_D, \theta'_D, \phi'_D)$. Substituting this expression of a dipolar primary source into the multipole moment expression (4.5) gives us

$$\alpha_{lm} = -\frac{iR'^{l}_D}{(2l+1)(l+1)}\left(\frac{ma_\theta}{\sin\theta'_D}Y^*_{lm}(\theta'_D, \phi'_D) - ia_\phi\frac{\partial Y^*_{lm}(\theta'_D, \phi'_D)}{\partial\theta'}\right), \tag{4.25}$$

and a direct evaluation of the spherical harmonic derivative allows us to further express it as

$$\alpha_{lm} = -\frac{iR_D'^l}{(2l+1)(l+1)}\left[\left(\frac{ma_\theta}{\sin\theta_D'} - ia_\phi m\cot\theta_D'\right)Y_{lm}^*(\theta_D',\phi_D') - ia_\phi e^{i\phi_D'}\sqrt{l(l+1)-m(m+1)}\,Y_{l,m+1}^*(\theta_D',\phi_D')\right]. \tag{4.26}$$

Expressions for spherical harmonic derivatives may also be obtained from, for example, [153].

To observe the resolution abilities of each spatial frequency component, a dipole located at $(R_D', \theta_D', \phi_D') = (0.07, \pi/2, \pi)$ with moment $\mathbf{D} = (1,1,1)$ nAm was specified, and the sensor setup used was the standard placement of the 102 magnetometers of the Elekta Neuromag TRIUX system (see Section 3.2.3). The forward signal of the dipole $\boldsymbol{\phi}_l = \mathbf{S}_{in,l}\mathbf{a}_l$ for each $l = 1,\ldots,9$ degree was then calculated. The dipole was then shifted tangentially across the sphere of $r = r_D'$ to obtain the perturbed signal $\boldsymbol{\phi}_l'$. For each l degree portion at each dipole location, the relative error (RE) between $\boldsymbol{\phi}$ and $\boldsymbol{\phi}'$ was calculated using

$$\text{RE} = \frac{\|\boldsymbol{\phi}_l - \boldsymbol{\phi}_l'\|}{\|\boldsymbol{\phi}_l\|}. \tag{4.27}$$

Note that $\mathbf{S}_{in,l}$ was obtained by evaluating (4.13) using a 9-point cubature; it will be shown in Section 4.7 that for such a sensor setup, a 9-point cubature approximation of the basis matrix is still accurate. The multipole moment elements in $\mathbf{a}_l$ were calculated with (4.26).

The colored topographic plots in Figure 4.2 show the RE at each shifted dipole location for the odd l degree signal portions, whereas the grayscale plots show a top-down view of the area of convergence for RE ≤ 0.8 (i.e., the intersection between the topographic RE plots and the $z \leq 0.8$ domain). The location of the original dipole (or "true solution") corresponds to the center of the xy plane, and is marked by a red dot in the area of convergence plots.

We see that for higher l degrees, the steepness of descent into the true solution with zero RE increases, indicating that for a given perturbed dipole position, a larger RE is obtained in general. Conversely, this means that dipolar sources are able to be localized with higher

accuracies for a given error tolerance amount, since a smaller margin of spatial error from the true solution is allowed (represented by the area of convergence). This is, however, assuming an initial guess sufficiently close to the true solution. As mentioned in Section 3.2, the multiple local minima that can be seen from the RE plots (especially for higher l degrees) may result in a mis-localization of the dipole if they have lower values than the specified error tolerance. For instance, we see that in the $l = 9$ disc of convergence plot in Figure 4.2, more than one spatial location has RE ≤ 0.8. Specifying a tolerance of RE $= 0.8$ (which is unrealistically high, but serves as an example) may result in an incorrect dipole localization for initial guesses away from the true solution.

One way to mitigate such a convergence into an incorrect local minima may be exploit the increased smoothness and hence decreased number of local minima for low l-degree RE plots (which can be seen by either observing the topographic plots of Figure 4.2, or noting that they correspond to lower-degree harmonic polynomials). A decreased number of local minima means that an initial guess near the true solution may be more safely obtained by performing an inverse model (with sufficiently low tolerance) on a low l-degree signal portion. This initial guess will then likely fall within the correct area of convergence corresponding to higher l-degree portions, and can then be refined with inverse models on these higher l-degree portions. Utilizing individual l-degree signal portions for inverse modeling is, however, still under study.

4.2.2 Analytical first-order multipole moment errors: an aside

As an aside here, we provide the first-order error expressions of the multipole moments (4.25), which apply for small dipole position displacements.

For a small perturbation in the radial direction, $R'_D \to R'_D + \delta R'$, the multipole moment

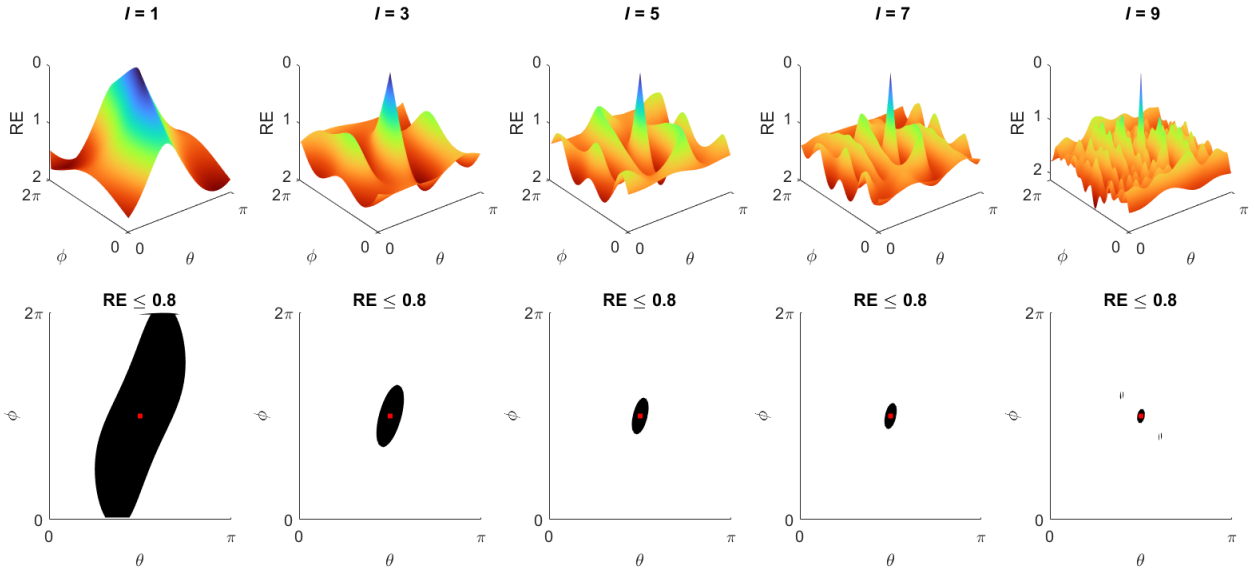

Figure 4.2: (Top row) Topographic plots of l-degree signal RE due to tangentially-displaced dipole positions. The original dipole position corresponds to the center of the xy plane. (Bottom row) Areas of convergence for RE ≤ 0.8. For higher l degrees, the steepness of descent into the true solution increases, corresponding to a smaller area of convergence.

error $\delta\alpha_{lm,R'}$ is approximately

$$\begin{aligned}\delta\alpha_{lm,R'} &\approx \left.\frac{\partial\alpha_{lm}}{\partial R'}\right|_{\mathbf{r}'=\mathbf{r}'_D} \delta R' \\ &= -\frac{ilR_D'^{l-1}\delta R'}{(2l+1)(l+1)}\left[\left(\frac{ma_\theta}{\sin\theta'_D} - ia_\phi m\cot\theta'_D\right)Y^*_{lm}(\theta'_D,\phi'_D)\right. \\ &\quad \left. -e^{i\phi'_D}ia_\phi\sqrt{l(l+1)-m(m+1)}Y^*_{l,m+1}(\theta'_D,\phi'_D)\right]. \end{aligned} \tag{4.28}$$

For a small perturbation of the elevation, $\theta'_D \to \theta'_D + \delta\theta'$, the multipole moment error

$\delta\alpha_{lm,\theta'}$ is approximately

$$\begin{aligned}\delta\alpha_{lm,\theta'} &\approx \left.\frac{\partial\alpha_{lm}}{\partial\theta'}\right|_{\mathbf{r}'=\mathbf{r}'_D}\delta\theta' \\ &= -\frac{iR'^l_D\delta\theta'}{(2l+1)(l+1)} \\ &\quad\cdot\left\{\left[ia_\phi l(l+1)+\frac{ma_\theta\cos\theta'_D}{\sin^2\theta'_D}(m-1)+\frac{ia_\phi m}{\sin^2\theta'_D}\left(\cos^2\theta'_D-m\right)\right]Y^*_{lm}(\theta'_D,\phi'_D)\right. \\ &\quad\left.+\left[e^{i\phi'_D}\sqrt{l(l+1)-m(m+1)}\left(\frac{ma_\theta}{\sin\theta'_D}-ia_\phi\cot\theta'_D\right)\right]Y^*_{l,m+1}(\theta'_D,\phi'_D)\right\}.\end{aligned} \tag{4.29}$$

For a small perturbation in the azimuthal direction $\phi'_D \to \phi'_D + \delta\phi'$, the multipole moment error $\delta\alpha_{lm,\phi'}$ is approximately

$$\begin{aligned}\delta\alpha_{lm,\phi'} &\approx \left.\frac{\partial\alpha_{lm}}{\partial\phi'}\right|_{\mathbf{r}'=\mathbf{r}'_D}\delta\phi' \\ &= -\frac{iR'^l\delta\phi'}{(2l+1)(l+1)}\left[\left(-\frac{ia_\theta m^2}{\sin\theta'_D}-m^2a_\phi\cot\theta'_D\right)Y^*_{lm}(\theta'_D,\phi'_D)\right. \\ &\quad\left.-e^{i\phi'_D}ma_\phi\sqrt{l(l+1)-m(m+1)}Y^*_{l,m+1}(\theta'_D,\phi'_D)\right].\end{aligned} \tag{4.30}$$

The multipole moment error due to an arbitrary small perturbation direction can thus be approximated via the sum of (4.28), (4.29), and (4.30) above,

$$\delta\alpha_{lm} \approx \left.\left(\frac{\partial\alpha_{lm}}{\partial R'}\delta R'+\frac{\partial\alpha_{lm}}{\partial\theta'}\delta\theta'+\frac{\partial\alpha_{lm}}{\partial\phi'}\delta\phi'\right)\right|_{\mathbf{r}'=\mathbf{r}'_D}. \tag{4.31}$$

4.3 Line integral formula for an arbitrary sensor geometry

We now proceed with the goal of presenting near-analytical flux evaluation methods. Here, we convert v_{lm} (4.17) into a line integral formula, which can be more easily evaluated by computer software as long as a parametrization for the pick-up loop boundary can be written.

First, recall that the magnetic vector potential $\mathbf{A}$ is defined as

$$\nabla \times \mathbf{A} = \mathbf{B}. \tag{4.32}$$

If we can find an $\mathbf{A}$, then we can apply Stoke's theorem to convert the flux integral (4.10) to a line integral over the boundary $\partial\mathcal{C}$ of $\mathcal{C}$,

$$\mathbf{\Phi}_{surf} = \oint_{\partial\mathcal{C}} \mathbf{A} \cdot d\mathbf{l} = \int_{t_1}^{t_2} \mathbf{A}\left[\mathbf{r}(t)\right] \cdot \frac{d\mathbf{r}(t)}{dt}\, dt, \tag{4.33}$$

where $d\mathbf{l}$ points along $\partial\mathcal{C}$ in the direction $\mathbf{n}$, and $\mathbf{r}(t) = (r_x(t), r_y(t), r_z(t))$ is a parametrization of $\partial\mathcal{C}$ in $t \in [t_1, t_2]$.

From [69], we know that for some scalar function $f(R)$,

$$\begin{aligned}\nabla \times [f(R)\mathbf{X}_{lm}] = i\sqrt{\frac{l}{2l+1}}\left[\frac{df(R)}{dR} - \frac{l}{R}f(R)\right]\mathbf{V}_{lm} \\ + i\sqrt{\frac{l+1}{2l+1}}\left[\frac{df(R)}{dR} + \frac{l+1}{R}f(R)\right]\mathbf{W}_{lm}.\end{aligned} \tag{4.34}$$

This is in the same form as the expansion terms of the magnetic field (4.4)-(4.6). $A_{\alpha_{lm}}$ and $A_{\beta_{lm}}$ can be treated as constants since they are in the source coordinates and independent of field coordinates. Comparing coefficients gives us

$$\begin{cases} -\mu_0 A_{\alpha_{lm}} \dfrac{1}{R^{l+2}} = \dfrac{df(R)}{dR} - \dfrac{l}{R}f(R) \\ -\mu_0 A_{\beta_{lm}} R^{l-1} = \dfrac{df(R)}{dR} + \dfrac{l+1}{R}f(R) \end{cases}$$

$$\implies f(R) = \frac{\mu_0}{2l+1}\left(\frac{A_{\alpha_{lm}}}{R^{l+1}} - A_{\beta_{lm}}R^l\right) \tag{4.35}$$

$$\implies \mathbf{A}(\mathbf{r}) = \sum_{l=1}^{\infty}\sum_{m=-l}^{l} \frac{\mu_0}{2l+1}\left(\frac{A_{\alpha_{lm}}}{R^{l+1}} - A_{\beta_{lm}}R^l\right)\mathbf{X}_{lm}(\theta,\phi). \tag{4.36}$$

As mentioned in Section 4.1.1, we will consider sources within the head only; calculations hold analogously for sources outside the head. So, we take $A_{\beta_{lm}} = 0$. We will also drop the

"*in*" and "*out*" subscripts from now on, since only the former is relevant.

For an easier dot product evaluation in (4.33), we convert the vector spherical harmonics $\mathbf{x}_{lm} = -\sqrt{l(l+1)}\mathbf{X}_{lm}$ seen in (4.36) into Cartesian coordinates, in agreement with $\mathbf{r}(t)$. We have

$$\mathbf{x}_{lm} = x_1(\theta,\phi)\mathbf{e}_x + x_2(\theta,\phi)\mathbf{e}_y + x_3(\theta,\phi)\mathbf{e}_z, \tag{4.37}$$

where

$$x_1(\theta,\phi) = \left(\frac{mY_{lm}(\theta,\phi)}{\tan\theta}\cos\phi - i\frac{\partial Y_{lm}(\theta,\phi)}{\partial\theta}\sin\phi\right) \tag{4.38}$$

$$x_2(\theta,\phi) = \left(\frac{mY_{lm}(\theta,\phi)}{\tan\theta}\sin\phi + i\frac{\partial Y_{lm}(\theta,\phi)}{\partial\theta}\cos\phi\right) \tag{4.39}$$

$$x_3(\theta,\phi) = -mY_{lm}(\theta,\phi). \tag{4.40}$$

Substituting (4.5) and (4.37)-(4.40) into (4.36), then evaluating (4.33) leads to the flux contribution

$$\mathbf{\Phi}_{lm}^{surf} = (-\mu_0\alpha_{lm})\left[\frac{1}{li}\int_{t_1}^{t_2}\frac{x_1(\theta,\phi)r_x' + x_2(\theta,\phi)r_y' + x_3(\theta,\phi)r_z'}{R^{l+1}}\,dt\right], \tag{4.41}$$

where we have placed the "$surf$" label as a superscript now, and

$$R(t) = \sqrt{r_x^2 + r_y^2 + r_z^2}, \qquad \theta(t) = \arccos\frac{r_z}{\sqrt{r_x^2 + r_y^2 + r_z^2}}, \qquad \phi(t) = \arctan\frac{r_y}{r_x}. \tag{4.42}$$

Note that the prime notation here refers to the time derivative, not source coordinates. Also note that in the evaluation of the coordinate conversions, the arctan function must be defined appropriately to match polar coordinates. In particular, if $r_x < 0$, we need to add or subtract π if $r_y > 0$ or $r_y < 0$ respectively.

It is clear from a comparison between (4.41) and the expansion terms of (4.11) that the

expression contained within the parenthesis of (4.41) are v_{lm},

$$v_{lm} = \frac{1}{li} \int_{t_1}^{t_2} \frac{x_1(\theta,\phi)r'_x + x_2(\theta,\phi)r'_y + x_3(\theta,\phi)r'_z}{R^{l+1}}\, dt. \tag{4.43}$$

If the parametrization $\mathbf{r}(t)$ of the boundary of an arbitrarily-shaped sensor can be written, we are in practice able to find the exact magnetic flux across it by evaluating this line integral. In this form, we have reduced the surface integral (4.17) into a line integral, which helps computing softwares evaluate it more easily. Although most softwares utilize numerical integration methods, a tolerance can be set so that an arbitrary accuracy is obtained. One should note, however, that the integral evaluation for complicated parametrizations may be computationally demanding.

We now focus on rectangular/square and circular sensors respectively, two of the most common sensor geometries. For tangential circular sensors, an additional computationally-efficient analytical recursion is obtained in Section 4.4 by exploiting symmetry.

4.3.1 Rectangular/square sensors

For a rectangular sensor, the line integral (4.33) is the sum of the integrals over the 4 straight edges.

Let the center of the rectangle be $\mathbf{r}_C$, and let X, Y and Z denote the local sensor Cartesian coordinates. The unit basis vectors pointing in the X and Y directions that span the plane containing the flat sensor can be written in terms of the global coordinates as $\mathbf{n}_X = (n_{Xx}, n_{Xy}, n_{Xz})$ and $\mathbf{n}_Y = (n_{Yx}, n_{Yy}, n_{Yz})$, whereas the unit normal $\mathbf{n}_Z = (n_{Zx}, n_{Zy}, n_{Zz})$ is equivalent to $\mathbf{n}$ as defined before in (4.10). Also let the half-width of the pair of edges parallel to $\mathbf{n}_X$ be d_X, and the other pair parallel to $\mathbf{n}_Y$ be d_Y (for square sensors, $d_X = d_Y$.). The coordinates of the 4 corner points of the rectangular sensor can be written as

$$\mathbf{r}_0 = \mathbf{r}_C \pm d_X \mathbf{n}_X \pm d_Y \mathbf{n}_Y, \tag{4.44}$$

and the parametrization for one of the edges is thus

$$\mathbf{r}(t) = \mathbf{r}_0 + \mathbf{n}_\tau t, \qquad t \in [0, 2d_\tau] \tag{4.45}$$

$$\implies \mathbf{r}'(t) = \mathbf{n}_\tau, \tag{4.46}$$

where $\tau = X$ or Y, chosen appropriately depending on which edge we are integrating along. Substituting the parametrization derivative into (4.43), we see that the contribution to v_{lm} from one edge is

$$v_{lm}^{edge} = \frac{1}{li} \int_0^{2d_\tau} \frac{x_1(\theta,\phi)n_{\tau x} + x_2(\theta,\phi)n_{\tau y} + x_3(\theta,\phi)n_{\tau z}}{R^{l+1}}\, dt. \tag{4.47}$$

The sum of 4 such integrals gives v_{lm} for rectangular sensors.

4.3.2 Circular sensors

Let us now consider a circular sensor of radius d and center $\mathbf{r}_C$ lying on a plane spanned by orthogonal unit vectors $\mathbf{v}_1$ and $\mathbf{v}_2$. The parametrization for the circle is given by

$$\mathbf{r}(t) = \mathbf{r}_C + d(\mathbf{v}_1 \cos t + \mathbf{v}_2 \sin t), \qquad t \in [0, 2\pi] \tag{4.48}$$

$$\implies \mathbf{r}'(t) = d(-\mathbf{v}_1 \sin t + \mathbf{v}_2 \cos t), \tag{4.49}$$

which tells us that

$$v_{lm} = \frac{1}{li} \int_0^{2\pi} \frac{x_1(\theta,\phi)r'_x + x_2(\theta,\phi)r'_y + x_3(\theta,\phi)r'_z}{R^{l+1}}\, dt. \tag{4.50}$$

Note that the sine and cosine functions of the parametrization may be interchanged to ensure the correct orientation consistent with the unit normal of the sensor $\mathbf{n}$.

The slightly more complicated form of $\mathbf{r}'(t)$ than the square sensor case may result in a longer computational time for this integral (though still an improvement over a surface integral). In the next section, we show that with the additional assumption of having a

radial unit normal (i.e. tangential circular sensors), a purely recursive formula for v_{lm} can be derived, which allows for a quick computation of v_{lm} without any approximations or numerical integration.

4.4 Analytical recursion formula for tangential circular sensors

Consider again a circular sensor of radius d, but this time with its center lying on the z-axis, $\mathbf{r}_C = (0, 0, r_C)$, and being tangential relative to the origin with $\mathbf{r}_C \cdot \mathbf{n} = r_C$. In this case, $n_x = n_y = 0$ and $n_z = 1$ in equations (4.18)-(4.20), and so (4.17) simplifies to become

$$v_{lm} = \int_{\mathcal{C}} \frac{1}{R^{l+2}} \left[-(l+1) Y_{lm}(\theta, \phi) \cos\theta - \frac{\partial Y_{lm}(\theta, \phi)}{\partial \theta} \sin\theta \right] dxdy, \tag{4.51}$$

where

$$R = \sqrt{x^2 + y^2 + r_C^2}, \qquad \theta = \arccos \frac{r_C}{\sqrt{x^2 + y^2 + r_C^2}}, \qquad \phi = \arctan \frac{y}{x}. \tag{4.52}$$

Again, the arctan function should be defined appropriately.

By symmetry of the $e^{im\phi}$ term in Y_{lm}, one observes that $v_{lm} = 0$ whenever $m \neq 0$. Thus, we may concentrate only on the $m = 0$ case. This reduces the number of terms to evaluate drastically from $(L+1)^2 - 1$ to $L - 1$. Note that this is not true in general for any sensor geometry; it is shown in Section 4.6 that for square sensors, $v_{lm} = 0$ whenever m is not a multiple of 4. Evaluating only the nonzero v_{lm} terms may improve accuracy of flux calculation, since possible computer software round-off errors from calculating the zero terms will be eliminated. Figure 4.3b shows the individual $v_{32,m}$ terms for a tangential circular sensor along the z axis, evaluated using the recursion formulas that are to follow. Indeed, the only the $m = 0$ term is nonzero.

Let us define

$$\gamma_{a,b,u,v} := \int_0^d \frac{\zeta^a}{(\zeta^2 + r_C^2)^{b/2}} P_v^{0,u}\left(\frac{r_C}{\sqrt{\zeta^2 + r_C^2}}\right) d\zeta, \tag{4.53}$$

where a, b, u, v are non-negative integers, and $P_v^{0,u}(x)$ is the u^{th} derivative of $P_v^0(x)$. Note that $\gamma_{a,b,u,v}$ equals 0 whenever $u > v$. By substituting $x = \zeta \cos\psi$ and $y = \zeta \sin\psi$ into (4.51)

and using the identity

$$\frac{\partial Y_{l,0}(\theta,\phi)}{\partial\theta} = \sqrt{l(l+1)}e^{-i\phi}Y_{l,1}(\theta,\phi), \tag{4.54}$$

we see that when $m = 0$,

$$\begin{aligned} v_{l,0} = \sqrt{\frac{2l+1}{4\pi}}\int_0^{2\pi}\int_0^d \frac{1}{(\zeta^2+r_C^2)^{(l+2)/2}}\Bigg[&-(l+1)P_l^0\left(\frac{r_C}{\sqrt{\zeta^2+r_C^2}}\right)\frac{r_C}{\sqrt{\zeta^2+r_C^2}} \\ &- P_l^1\left(\frac{r_C}{\sqrt{\zeta^2+r_C^2}}\right)\frac{\zeta}{\sqrt{\zeta^2+r_C^2}}\Bigg]\zeta\, d\zeta d\psi \\ = 2\pi\sqrt{\frac{2l+1}{4\pi}}&\left(-(l+1)r_C\gamma_{1,l+3,0,l} + \gamma_{3,l+4,1,l}\right). \end{aligned} \tag{4.55}$$

If $l < 1$, then the second term vanishes.

It is now clear that computing $v_{l,0}$ amounts to providing an algorithm to calculate $\gamma_{a,b,u,v}$. Let us recall two well-known recurrences for Legendre polynomials (Bonnet's formulas):

$$P_{l+1}^0(x) = \frac{2l+1}{l+1}xP_l^0(x) - \frac{l}{l+1}P_{l-1}^0(x), \tag{4.56}$$

$$\frac{dP_{l+1}^0(x)}{dx} = (l+1)P_l^0(x) + x\frac{dP_l^0(x)}{dx}. \tag{4.57}$$

From the definition of $\gamma_{a,b,u,v}$, Bonnet's formulas give us the relations

$$\gamma_{a,b,1,l+1} = (l+1)\gamma_{a,b,0,l} + r_C\gamma_{a,b+1,1,l}, \tag{4.58}$$

$$\gamma_{a,b,0,l+1} = \frac{2l+1}{l+1}r_C\gamma_{a,b+1,0,l} - \frac{l}{l+1}\gamma_{a,b,0,l-1}. \tag{4.59}$$

If we repeatedly apply equation (4.58) to itself by substituting the left hand side into the

second term on the right hand side, we have

$$\begin{aligned}\gamma_{a,b,1,l+1} &= (l+1)\gamma_{a,b,0,l} + r_C\gamma_{a,b+1,1,l} \\ &= (l+1)\gamma_{a,b,0,l} + r_C l\gamma_{a,b+1,0,l-1} + r_C^2\gamma_{a,b+2,1,l-1} \\ &= \cdots \\ &= (l+1)\gamma_{a,b,0,l} + r_C l\gamma_{a,b+1,0,l-1} + r_C^2(l-1)\gamma_{a,b+2,0,l-2} + \cdots + r_C^l\gamma_{a,b+l,0,0}. \end{aligned} \tag{4.60}$$

Notice that the last term vanishes ($\gamma_{a,b+l,1,0} = 0$), hence it has been excluded in (4.60). The recursions (4.58) and (4.59) reduce the problem to computing the integrals

$$\gamma_{a,b,0,0} = \int_0^d \frac{\zeta^a}{(\zeta^2 + r_C^2)^{b/2}}\, d\zeta \tag{4.61}$$

and

$$\gamma_{a,b,0,1} = \int_0^d \frac{\zeta^a r_C}{(\zeta^2 + r_C^2)^{(b+1)/2}}\, d\zeta \tag{4.62}$$

$$= r_C\gamma_{a,b+1,0,0}. \tag{4.63}$$

The one-dimensional integral $\gamma_{a,b,0,0}$ (4.61) can be easily evaluated, but we can also give a recipe to recursively compute it more efficiently.

Let us write $\gamma_{a,b} := \gamma_{a,b,0,0}$. By equation (4.55), we also restrict ourselves to the case of $b \geq a+2$. Integration by parts gives

$$\gamma_{a+2,b+2} = \frac{(a+1)}{b}\gamma_{a,b} - \frac{d^{a+1}}{b(d^2 + r_C^2)^{b/2}}, \tag{4.64}$$

so it suffices to compute $\gamma_{1,b}$ and $\gamma_{0,b}$. The former has the form

$$\gamma_{1,b} = -\frac{1}{b-2}\left(\frac{1}{(d^2 + r_C^2)^{(b-2)/2}} - \frac{1}{r_C^{b-2}}\right), \tag{4.65}$$

whereas the latter can be found by substituting $\zeta = r_C \tan\omega$ into (4.61) to give

$$\gamma_{0,b} = \frac{1}{b-2}\left(\frac{b-3}{r_C^2}\gamma_{0,b-2} + \frac{d}{r_C^2(d^2+r_C^2)^{(b-2)/2}}\right), \qquad b \geq 4, \tag{4.66}$$

with base cases

$$\gamma_{0,2} = \frac{1}{r}\arctan\left(\frac{d}{r_C}\right), \qquad \gamma_{0,3} = \frac{d}{r_C^2\sqrt{d^2+r_C^2}}. \tag{4.67}$$

Equations (4.55), (4.59), (4.60), (4.63)-(4.67), when evaluated in reverse order, provide an efficient way to recursively compute v_{lm} analytically as desired.

To generalize the above to sensors not aligned on the z axis, we may passively rotate the $\mathbf{B}$ field so that the z axis now aligns with the center of the new sensor. This is shown in the next section (Section 4.5). The same recursion formulas can still be used; only the coefficients of the recursive form of v_{lm} (4.55) are changed.

4.5 Passive rotations of vector fields

The rotation matrix $\mathcal{R}$ for a proper rotation about the axis $\mathbf{k} = (k_x, k_y, k_z)$, $|\mathbf{k}| = k = 1$, by an angle γ can be written using Rodrigues' rotation formula [16],

$$\mathcal{R} = \begin{bmatrix} \cos\gamma + k_x^2(1-\cos\gamma) & k_xk_y(1-\cos\gamma) - k_z\sin\gamma & k_xk_z(1-\cos\gamma) + k_y\sin\gamma \\ k_yk_x(1-\cos\gamma) + k_z\sin\gamma & \cos\gamma + k_y^2(1-\cos\gamma) & k_yk_z(1-\cos\gamma) - k_x\sin\gamma \\ k_zk_x(1-\cos\gamma) - k_y\sin\gamma & k_zk_y(1-\cos\gamma) + k_x\sin\gamma & \cos\gamma + k_z^2(1-\cos\gamma) \end{bmatrix}. \tag{4.68}$$

Since we aim to passively rotate $\mathbf{B}$ such that the z axis coincides with an arbitrary tangential sensor, $\mathbf{B}$ is rotated with $\mathcal{R}^{-1}$ instead of $\mathcal{R}$. The sensor coordinates must be rotated by $\mathcal{R}$ as well, so that the field coordinates still line up correctly with the passively rotated magnetic field. Let the sensor be located at $\mathbf{r}_s = (R_s, \theta_s, \phi_s)$ (Cartesian coordinates $\mathbf{r}_s = (x_s, y_s, z_s)$). The rotation axis $\mathbf{k}$ is obtained via the normalized cross product between $\mathbf{r}_s$ and $\mathbf{e}_z$, and

always lies on the xy plane with $k_z = 0$. Thus, (4.68) simplifies to become

$$\mathcal{R} = \begin{bmatrix} \cos\theta_s + k_x^2(1-\cos\theta_s) & k_x k_y(1-\cos\theta_s) & k_y \sin\theta_s \\ k_y k_x(1-\cos\theta_s) & \cos\theta_s + k_y^2(1-\cos\theta_s) & -k_x \sin\theta_s \\ -k_y \sin\theta_s & k_x \sin\theta_s & \cos\theta_s \end{bmatrix}. \tag{4.69}$$

The passively rotated $\mathbf{B}$ field is given by $\mathcal{R}^{-1}\mathbf{B}(\mathcal{R}\mathbf{r})$.

4.5.1 Passive rotation of v_{lm} for tangential circular sensors along z-axis

Now, consider some tangential circular sensor $\mathcal{C}$ located at $\mathbf{r}_s = (R_s, \theta_s, \phi_s)$. If we align the z axis along this sensor via a passive rotation of the $\mathbf{B}$ field as described above, v_{lm} (4.17) becomes

$$\begin{aligned} v_{lm} = \int_{\mathcal{C}} \frac{1}{R^{l+2}} \Big[& \mathcal{R}_{31}^{-1} \left(B_1 \sin\theta_s \cos\phi_s + B_2 \cos\theta_s \cos\phi_s - B_3 \sin\phi_s\right) \\ & + \mathcal{R}_{32}^{-1} \left(B_1 \sin\theta_s \sin\phi_s + B_2 \cos\theta_s \sin\phi_s + B_3 \cos\phi_s\right) \\ & + \mathcal{R}_{33}^{-1} \left(B_1 \cos\theta_s - B_2 \sin\theta_s\right) \Big] dS, \end{aligned} \tag{4.70}$$

where $\mathcal{R}_{ij}^{-1}$ is the ij^{th} entry of $\mathcal{R}^{-1}$, and

$$B_1 = -(l+1) Y_{lm}(\theta_s, \phi_s) \tag{4.71}$$

$$B_2 = \frac{\partial Y_{lm}(\theta_s, \phi_s)}{\partial \theta} = \frac{\partial Y_{lm}(\theta_s, \phi_s)}{\partial \theta_s} \frac{d\theta_s}{d\theta} \tag{4.72}$$

$$B_3 = \frac{imY_{lm}(\theta_s, \phi_s)}{\sin\theta_s}. \tag{4.73}$$

The integral (4.70) can be simplified by observing that due to the symmetry of the circle, integrals over terms explicitly dependent on $\sin\phi_s$ and $\cos\phi_s$ vanish. Thus, the first two integrand terms vanish. Moreover, if we denote $\mathcal{R}_{ij}$ as the ij^{th} entry of $\mathcal{R}$, an explicit

evaluation tells us that $d\theta_s/d\theta = \mathcal{R}_{22}$. So, we get

$$v_{lm} = \int_{\mathcal{C}} \frac{\mathcal{R}_{33}^{-1}}{R^{l+2}} \left[-(l+1) Y_{lm}(\theta_s, \phi_s) \cos\theta_s - \mathcal{R}_{22} \frac{\partial Y_{lm}(\theta_s, \phi_s)}{\partial \theta_s} \sin\theta_s \right] dS. \tag{4.74}$$

Recall from the previous section (Section 4.4) the notation $\gamma_{s,t,u,v}$, as well as the fact that we are only interested in $m = 0$ terms since they are the only terms that are possibly nonzero. Then, the passively rotated v_{l0} can be written as

$$v_{l,0} = 2\pi \sqrt{\frac{2l+1}{4\pi}} \mathcal{R}_{33}^{-1} \left(-(l+1) r_C \gamma_{1,l+3,0,l} + \mathcal{R}_{22} \gamma_{3,l+4,1,l} \right). \tag{4.75}$$

This is exactly the form of (4.55), only with different coefficients. The flux through sensors not aligned on the z axis can thus be obtained with the same recurrences established in Section 4.4, if they are rotation to align with the z axis.

4.6 Nonzero v_{lm} terms for tangential square sensors along the z-axis

For tangential square sensors along the z axis, a clean recursive formula seems to be difficult to obtain, but useful comments can still be made about which v_{lm} terms are nonzero based on symmetry. Similar to the passive rotation of the $\mathbf{B}$ field as discussed in Section 4.5, arbitrary tangential square sensors can be aligned with the z axis via a passive rotation of the magnetic vector potential $\mathbf{A}$. This allows for a line integral evaluation of the magnetic flux in the form of (4.33).

In this section, we show that for tangential square sensors centered along the z-axis, $v_{lm} = 0$ in the following two cases: when m is odd, and when $m = 2k$, where k is an odd integer satisfying $0 < |2k| \leq l$. In other words, v_{lm} can be nonzero only when m is a multiple of 4 (with $0 \leq |m| \leq l$). This cuts down the number of v_{lm} terms required to be evaluated from $(L+1)^2 - 1$ to $\sum_{l=1}^{L} (2\lfloor l/4 \rfloor + 1)$. Intuitively, this result follows from the dihedral D_4 symmetry of the square, but we will justify this assertion explicitly here.

Consider a tangential square sensor with half-width d along the z axis, similar to the setup in the previous section (Section 4.4). Equation (4.51) for v_{lm} thus holds, except with $\mathcal{C}$

being the square area.

First, let us assume that m is odd. Then, pick four points on the square sensor, $P_1 = (x, y)$, $P_2 = (-x, y)$, $P_3 = (-x, -y)$, and $P_4 = (x, -y)$, with P_1 lying in the first quadrant. The only difference in the integrand of (4.51) at these four points is the exponential portions dependent on ϕ in Y_{lm}. Denote the exponential portions for each of the four points as $e_{P_\xi} = e^{im\phi_{P_\xi}}$, where $\xi = 1, ..., 4$, and ϕ_{P_ξ} is calculated using (4.52). It is clear that for odd m, we have

$$
\begin{aligned}
e_{P_1} &= \cos(m\phi_{P_1}) + i\sin(m\phi_{P_1}) \\
e_{P_2} &= \cos(m(\pi - \phi_{P_1})) + i\sin(m(\pi - \phi_{P_1})) = -\cos(m\phi_{P_1}) + i\sin(m\phi_{P_1}) \\
e_{P_3} &= \cos(m(\pi + \phi_{P_1})) + i\sin(m(\pi + \phi_{P_1})) = -\cos(m\phi_{P_1}) - i\sin(m\phi_{P_1}) \\
e_{P_4} &= \cos(m(2\pi - \phi_{P_1})) + i\sin(m(2\pi - \phi_{P_1})) = \cos(m\phi_{P_1}) - i\sin(m\phi_{P_1}).
\end{aligned}
$$

The sum of these four integrands is zero, hence it is clear that (4.51) is zero for odd m due to the symmetry of the square.

Now, assume $m = 2k$, where k is an odd integer satisfying $0 < |2k| \leq l$. As before, pick any point $P_1 = (x, y)$ in the first quadrant of the square. Instead of obtaining the three other points by reflections, we obtain P_2, P_3, P_4 by rotating P_1 counterclockwise about the origin by an angle of $\frac{\pi}{2}, \pi, \frac{3\pi}{2}$ respectively. Notice once again that the only difference in the integrand of (4.51) is the exponential term e_{P_ξ}. In this case,

$$
\begin{aligned}
e_{P_1} &= e^{2ik\phi_{P_1}} && (4.76) \\
e_{P_2} &= e^{2ik(\pi/2+\phi_{P_1})} = e^{ik\pi} e_{P_1} = -e_{P_1} && (4.77) \\
e_{P_3} &= e^{2ik(\pi+\phi_{P_1})} = e^{2ik\pi} e_{P_1} = e_{P_1} && (4.78) \\
e_{P_4} &= e^{2ik(3\pi/2+\phi_{P_1})} = e^{3ik\pi} e_{P_1} = -e_{P_1}, && (4.79)
\end{aligned}
$$

which means the sum of the four integrands equals zero again. Hence, (4.51) is zero for $m = 2k$, where k is an odd integer,

The above arguments do not apply when m is a multiple of 4, including $m = 0$. Figure 4.3a

shows the individual $v_{32,m}$ terms for a tangential square sensor along the z axis, evaluated using the line integral (4.47). Indeed, the only nonzero terms are when m is a multiple of 4, including $m = 0$.

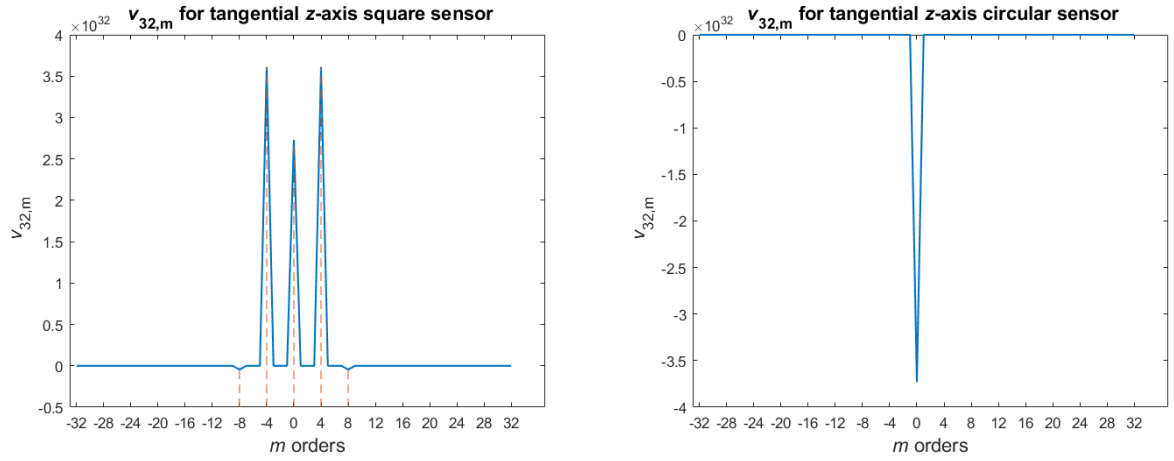

(a) (b)

Figure 4.3: Plots of $v_{32,m}$ terms for: (a) a tangential square sensor, and (b) a tangential circular sensor, both on the z-axis. For the square sensor, $v_{32,m} \neq 0$ only when m is a multiple of 4, including $m = 0$. For the circular sensor, $v_{32,0}$ is nonzero.

4.7 Cubature approximation errors

In Sections 4.3 and 4.4, we have presented methods offering (near)-analytical evaluations of v_{lm}. The former applies for arbitrary pick-up loops with parametrizations that can be found, whereas the latter applies for tangential circular sensors. In this section, we show the results when these analytical methods are utilized to determine the relative errors (RE) for cubature approximations of v_{lm}. Similar to (4.27), the RE in this section is defined as

$$\mathrm{RE} = \frac{\|v_{lm}^a - v_{lm}^c\|}{\|v_{lm}^a\|}, \tag{4.80}$$

where v_{lm}^a and v_{lm}^c denote the (near)-analytical evaluations and cubature approximations of v_{lm} respectively.

Let us consider the simple cases of tangential square sensors and tangential circular sensors oriented along the z-axis. For the circular sensors, the recursions in Section 4.4 were used to obtain fully analytical calculations of v_{lm}. For square sensors, the line integral (4.47) was evaluated using Matlab's default numerical integration. It was observed that using the default tolerance yielded the same results as having a decreased tolerance, hence the former was used since it appears to be accurate and near-analytical.

The sampling points and weights of various cubature approximations were obtained from Section 25.4 of [1]. Namely, we considered 4- and 9-point cubatures for square sensors, and 4-, 7- and 21-point cubatures for circular sensors. In addition, for both sensor geometries, we also considered a 1-point cubature with the sampling point located at the center of the sensor; this is a common approximation, since point-like sensors are frequently assumed.

We will only evaluate $v_{l,0}$ terms, since it has been determined in Section 4.4 that only $m = 0$ terms are possibly nonzero for tangential circular sensors. Unless explicitly stated, the distance of the sensor from the origin is $r_C = 9$ cm, which corresponds to the average size of an adult head, and the half-width/radius of the sensor is $d = 1$ cm, approximately the half-width of the square pick-up loops of the Elekta Neuromag TRIUX system.

4.7.1 Errors for each l degree

In Figure 4.4, the cubature approximation errors of $v_{l,0}$ for various l degrees are shown. We see that utilizing fewer sampling points yielded the greatest errors, and higher l degree/higher spatial frequency terms had higher RE. This is expected given that discrete sampling points become increasingly inaccurate in sampling more spatially complex signal portions.

Recall from Section 4.1.1 that an $L = 8$ truncation degree has been determined to be sufficient for most SQUID-based applications [144]. From our plots however, we see that for point-like approximations of $v_{6,0}$, significant RE of around 0.16 and 0.11 for square and circular sensors respectively are already seen. This indicates that even for current SQUID sensors, using point-like sensor approximations may introduce significant errors in flux calculations.

The errors for the other cubatures remain relatively small (RE $\leq 10^{-2}$) up to $l = 8$.

However, up to $l = 20$, only the 9-point cubature for square sensors, and 7- and 21-point cubatures for circular sensors have small errors with RE < 0.02. This means that utilizing 1- and 4-point cubature approximations will likely result in inaccurate high resolution flux calculations that require higher L-degree truncations, e.g. OPM signals.

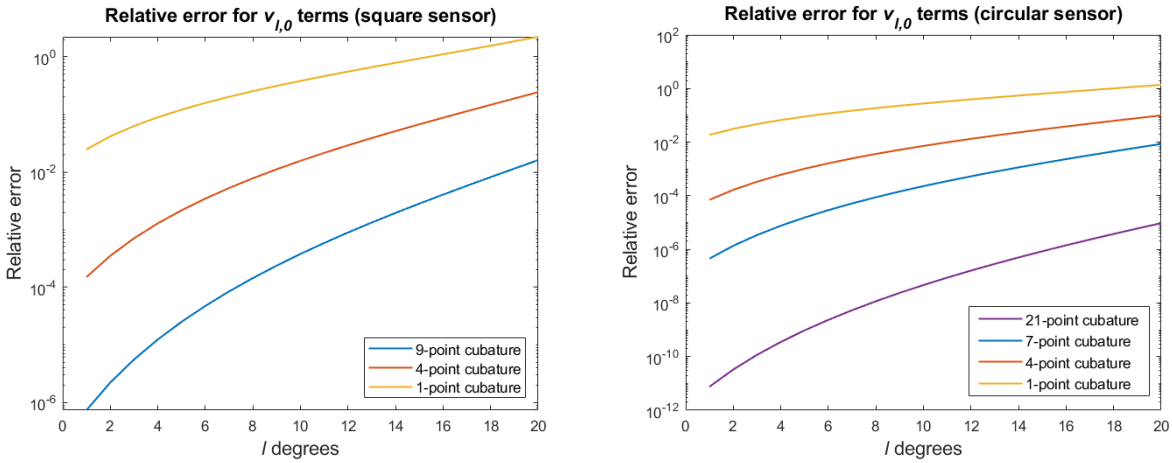

(a) (b)

Figure 4.4: Relative error plots of $v_{l,0}$ for a (a) tangential square sensor and (b) tangential circular sensor, both located on the z-axis. The errors increase as l increases, which means that cubature approximations of higher frequency signal portions become increasingly inaccurate. Fewer sampling points result in larger errors as well.

4.7.2 Varying sensor distances

As discussed in Section 4.1, reduced brain-to-sensor distances allow us to detect higher l degree signal portions. According to the results of Figure 4.4 then, we expect a higher RE for closer sensor distances due to the inclusion of these increasingly inaccurately approximated high frequency portions. Here, we additionally show that l degree signal portions at closer sensor distances have increasing cubature approximation errors as well. There are thus two factors at play that contribute to increased cubature errors for closer sensor array distances: the inclusion of more inaccurate higher frequency terms, and each frequency term becoming more inaccurate themselves.

Figure 4.5 shows the cubature approximation REs of the $l = 8$ signal portion, $v_{8,0}$, at sensor distances $r_C = 5$ cm to $r_C = 10$ cm. This range is approximately applicable for all head sizes from infants to adults.

We see that for the $l = 8$ signal portion, there is a significant error of RE > 0.4 for the point-like square and circular sensors that are located at around 6 cm from the origin. Such sensor distances correspond to the approximate size of an infant head. A truncation degree of $L > 8$ is required for these sensor distances, since the usual $L = 8$ truncation was determined using sensor distances corresponding to average adult head sizes. Together with the results of Figure 4.4, this suggests that for infant MEG measurements with sensors that can be placed close to the head (and having $d \approx 1$ cm), point-like approximations of the flux may be highly inaccurate. The important high-frequency components beyond $L = 8$ may be especially inaccurate, with RE much larger than 0.4. In turn, the spatial resolution of inverse source estimates may be significantly compromised.

As before, the 9-point cubature for square sensors and 7- and 21-point cubatures for circular sensors had small errors for all sensor distances, with RE < 0.02.

4.7.3 Varying sensor sizes

Here, we verify that having closer cubature sampling points results in more accurate $v_{l,0}$ signal portion calculations. The half-width of the square sensor and radius of the circular sensor sizes was varied from $d = 0.25$ cm to $d = 2.5$ cm. A decreased sensor size means that the sampling points become closer to each other, and hence they are expected to resolve higher spatial frequency components more accurately with lower RE. Figure 4.6 verifies this with plots of $v_{8,0}$ cubature errors as a function of sensor size.

We see that when $d \approx 0.5$ cm, the cubature error for a tangential circular sensor at $r_C = 9$ cm has a RE of less than 0.01. Recent OPM sensor considerations have cylindrical cap surfaces with $d \approx 0.5$ cm to $d \approx 1$ cm [70, 74], which are smaller than typical SQUID pick-up loops. This feature may thus mitigate the increased cubature errors that are to be expected for due to the factors discussed in the previous sections (namely, having closer

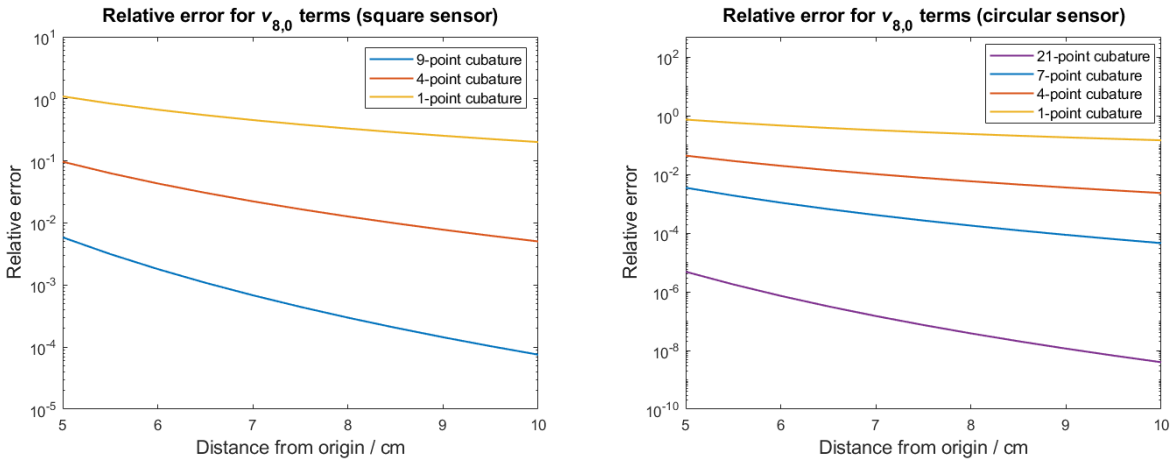

(a) (b)

Figure 4.5: Relative error plots of $v_{8,0}$ for a (a) tangential square sensor and (b) tangential circular sensor with varying distances from the origin, both located on the z-axis. The error of l degree signal portions increase as the sensor is placed closer to the origin.

sensor distances and increasingly inaccurate higher frequency components).

4.7.4 Comments

All the results in this section demonstrate that a higher number of cubature points results in decreased cubature errors. This is due to their reduced distances from each other, which allows for an increased accuracy when sampling a given spatial frequency signal component. It is thus recommended that one implements cubature approximations with a large number of sampling points, or calculates the flux (near)-exactly using our formulas whenever possible. (Near)-exact flux evaluations will always be more advantageous however; they have the added benefits of entirely eliminating the possibility of signal aliasing, as well as ensuring that the important higher spatial frequency components that ensure higher inverse model resolutions (see Section 4.2.1) are accurately evaluated.

Our results also indicate that for current SQUID-based MEG setups, the 9-point cubature for square sensors and 7-point cubature for circular sensors seem to provide sufficiently accurate evaluations of the signal. However, for OPM-based systems which are able to

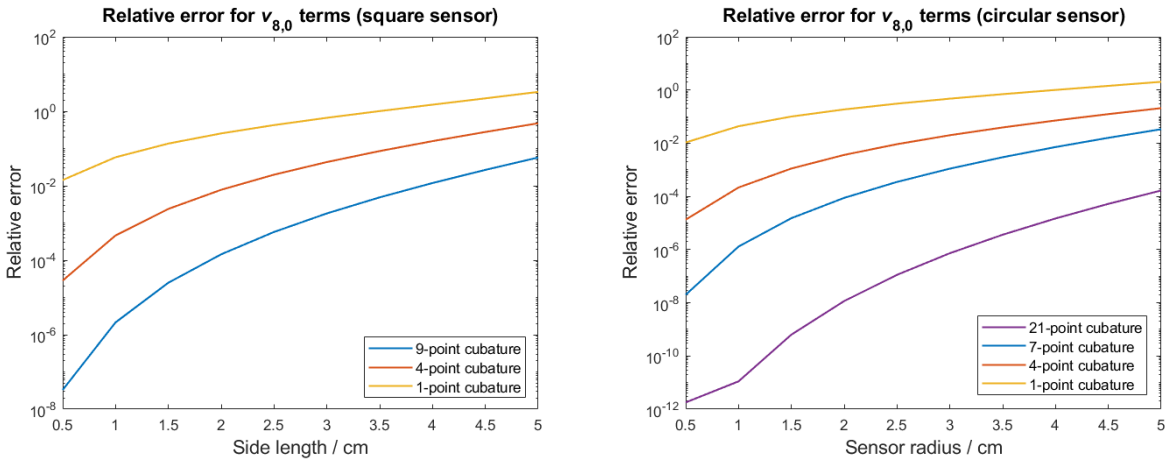

(a) (b)

Figure 4.6: Relative error plots of $v_{8,0}$ for a (a) tangential square sensor and (b) tangential circular sensor with varying sensor sizes. The errors increase as side length increases, since the sampling points are further apart and hence resolve the given spatial frequency component with decreased accuracies.

detect higher frequency components and can be placed directly on the head, these cubature approximations (and thus inverse models performed with them) will likely become increasingly inaccurate. This may become an increasingly crucial issue especially for OPM-based on-scalp infant MEG, since source mis-localizations have more severe implications relative to smaller heads/brains (e.g. they may point to an entirely different brain region of interest).

Note that a verification that increasingly inaccurate signals result in increasingly inaccurate source localizations can be seen via the noiseless case example presented in 5.3.

4.8 Cylindrical harmonics

As additional consideration, we present a possible starting point for flux calculations in cylindrical harmonics here. Since OPM-based systems typically utilize cylindrical sensing volumes, cylindrical harmonics may offer a more natural description of the signals than spherical harmonics.

We first state the following expressions from [71, 84] that convert the (solid) spherical

harmonics into cylindrical harmonics,

$$\begin{aligned}\frac{Y_{lm}(\theta,\phi)}{R^{l+1}} &= \frac{c_{lm}}{(l-m)!}e^{im\phi}\int_0^\infty \lambda^l e^{-\lambda z} J_m(\lambda\rho)\ d\lambda \\ &\equiv \frac{c_{lm}}{(l-m)!}e^{im\phi}K_{lm}(\rho,z) \qquad (4.81)\\ R^l Y_{lm}(\theta,\phi) &= \frac{c_{lm}(l-m)!}{2\pi i}e^{im\phi}\int_0^\infty \frac{e^{\lambda z}}{\lambda^{l+1}} J_m(\lambda\rho)\ d\lambda \\ &\equiv \frac{c_{lm}(l-m)!}{2\pi i}e^{im\phi}L_{lm}(\rho,z). \qquad (4.82)\end{aligned}$$

In these expressions, $(\rho,\phi,z) = (R\sin\theta, \phi, R\cos\theta)$ are the cylindrical coordinates, c_{lm} are the spherical harmonic coefficients as seen in (4.2), J_m are Bessel functions of the first kind, and K_{lm} and L_{lm} are the definite integrals defined in the first and second expressions respectively. One can arrive at these expressions by solving Laplace's equation in cylindrical coordinates – see for example [80].

Substituting these conversions into the magnetic scalar potential expansion (4.1) gives us

$$U(\mathbf{r}) = \sum_{l=1}^{\infty}\sum_{m=-l}^{l}\alpha_{lm}\frac{c_{lm}}{(l-m)!}e^{im\phi}K_{lm}(\rho,z) + \sum_{l=1}^{\infty}\sum_{m=-l}^{l}\beta_{lm}\frac{c_{lm}(l-m)!}{2\pi i}e^{im\phi}L_{lm}(\rho,z). \quad (4.83)$$

Observe that

$$\nabla\left(e^{im\phi}K_{lm}\right) = e^{im\phi}\left(\frac{\partial K_{lm}}{\partial\rho}\hat{\boldsymbol{\rho}} + \frac{im}{\rho}K_{lm}\hat{\boldsymbol{\phi}} - K_{l+1,m}\hat{\mathbf{z}}\right) \equiv \mathbf{K}_{l+1,m} \quad (4.84)$$

$$\nabla\left(e^{im\phi}L_{lm}\right) = e^{im\phi}\left(\frac{\partial L_{lm}}{\partial\rho}\hat{\boldsymbol{\rho}} + \frac{im}{\rho}L_{lm}\hat{\boldsymbol{\phi}} + L_{l-1,m}\hat{\mathbf{z}}\right) \equiv \mathbf{L}_{l-1,m}, \quad (4.85)$$

where we have defined $\mathbf{K}_{lm}$ and $\mathbf{L}_{lm}$ as the vector cylindrical harmonics. The derivatives of K_{lm} and L_{lm} with respect to ρ can be evaluated using

$$\frac{d}{d\rho}J_m(\lambda\rho) = \frac{d}{d(\lambda\rho)}\frac{d(\lambda\rho)}{d\rho}J_m(\lambda\rho) = \frac{\lambda}{2}\left(J_{m-1}(\lambda\rho) - J_{m+1}(\lambda\rho)\right), \quad (4.86)$$

which gives

$$\frac{\partial K_{lm}}{\partial \rho} = \frac{1}{2}\left[K_{l+1,m-1} - K_{l+1,m+1}\right] \tag{4.87}$$

$$\frac{\partial L_{lm}}{\partial \rho} = \frac{1}{2}\left[L_{l-1,m-1} - L_{l-1,m+1}\right]. \tag{4.88}$$

The magnetic field is thus

$$\mathbf{B}(\mathbf{r}) = -\mu_0 \sum_{l=1}^{\infty}\sum_{m=-l}^{l} \alpha_{lm}\frac{c_{lm}}{(l-m)!}\mathbf{K}_{l+1,m}(\rho,\phi,z) - \mu_0 \sum_{l=1}^{\infty}\sum_{m=-l}^{l} \beta_{lm}\frac{c_{lm}(l-m)!}{2\pi i}\mathbf{L}_{l-1,m}(\rho,\phi,z). \tag{4.89}$$

Let us assume a cylindrical sensor aligned along the z-axis, i.e., the axis that passes through the center of the cylinder caps aligns with the z axis (as discussed in Section 4.5, we can passively rotate the magnetic field to align the z axis with any tangential cylindrical sensor). Then, we can reduce the volume integral into a surface integral by evaluating out the integral with respect to z from the lower cylinder cap at $z = z_1$ to the upper cap at $z = z_2$,

$$\begin{aligned}\mathbf{\Phi}_{surf}(\mathbf{r}) = \Bigg[&\mu_0 \sum_{l=1}^{\infty}\sum_{m=-l}^{l} \alpha_{lm}\int_{\mathcal{C}} \frac{c_{lm}}{\lambda(l-m)!}\mathbf{K}_{lm}(\rho,\phi,z)\cdot\tilde{\mathbf{n}}\, dS \\ &- \mu_0 \sum_{l=1}^{\infty}\sum_{m=-l}^{l} \beta_{lm}\int_{\mathcal{C}} \frac{c_{lm}(l-m)!}{2\lambda\pi i}\mathbf{L}_{lm}(\rho,\phi,z)\cdot\tilde{\mathbf{n}}\, dS\Bigg]\Bigg|_{z=z_1}^{z_2}.\end{aligned} \tag{4.90}$$

This is a similar form to (4.11); if one were to utilize the SSS formalism in cylindrical harmonics, the elements of the basis matrices are similarly specified by the surface integrals. Evaluating these surface integrals in a simpler way is a topic for future study.

Chapter 5

EFFECTS OF INACCURATE HEAD MODELS ON FORWARD AND INVERSE MODEL ACCURACIES

Geselowitz's formula, which was presented in Section 2.2.2, tells us that for a head that is modeled as a bounded conductor with piecewise homogeneous conductivities, the volume currents are mathematically equivalent to surface currents that lie on the conductivity boundaries [49]. Any inaccuracies in the head model is thus equivalent to inaccuracies in the volume current model, resulting in forward model errors. We also know from Section 4.2.1 that closer sensor arrays measure higher resolution signals.

These two pieces of information when combined together tell us that one may need to become increasingly vigilant in constructing accurate head models for closer sensor arrays. Not only will the primary current contributions be measured with higher resolutions, any inaccurate volume current contributions due to inaccurate head models will be measured with higher resolutions as well. Due to exact volume current contributions towards signals being non-trivial for arbitrary head geometries (as will be elaborated further in Section 5.1, and also as expected by the discussion in Section 2.2.5 about constructing current loops), it is not immediately obvious to what extent the amount of head model errors affects the signal error for varying sensor array distances. In this chapter, we attempt to elucidate this issue.

First, an overview of boundary element method (BEM) is presented. BEM triangularizes the head model, and allows for a way for us to estimate the volume current contribution to the signal. Then, to simulate inaccurate head models, we perturbed the vertices of a spherical BEM head model, and determined the resulting signal error and ECD source localization errors for varying sensor array distances. Errors for various spatial frequency bands are also investigated via the VSH expansion formalism as shown in Section 4.1. Finally, an analytical

expression for the first-order signal error due to a small vertex perturbation (and conductivity perturbation) is presented for our BEM choice.

In literature, there have been a few studies done that address similar concerns, although in less general ways. For instance, studies on head geometry errors have been done with focus on the skull [27, 94], or with the assumption that the head model errors are sufficiently smooth such that they can be accurately described with a spherical harmonic expansion [112]. Since our approach accounts for individual perturbations to the head model vertices, it may offer a solution to more precise corrections to discretized head models.

We note that there are many other sources of errors for BEM in addition to the geometrical head model errors that we consider in this chapter. These errors can be broadly categorized as anatomical modeling errors and/or numerical errors, with geometrical head model errors falling into the former category. Anatomical errors also include conductivity errors [65, 134, 137, 149], and numerical errors include different mesh triangulation methods and the various methods of estimating the electric potential within each triangle [104, 129]. An overview of many of these errors can be found in [39].

We also briefly note here that it may be possible to develop an algorithm to construct volume current line segments from a triangulated BEM head model. As mentioned in Section 2.2.5, although we have shown that an equivalent volume current line segment exists, its construction or shape is non-trivial in general. However, since they are equivalent to boundary surface currents with a surface normal orientation (e.g. spherical head models with origin at its center have surface normal vectors and equivalent volume current segments that are both radial), one may construct line segments with the same orientations as each triangle. The challenge comes in determining the appropriate length (multiplied by current) and spatial placement for all the line segments, since they must necessarily form a continuous line current.

5.1 Boundary Element Method overview

A common forward signal calculation method is the BEM, which triangulates the head model into a decimated surface mesh. This allows for the electric potential V in Geselowitz's

equation (2.33), which is implicitly defined and difficult to determine in the continuous case, to be approximated at the triangle locations [98, 118, 136]. With discrete values of V, the magnetic field and signal can then be approximated.

We now give an overview of BEM used in MEG signal forward calculations. More comprehensive reviews of BEM methods may be found in [30, 40, 118, 133, 136].

5.1.1 Triangularizing the head model

Let us assume all the results and assumptions in Chapter 2. For a piecewise homogeneous conductor head model with N_S conductivity boundary surfaces, recall that the magnetic field due to the total current density $\mathbf{J}(\mathbf{r}')$ is given by Geselowitz's formula (2.31) in Section 2.2.2 [49, 59],

$$\mathbf{B}(\mathbf{r}) = \frac{\mu_0}{4\pi}\int_{v'} \mathbf{J}_{pri}(\mathbf{r}') \times \frac{\mathbf{r}-\mathbf{r}'}{|\mathbf{r}-\mathbf{r}'|^3}\, dv' + \frac{\mu_0}{4\pi}\sum_{l=1}^{N_S}\left(\sigma_l^- - \sigma_l^+\right)\int_{S_l'} V(\mathbf{r}')\frac{\mathbf{r}-\mathbf{r}'}{|\mathbf{r}-\mathbf{r}'|^3}\times d\mathbf{S}_l' \tag{5.1}$$

$$\equiv \mathbf{B}_{pri}(\mathbf{r}) + \mathbf{B}_{vol}(\mathbf{r}), \tag{5.2}$$

where $\mathbf{B}_{pri}$ is the contribution by primary currents, $\mathbf{B}_{vol}$ is the contribution by volume currents, v' is the total head volume, and σ_l^- and σ_l^+ are the conductivities of the inner and outer regions relative to S_l. In order to evaluate $\mathbf{B}$, the electric potential V in $\mathbf{B}_{vol}$ must be found.

The electric potential $V(\mathbf{r})$ for a field point $\mathbf{r}$ on the k^{th} surface S_k is given intrinsically by [59, 118]

$$V(\mathbf{r}) = V_\infty(\mathbf{r}) - \frac{1}{2\pi}\sum_{l=1}^{N_S}\frac{\sigma_l^- - \sigma_l^+}{\sigma_k^- + \sigma_k^+}\int_{S_l'} V(\mathbf{r}')\frac{\mathbf{r}-\mathbf{r}'}{|\mathbf{r}-\mathbf{r}'|^3}\cdot d\mathbf{S}_l', \tag{5.3}$$

where

$$V_\infty(\mathbf{r}) = \frac{1}{2\pi\left(\sigma_k^- + \sigma_k^+\right)}\int_{v'}\mathbf{J}_{pri}(\mathbf{r}')\cdot\frac{\mathbf{r}-\mathbf{r}'}{|\mathbf{r}-\mathbf{r}'|^3}\, dv'. \tag{5.4}$$

Similar to the $\mathbf{B}$ field case, the surface integral term in (5.3) corresponds to the volume current contribution, whereas (5.4) corresponds to the primary current contribution.

The primary current contribution V_∞ is easily obtained if we know $\mathbf{J}_{pri}$. In particular, if

we let $\mathbf{J}_{pri}$ be a collection of N_D current dipoles as described by (2.29), then (5.4) collapses into the simple form

$$V_\infty(\mathbf{r}) = \frac{1}{2\pi\left(\sigma_k^- + \sigma_k^+\right)} \sum_{n=1}^{N_D} \mathbf{D}_n \cdot \frac{\mathbf{r} - \mathbf{r}'_n}{|\mathbf{r} - \mathbf{r}'_n|^3}. \tag{5.5}$$

As for the volume current contribution, we may discretize each surface S_l into N_l triangles; this results in the approximation

$$V(\mathbf{r}) \approx V_\infty(\mathbf{r}) - \frac{1}{2\pi} \sum_{l=1}^{N_S} \frac{\sigma_l^- - \sigma_l^+}{\sigma_k^- + \sigma_k^+} \sum_{m=1}^{N_l} \int_{\Delta_l^m} V(\mathbf{r}') \frac{\mathbf{r} - \mathbf{r}'}{|\mathbf{r} - \mathbf{r}'|^3} \cdot d\mathbf{S}'_{\Delta_l^m}, \tag{5.6}$$

where Δ_l^m is the m^{th} triangle of surface S_l.

If we have chosen a large enough N_l such that the triangle areas are small, then reasonable assumptions about the behavior of V within each triangle can be made. This allows us to define and hence estimate V with basis and weight functions constructed from the parameters of relevant triangles. For example, we may use a constant or linear basis with collocation, Galerkin weighting [133], or other higher-degree basis functions [48].

In this chapter, we choose the simplest and most straightforward BEM methods: the constant collocation (CC) and linear collocation (LC) approaches. Since we will only be using BEM as a tool to illustrate the behavior of signal errors at various sensor distances due to head geometry errors, CC and LC BEM suffice for our purposes. Moreover, the simplicity of CC BEM has the added advantage of being able easily illustrate the general method that one may use to find analytical forms of the firtst-order signal errors. This is shown in Section 5.4.

We present the CC case in the next section, which assumes a constant potential V within each triangle. The LC approach approximates the potential within each triangle as a linear function via an interpolation from the potentials at the three vertices (see [30, 133, 136]).

5.1.2 Linearization of discretized electric potentials

Under the assumption that the potential is constant in each triangle, we can write $V(\mathbf{r}') \approx V(\mathbf{c}_l^m)$ when $\mathbf{r}' \in \Delta_l^m$, where $\mathbf{c}_l^m$ is the centroid of Δ_l^m. This allows us to pull the potential

term out of the integral in (5.6) to get

$$\int_{\Delta_l^m} V(\mathbf{r}') \frac{\mathbf{r}-\mathbf{r}'}{|\mathbf{r}-\mathbf{r}'|^3} \cdot d\mathbf{S}_{\Delta_l^m} \approx V(\mathbf{c}_l^m) \int_{\Delta_l^m} \frac{\mathbf{r}-\mathbf{r}'}{|\mathbf{r}-\mathbf{r}'|^3} \cdot d\mathbf{S}'_{\Delta_l^m}. \tag{5.7}$$

Notice that the integral on the right hand side is now simply the solid angle spanned by the triangle Δ_l^m from the observation point $\mathbf{r}$; let us denote it as $\Omega_l^m(\mathbf{r})$. If we let $\mathbf{r}_{i0} \equiv \mathbf{r}_i - \mathbf{r}$ be the three vertices of the triangle relative to $\mathbf{r}$, $i = 1, 2, 3$, and let r_{i0} be their lengths, we may equivalently express each Ω_l^m as [150]

$$\Omega_l^m = 2 \arctan \left[\frac{\mathbf{r}_{10} \cdot (\mathbf{r}_{20} \times \mathbf{r}_{30})}{r_{10} r_{20} r_{30} + (\mathbf{r}_{10} \cdot \mathbf{r}_{20}) r_{30} + (\mathbf{r}_{30} \cdot \mathbf{r}_{10}) r_{20} + (\mathbf{r}_{20} \cdot \mathbf{r}_{30}) r_{10}} \right]. \tag{5.8}$$

Let $\mathbf{r}$ coincide with centroids of the triangles as well. Then, all the potential terms of (5.3) are discretized at the same locations and it can now be compactly written as

$$V(\mathbf{c}_k^i) = V_\infty(\mathbf{c}_k^i) - \frac{1}{2\pi} \sum_{l=1}^{N_S} \sum_{m=1}^{N_l} \frac{\sigma_l^- - \sigma_l^+}{\sigma_k^- + \sigma_k^+} V(\mathbf{c}_l^m) \Omega_l^m(\mathbf{c}_k^i), \tag{5.9}$$

or equivalently in matrix form,

$$\begin{bmatrix} \mathbf{V}_1 \\ \vdots \\ \mathbf{V}_{N_S} \end{bmatrix} = \begin{bmatrix} \mathbf{V}_{\infty,1} \\ \vdots \\ \mathbf{V}_{\infty,N_S} \end{bmatrix} + \begin{bmatrix} \mathbf{G}_{1,1} & \cdots & \mathbf{G}_{1,N_S} \\ \vdots & \ddots & \vdots \\ \mathbf{G}_{N_S,1} & \cdots & \mathbf{G}_{N_S,N_S} \end{bmatrix} \begin{bmatrix} \mathbf{V}_1 \\ \vdots \\ \mathbf{V}_{N_S} \end{bmatrix} \tag{5.10}$$

where

$$G_{k,l}^{i,m} = -\frac{1}{2\pi} \frac{\sigma_l^- - \sigma_l^+}{\sigma_k^- + \sigma_k^+} \Omega_l^m(\mathbf{c}_k^i). \tag{5.11}$$

A quick inspection reveals that the matrix $\mathbf{G}$ is the only term that depends on the head boundaries' geometries, and it is dependent only on the geometries and conductivities of the conductor as well. This means that for different source configurations within the same head model, $\mathbf{G}$ only needs to be calculated only once, as opposed to $\mathbf{V}_\infty$ that needs to be recalculated.

5.1.3 Matrix deflation

If we write the matrix equation (5.10) as $\mathbf{V} = \mathbf{V}_\infty + \mathbf{G}\mathbf{V}$, then we have

$$(\mathbb{I} - \mathbf{G})\,\mathbf{V} = \mathbf{V}_\infty, \tag{5.12}$$

where $\mathbb{I}$ is the identity matrix. It is seemingly straightforward to solve for $\mathbf{V}$ by taking the inverse of $(\mathbb{I} - \mathbf{G})$; however, $(\mathbb{I} - \mathbf{G})$ is in fact non-invertible since it is rank-deficient. The electric potential $\mathbf{V}$ has an infinite number of solutions since it is defined up to an additive constant. This manifests from the fact that the fundamental equation we are trying to solve is the Poisson equation within the head,

$$\boldsymbol{\nabla} \cdot (\sigma \boldsymbol{\nabla} V) = \boldsymbol{\nabla} \cdot \mathbf{J}_{pri} \tag{5.13}$$

with Neumann boundary condition at each boundary (normal current continuity)

$$\sigma^+ \boldsymbol{\nabla} V \cdot \mathbf{n} = \sigma^- \boldsymbol{\nabla} V \cdot \mathbf{n}, \tag{5.14}$$

where $\mathbf{n}$ is the outward-pointing unit surface normal. These equations are specified only up to the first derivative/gradient of V, hence V is defined up to a constant.

Let k be a nonzero constant, and let $\mathbf{e} = (1, 1, \ldots, 1)^T$. We thus know that both $\mathbf{V}$ and $\mathbf{V} + k\mathbf{e}$ are solutions to the matrix equation. In addition to (5.12), we also have

$$(\mathbb{I} - \mathbf{G})\,(\mathbf{V} + k\mathbf{e}) = \mathbf{V}_\infty. \tag{5.15}$$

Subtracting (5.12) from this yields

$$(\mathbb{I} - \mathbf{G})\,\mathbf{e} = 0 \tag{5.16}$$

which indicates that $(\mathbb{I} - \mathbf{G})$ has a zero eigenvalue with associated eigenvector $\mathbf{e} \neq \mathbf{0}$, i.e. it

is indeed singular. Equivalently,

$$\mathbf{G}\mathbf{e} = \mathbf{e}, \tag{5.17}$$

i.e. $\mathbf{G}$ has a unit eigenvalue with corresponding eigenvector $\mathbf{e}$. Therefore, one way to avoid the singularity of $(\mathbb{I} - \mathbf{G})$ is to eliminate this unit eigenvalue of $\mathbf{G}$. The standard way to do this is by *deflation*, as follows.

First, assume that the unit eigenvalue of $\mathbf{G}$ is has a multiplicity of 1 [140]. For any vector $\mathbf{b}$, we need to find a vector $\mathbf{c}$ with constant entries (not all necessarily the same) such that

$$\mathbf{c}^T\mathbf{b} = \begin{cases} k & \text{if } \mathbf{b} = k\mathbf{e} \\ 0 & \text{otherwise.} \end{cases} \tag{5.18}$$

The first case imposes the condition of defining a reference potential in some way. For example, if we pick $\mathbf{c}$ to have all the same entries, then it means we let the sum of all potentials over all boundaries to be zero [61]. We may also pick just a few entries to be zero, corresponding to a possibly more meaningful reference potential; for example, Wilson terminals are used in electrocardiogram [42].

The second case ensures that all eigenvalues of $\mathbf{G}' \equiv (\mathbf{G} - \mathbf{e}\mathbf{c}^T)$ are equal to those of $\mathbf{G}$, apart from the unit eigenvalue which is replaced by zero. This ensures that $\mathbf{G}'$ is singular, which leads to $(\mathbb{I} - \mathbf{G}')$ being non-singular and hence invertible by condition (5.17). We may explicitly show this preservation of eigenvalues for $\mathbf{G}'$ as follows. Let λ be eigenvalues of $\mathbf{G}$, and $\mathbf{v}_e$ be their corresponding eigenvectors. For $\mathbf{v}_e \neq \mathbf{e}$,

$$\mathbf{G}'\mathbf{v}_e = \left(\mathbf{G} - \mathbf{e}\mathbf{c}^T\right)\mathbf{v}_e = \mathbf{G}\mathbf{v}_e - \mathbf{e}\mathbf{c}^T\mathbf{v}_e = \lambda\mathbf{v}_e - \mathbf{e}0 = \lambda\mathbf{v}_e, \tag{5.19}$$

hence eigenvalues are preserved. For $\mathbf{v}_e = k\mathbf{e}$,

$$\mathbf{G}'k\mathbf{e} = \left(\mathbf{G} - \mathbf{e}\mathbf{c}^T\right)k\mathbf{e} = \mathbf{G}k\mathbf{e} - \mathbf{e}\mathbf{c}^Tk\mathbf{e} = k\mathbf{e} - \mathbf{e}k = 0, \tag{5.20}$$

which tells us that $\mathbf{G}'$ is singular.

Thus, with (5.18) that allows for the construction of the invertible deflated $(\mathbb{I} - \mathbf{G}')$, we can solve for $\mathbf{V}$ via

$$\mathbf{V} = \left(\mathbb{I} - \mathbf{G} + \mathbf{e}\mathbf{c}^T\right)^{-1} \mathbf{V}_\infty. \tag{5.21}$$

5.1.4 Discretization of the magnetic field

With $\mathbf{V}$, we now have a set of discrete electric potential solutions at the triangle centroids. If we discretize $\mathbf{B}_{vol}$ in an identical manner as (5.6), it allows for the approximation of the magnetic field at an arbitrary field point $\mathbf{r}$ as

$$\mathbf{B}\left(\mathbf{r}\right) \approx \mathbf{B}_{pri}\left(\mathbf{r}\right) + \frac{\mu_0}{4\pi} \sum_{l=1}^{N_S} \left(\sigma_l^- - \sigma_l^+\right) \sum_{m=1}^{N_l} V\left(\mathbf{c}_l^m\right) \mathbf{\Omega}_l^m, \tag{5.22}$$

where we have defined the *vector solid angle*

$$\mathbf{\Omega}_l^m \equiv \int_{\Delta_l^m} \frac{\mathbf{r} - \mathbf{r}'}{\left|\mathbf{r} - \mathbf{r}'\right|^3} \times d\mathbf{S}'_{\Delta_l^m}. \tag{5.23}$$

The vector solid angle $\mathbf{\Omega}_l^m$ can be evaluated in a simple manner given by [30]

$$\mathbf{\Omega}_l^m = \sum_{i=1}^{3} \left(\gamma_{i-1} - \gamma_i\right) \mathbf{r}_i, \tag{5.24}$$

where

$$\gamma_i \equiv -\frac{1}{\left|\mathbf{r}_{i+1} - \mathbf{r}_i\right|} \cdot \ln \frac{r_i \left|\mathbf{r}_{i+1} - \mathbf{r}_i\right| + \mathbf{r}_i \cdot \left(\mathbf{r}_{i+1} - \mathbf{r}_i\right)}{r_{i+1} \left|\mathbf{r}_{i+1} - \mathbf{r}_i\right| + \mathbf{r}_{i+1} \cdot \left(\mathbf{r}_{i+1} - \mathbf{r}_i\right)}, \tag{5.25}$$

and $i = 1, 2, 3$ corresponds to the three vertices of the m^{th} triangle of surface S_l. Note that $\mathbf{r}_4 \equiv \mathbf{r}_1$ and $\mathbf{r}_0 \equiv \mathbf{r}_3$. This expression, which was derived via an application of Stoke's theorem, thus allows for the easy calculation of the magnetic field using (5.22), assuming that the indexing of vertices and triangles has been done properly during the process of surface triangulation.

With a way to estimate the magnetic field using (5.22), the flux can finally be computed.

We consider only the simpler case of SQUID pick-up loop flux measurements (as opposed to OPM measurements), since they suffice in our primary goal of illustrating how reduced sensor array distances may affect the signal measured due to BEM head model errors. The results presented in the next section (Section 5.3) are expected to hold for volumetric flux measurements of OPM sensors – the cylindrical sensing volumes may be approximated as thin pick-up loops, as seen in Section 4.1.2.

5.2 Subspace angle as a signal error and spatial complexity measure

From the BEM steps above, it is clear that inaccurate mesh models of the head will lead to perturbed triangle vertices and centroids. This causes inaccurate forward calculations of the electric potential V and magnetic field $\mathbf{B}$, and hence the magnetic flux signal $\boldsymbol{\phi}$.

The head model errors that we will consider are generated via random radial perturbations of the mesh vertices. The resulting perturbed quantities $\mathbf{V}'$, $\mathbf{B}'$ and $\boldsymbol{\phi}'$ may be thus be written with an additive error portion, since the error source is independent of the unperturbed quantities $\mathbf{V}$, $\mathbf{B}$ and $\boldsymbol{\phi}$. This gives us

$$\mathbf{V}' = \mathbf{V} + \delta\mathbf{V} \qquad \mathbf{B}' = \mathbf{B} + \delta\mathbf{B} \qquad \boldsymbol{\phi}' = \boldsymbol{\phi} + \delta\boldsymbol{\phi}, \tag{5.26}$$

where

$$\delta\phi_j = \int_{S_j} \delta\mathbf{B}(\mathbf{r}) \cdot d\mathbf{S}_j \tag{5.27}$$

for the j^{th} sensor of a N-sensor array, $j = 1, \ldots, N$. We re-emphasize that the primary current contribution $\mathbf{B}_{pri}$ does not depend on the head model by Geselowitz's formula, thus all errors come from inaccurate volume contribution. In other words, $\delta\boldsymbol{\phi} = \delta\boldsymbol{\phi}_{vol}$. In Section 5.4, we present an analytical approach to calculate the first-order perturbation contributions of $\delta\mathbf{V}$ and $\delta\mathbf{B}$.

We also note that BEM errors apply only to forward models of the signal vectors. Real recorded signal vectors, by definition, do not have errors due to inaccurate head models. The goal in BEM forward models is to set up a head model that obtains a signal $\boldsymbol{\phi}'$ that is as

close as possible to a recorded/true signal $\boldsymbol{\phi}$. If a BEM head model that perfectly models the real subject is achieved, then $\boldsymbol{\phi}' = \boldsymbol{\phi}$, with $\delta\boldsymbol{\phi} = 0$.

There are many metrics that can quantify the error between a recorded/reference data $\boldsymbol{\phi}$ and modeled/perturbed data $\boldsymbol{\phi}'$. For instance, one may calculate the relative error between the signals (similar to (4.27)), or determine the subspace angle between them (as briefly mentioned in Section 3.2.4). Here, we choose the latter metric to illustrate its versatility in two ways: first by quantifying signal errors as mentioned, and second by determining the spatial complexities of signal portions. Since the subspace angle between two matrices (with the same number of rows) is defined as the angle between their column spaces, it is a compact metric that can be used to quantify the discrepancy between any two physically meaningful subspaces of a vector space.

The subspace angle θ between the signals $\boldsymbol{\phi}$ and $\boldsymbol{\phi}'$ is [58],

$$\text{subspace}(\boldsymbol{\phi}, \boldsymbol{\phi}') = \theta = \arccos\left(\frac{\|\text{Proj}_{\boldsymbol{\phi}}\boldsymbol{\phi}'\|}{\|\boldsymbol{\phi}'\|}\right), \tag{5.28}$$

where $\text{Proj}_{\mathbf{x}}\mathbf{y}$ refers to the projection of the column space of some matrix $\mathbf{y}$ onto the column space of matrix $\mathbf{x}$ ($\mathbf{x}$ and $\mathbf{y}$ have the same number of rows necessarily). This has a range of $\theta \in [0, \pi/2]$, with $\theta = 0$ indicating perfect signal agreement (up to a sign), and $\theta = \pi/2$ indicating no correlation between the two signals at all.

To determine the spatial complexity of a signal, we may also calculate the subspace angle $\theta_{1:L}$ between the signal $\boldsymbol{\phi}$ (or $\boldsymbol{\phi}'$) and the L-degree truncated SSS basis matrix $\mathbf{S}_{1:L}$ (4.13),

$$\theta_{1:L} = \arccos\left(\frac{\|\text{Proj}_{\mathbf{S}_{1:L}}\boldsymbol{\phi}\|}{\|\boldsymbol{\phi}\|}\right). \tag{5.29}$$

A high $\theta_{1:L}$ indicates that the space spanned by the basis vectors of degree up to L does not adequately explain $\boldsymbol{\phi}$. This indicates that in addition to any low-frequency components, $\boldsymbol{\phi}$ also contains high frequency components that point in directions independent of the column space of $\mathbf{S}_{1:L}$, which correspond to $l > L$ basis modes. As such, more spatially complex

signals require a higher L degree truncation of the SSS basis matrix to obtain a low $\theta_{1:L}$. This is consistent with the discussions in Section 4.1 that state that higher L truncations are required to obtain higher signal resolutions.

Although we do not observe this in our results in the next section (Section 5.3), we note that signal aliasing may affect the value of $\theta_{l:L}$ in unpredictable ways. As discussed in Section 4.1 as well, if there exist $l > L$ signal components, they are forced to be projected onto the limited low spatial frequency basis vectors of $\mathbf{S}_{in}$, which may result in spurious projections into certain basis components [132].

5.3 BEM simulation results

Here, we present our results for the effects of BEM head model inaccuracies on the signal for varying sensor array and source distances. ECD fits were then performed with the inaccurate forward calculated signals to determine their effects on source localization in both noiseless and noisy sensor cases.

5.3.1 Simulation setup

For our reference setup, we used a simple 1-shell spherical head model of radius 9 cm and conductivity 0.33 S/m with origin located at the center of the sphere. This simple model was chosen over a more anatomically accurate multiple-shell model, since it allowed for arbitrary perturbations to its vertices without restrictions. For multiple-shell models, vertex perturbations are restricted by the distances between the shells, since the (perturbed) shells must not intersect.

The 1-shell spherical head model was triangulated into 1280 triangles (642 vertices), and a CC BEM forward calculation was performed as described in Sections 5.1 and 5.2 to obtain $\boldsymbol{\phi}$. A 9-point cubature approximation was used to calculate the signal, since it has been shown in Section 4.7.2 to be accurate for the sensor distances that we will be considering (10 cm to 15 cm). The current sources considered were 4 electric dipoles with varying depths located at $(2, 0, 0)$ cm, $(4, 0, 0)$ cm, $(6, 0, 0)$ cm, and $(8, 0, 0)$ cm, each having a moment of $(0, 10, 0)$ nAm. The BEM method was implemented using the Matlab library developed in [136].

Then, to simulate inaccurate mesh modeling, the vertices of the spherical mesh were randomly perturbed radially up to 2%, 4%, 6%, 8% and 10% relative to the 9 cm radius, and the signal $\boldsymbol{\phi}'$ was calculated for each case. Since the vertex perturbations were random, we generated 100 meshes for each vertex perturbation amount to ensure that any observations made are not simply a result of random effects. The results presented in the following sections for each vertex perturbation amount are the averaged quantities over the 100 signals obtained.

The sensor array that we used consisted of 324 square magnetometer pick-up loops, each with side length 2.1 cm. The sensors were also made to have non-radial orientations (to avoid linear dependence of the SSS basis [142]), and are uniformly arranged on a spherical shell up to $\pi/6$ below the $z = 0$ plane. Figure 5.1 illustrates the sensor, head, and source setup.

5.3.2 Total signal error at varying sensor array distances

First, we investigate how the error due to BEM mesh inaccuracy varies according to sensor array distance using equation (5.28). The sensor array radius was varied from 10 cm to 15 cm, in increments of 1 cm (i.e. 1 cm to 6 cm from the surface of a 9 cm head model) and the signal was assumed the be noiseless.

Figure 5.2 shows that for all the source distances considered, the subspace angle between the reference signal $\boldsymbol{\phi}$ and perturbed signal $\boldsymbol{\phi}'$ decreases as sensor array distance increases. This indicates decreasing relative effects of mesh boundary inaccuracies for further sensor arrays. Moreover, for a given sensor array distance, smaller perturbations to the spherical head model resulted in smaller subspace angles as expected.

These results may also be seen via direct plots of $\boldsymbol{\phi}$ and $\boldsymbol{\phi}'$ as shown Figure 5.3. The first row of plots illustrates the former result; it shows the signals measured for varying sensor array distances with the 2 cm source and one of the 10% vertex perturbation meshes. The latter result is illustrated in the second row of plots, which shows the signals measured for varying mesh perturbation amounts with the 2 cm source and 10 cm sensor array.

An interesting observation can be made from the plots of Figure 5.2: we see that the subspace angles in the plots for the 2 cm and 8 cm sources are higher than that of the 4 cm

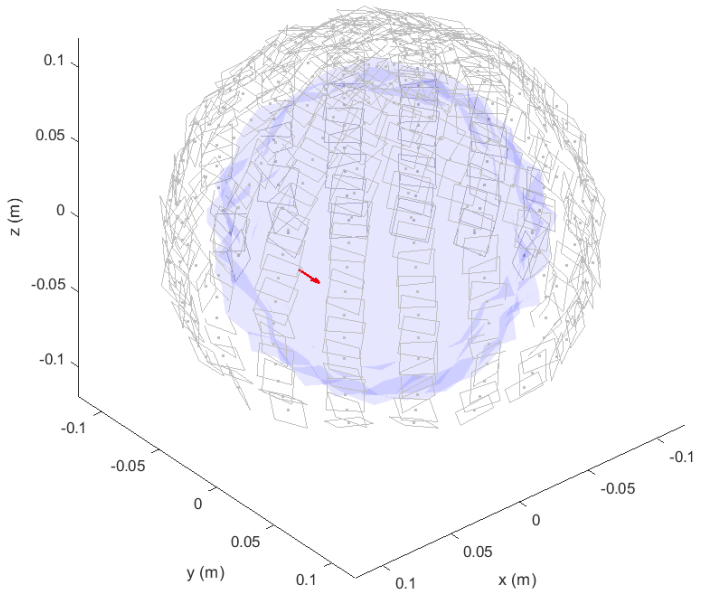

Figure 5.1: The BEM setup: the blue mesh shows a triangulated sphere of radius 9 cm that has its vertices randomly perturbed by up to 10%, and the red arrow shows a dipolar source located at $(6, 0, 0)$ cm. A spherical sensor array of radius 10 cm with 324 randomly-oriented square pick-up loops is also shown.

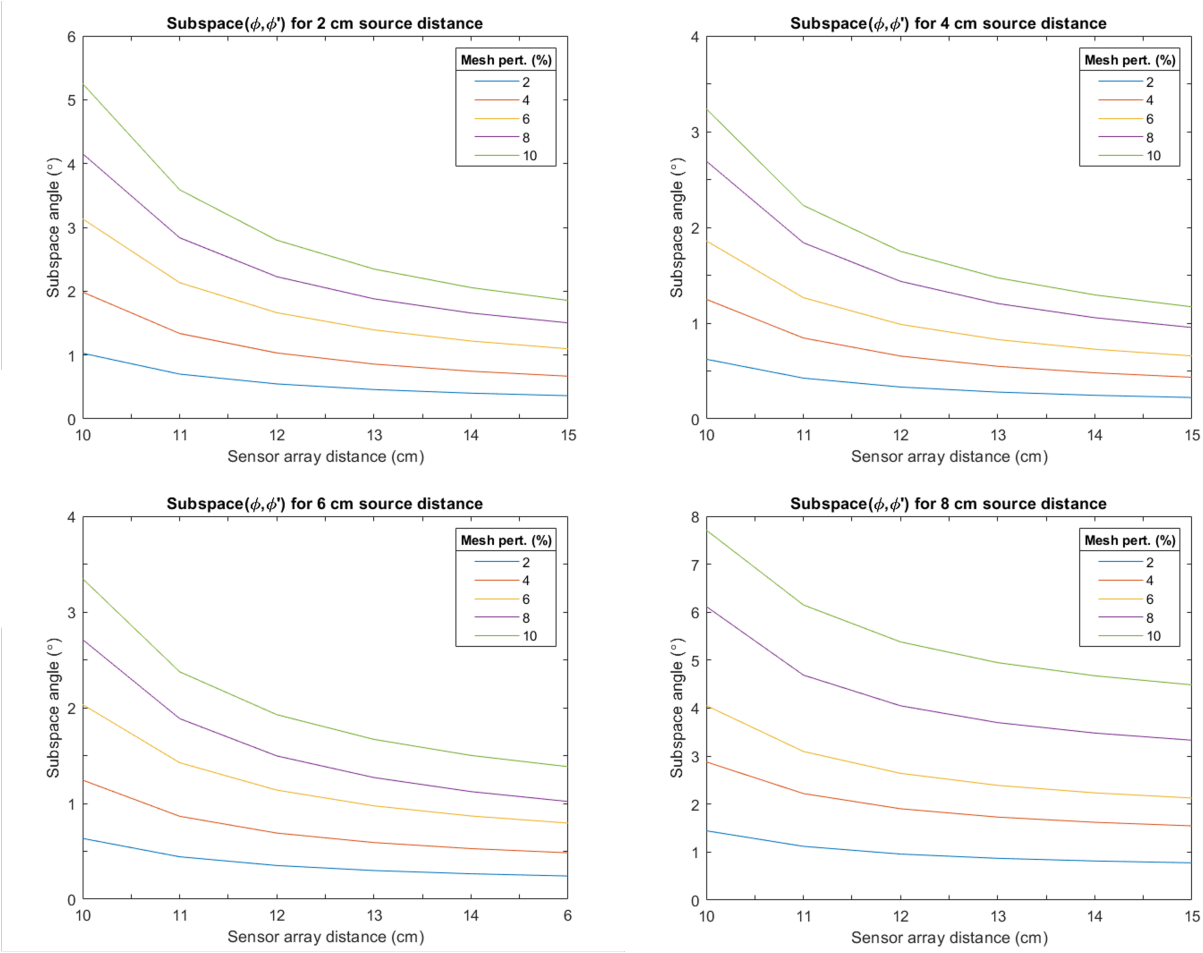

Figure 5.2: In the noiseless case, the subspace angle between $\boldsymbol{\phi}$ and $\boldsymbol{\phi}'$ decreases as sensor array distances increase. Signals measured by distant sensor arrays are thus less impacted by head model inaccuracies. Also, as mesh perturbations increase, the subspace angle increases as expected.

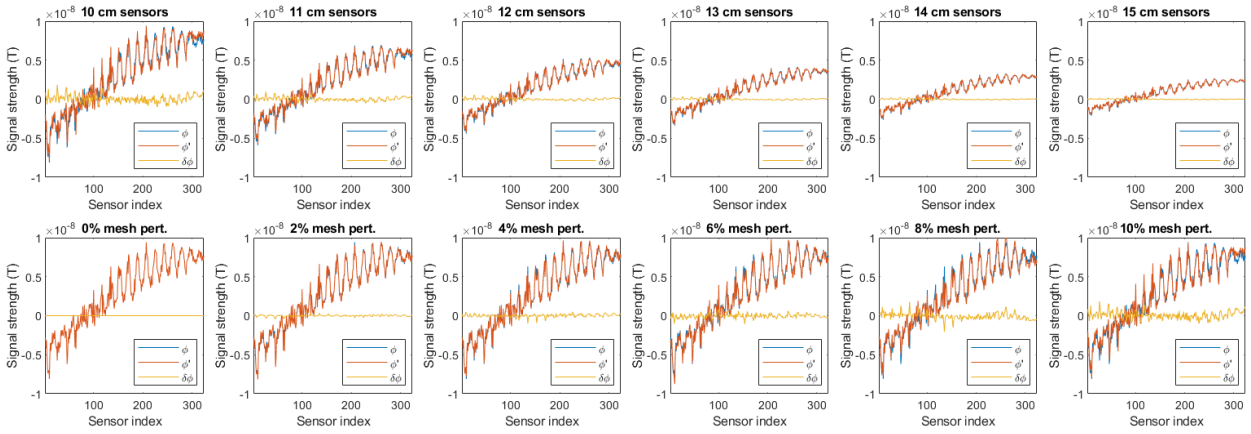

Figure 5.3: Plots of $\boldsymbol{\phi}$, $\boldsymbol{\phi}'$, and $\delta\boldsymbol{\phi} = \boldsymbol{\phi}' - \boldsymbol{\phi}$ for the following setups: (first row) the 2 cm source, a 10% mesh perturbation, and varying sensor array distances from 10 cm to 15 cm, and (second row) the 2 cm source, the 10 cm sensor array, and varying mesh perturbations from 0% to 10%. As sensor array distance increases, signal error decreases for the same amount of mesh perturbation. As mesh perturbations increase, signal errors increase.

and 6 cm sources. This indicates a "turnaround" point of the subspace angle as a function of source distance. A further investigation reveals that this behavior may be explained by an increased relative volume current contribution for deeper and superficial sources.

We found that for all mesh perturbation amounts, 4 cm and 6 cm sources have lower volume-to-primary current contribution ratios as compared to the 2 cm and 8 cm sources. This may be explained qualitatively by the fact that the deep 2 cm primary source has a low primary current signal strength due to the larger source-to-sensor distance, and hence has a higher volume-to-primary current contribution. The superficial 8 cm source has a small source-to-sensor distance, and hence measures a larger volume current contribution, resulting in the higher volume-to-primary current contribution to the signal. As mentioned previously, all signal errors result from errors in the volume contribution portion only, i.e. $\delta\phi = \delta\boldsymbol{\phi}_{vol}$, thus higher volume-to-primary current contributions implies higher signal errors given a same mesh perturbation/volume current perturbation amount.

Figure 5.4 shows the volume-to-primary current contributions to the signal measured with the 10 cm sensor array for a 10% mesh perturbation. The 2 cm and 8 cm sources have a

higher volume-to-primary current contribution than the 4 cm and 6 cm sources.

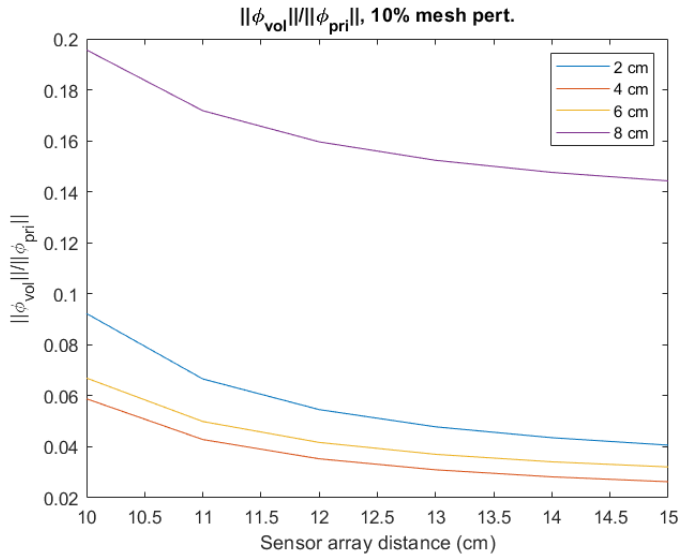

Figure 5.4: A plot of the volume-to-primary current contributions towards the total signal measured with the 10 cm sensor array for a 10% mesh perturbation. The values are higher for the 2 cm and 8 cm sources than the 4 cm and 6 cm sources, resulting in higher total signal errors as shown in Figure 5.2.

5.3.3 The signal error portion and its spatial complexity

Next, we determine if the additive error of the signal $\delta\boldsymbol{\phi}$ is more spatially complex than the unperturbed reference signal, and verify that it indeed $\delta\boldsymbol{\phi}$ increases as sensor distances decrease.

First, we show that the unperturbed signal may be explained to a large extent with a $L = 12$ degree truncated SSS basis matrix for the 10 cm to 15 cm sensor array distances considered. This is shown in the first row of plots in Figure 5.5. The subspace angle $\theta_{1:L}$ decays to become nearly zero at $L = 12$ for all source distances. As expected, closer sensor array distances have higher subspace angles than further sensor arrays, which agrees with Figure 5.2.

The second row of plots in Figure 5.5 show that despite the total signal $\boldsymbol{\phi}$ being well-

explained at $L = 12$, the signal errors $\delta\boldsymbol{\phi}$ for all source distances require a higher L truncation to explain, indicating that have a more spatially complex pattern with higher spatial frequency components. This is confirmed by the decaying behavior of the plots as L increases (as opposed to, for instance, an erratic plot, which means that $\boldsymbol{\phi}$ cannot be resolved with the spatial frequency basis modes), but this is to be expected since $\delta\phi = \delta\phi_{vol}$ is a volume current contribution. The subspace angles, which are also much higher than those of the total signal $\boldsymbol{\phi}$ in the first row, thus also indicate that higher spatial frequency components are affected more by inaccurate head models. For increased sensor distances, the subspace angles are smaller for all source distances, which explicitly verifies the results of Figure 5.2

Note that the $\delta\boldsymbol{\phi}$ in Figure 5.5 was obtained using a 10% mesh perturbation case. Although not shown here, the plots for all the other mesh perturbation cases are similar.

5.3.4 Source localization and orientation errors

From our results in Section 5.3.2 above, we see that with an inaccurate BEM head model, (noiseless) signals measured by closer sensor arrays suffer from higher inaccuracies since the higher spatial frequency components have larger errors. Deep and superficial sources also had higher signal errors due to a higher relative volume current contribution. Here, we investigate if these observations will be seen in the form of source localization errors as well. The source localization procedure was done via a standard ECD fit using the "fit_dipole" function in MNE-Python 1.0 [53, 54].

Note that in this section, the forward model was computed using LC BEM instead of CC BEM, since it is currently the only solving method implemented in MNE-Python. However, as we will see, since these LC BEM source space observations agree with the CC BEM signal space observations in the previous section, it is a strong indication that the results we see are due to reasons independent of BEM methods as desired (i.e. the head model inaccuracies).

The ECD fit errors when performed on the noiseless signals of the 2 cm, 4 cm, 6 cm and 8 cm source distances are shown in the first columns of Figures 5.6, 5.7, 5.8 and 5.9 respectively. Indeed, for a fixed mesh perturbation, source localization and orientation errors

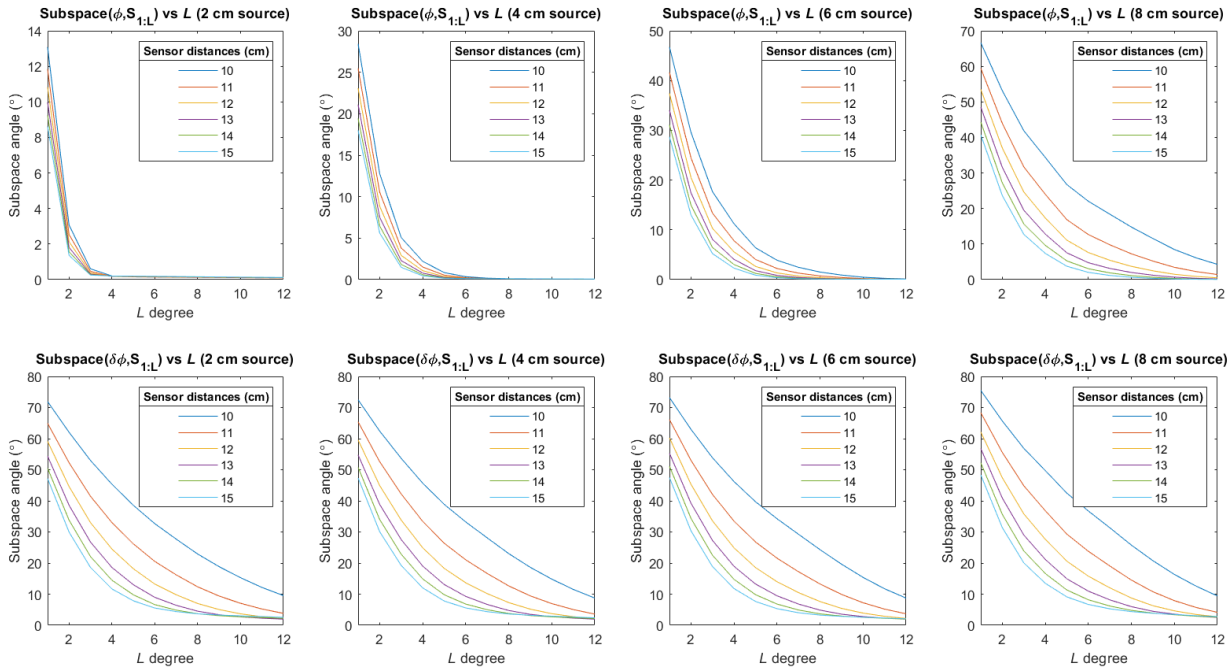

Figure 5.5: (Top row) The total signal $\boldsymbol{\phi}$ can be explained well with a $L = 12$ degree truncation of $\mathbf{S}_{1:L}$ for all source distances. (Bottom row) The signal error portion $\delta\boldsymbol{\phi}$ due to a 10% mesh perturbation are higher and requires a higher L degree truncation to explain than $\boldsymbol{\phi}$. This means $\delta\boldsymbol{\phi}$ have higher higher spatial complexities than $\boldsymbol{\phi}$, and the higher spatial frequency components of signals are more sensitive to head model inaccuracies. Closer sensor distances also have higher subspace angles, corresponding to increased signal errors in agreement with Figure 5.2.

are largest for closer sensor arrays. The 2 cm and 8 cm sources had higher errors than the 4 cm and 6 cm sources as well. These observations are in agreement with the signal error results in Section 5.3.2.

However, noiseless signals are impractical in real life; the primary motivation to move sensors closer to the head is to potentially utilize the higher SNR for improved source localization results. For the j^{th} sensor of an N-sensor array, the definition of SNR (with units of decibels) used in MNE-Python 1.0 follows that of Goldenholz [51],

$$\text{SNR} = 10 \log \left[\frac{q^2}{N} \sum_{j=1}^{N} \frac{\phi_j^2}{s_j^2} \right], \tag{5.30}$$

where q denotes the source strength and s_j^2 denots the noise variance on sensor j.

For each mesh perturbation and for a reduced sensor array distance, we introduced various noise levels to determine the noise level at which the effect of having more accurate source localizations due to the higher SNR outweighs the effect of less accurate source localizations due to the increased noiseless signal error.

We found that this occurred at SNR $\approx$ 6 dB (the sensor noise was varied to force a 6 dB SNR for varying sensor array distances); for SNR greater than 6 dB, the localization and orientation errors began to increase as sensor array distances increased. This is shown in the second column of Figures 5.6, 5.7, 5.8 and 5.9, where the position and orientation errors for a 10 cm and 15 cm sensor array distance was seen to be approximately equal for most mesh perturbation amounts, only very slightly increasing for more distant sensor array distances.

The third and rightmost column of Figures 5.6, 5.7, 5.8 and 5.9 show that for a constant 20 fT noise level which is greater than an SNR of 6 dB, there is an improvement in source localization for closer sensor arrays. This means that the effects of having a higher SNR that allow for improved source localization resolutions have outweighed the effects of BEM head model errors errors that cause more inaccurate source localizations.

Our results tell us that in general, OPM sensors should still result in more accurate source localization results despite head modelling errors, since the current signal measurements

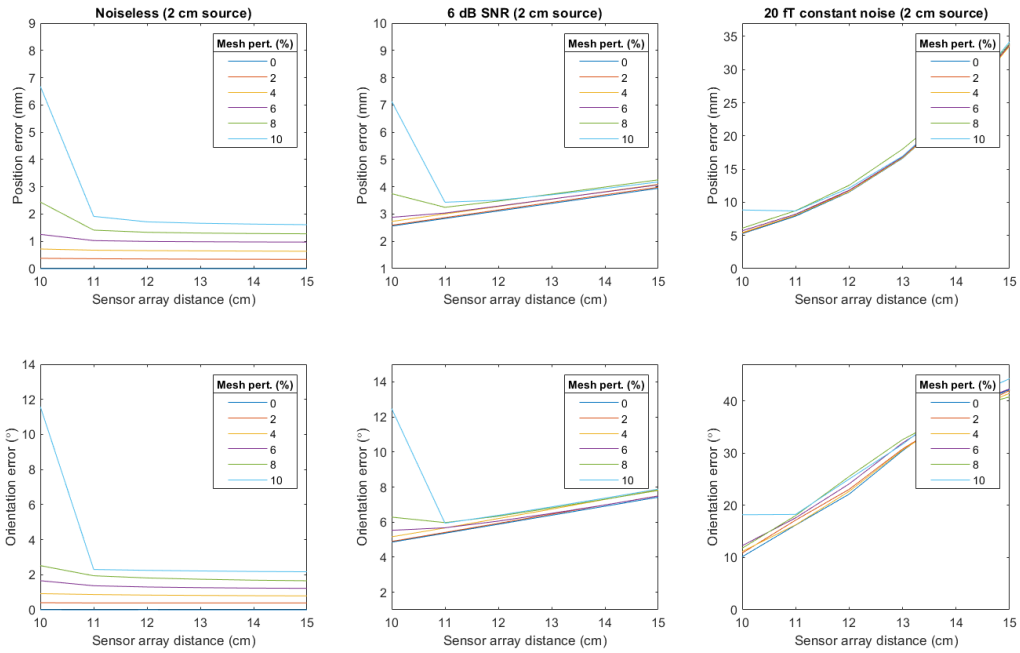

Figure 5.6: ECD fit results for a 2 cm source case. (Left column) The position and orientation errors of the ECD fit for the noiseless signal case. Closer sensor arrays have increased errors, agreeing with the behavior of the noiseless signal error itself. (Middle column) For a noise level of SNR $\approx$ 6 dB, ECD fit errors start to increase slightly for increased sensor array distances, indicating that the improved localization made possible with higher SNR is starting to outweigh the the poorer localization due to more inaccurate noiseless signals. (Right column) For a 20 fT constant noise level (above 6 dB), ECD fit errors decrease for decreased sensor array distances. The effect of higher SNR has now fully outweighed the effects of the increased noiseless signal error.

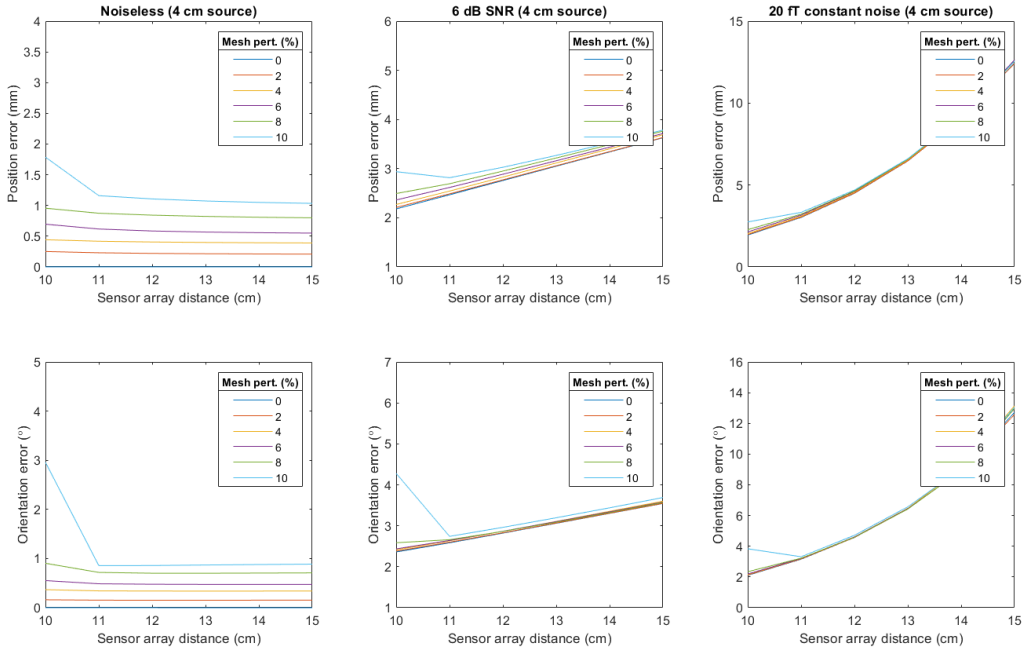

Figure 5.7: ECD fit results for a 4 cm source case. The description of this figure is similar to Figure 5.6.

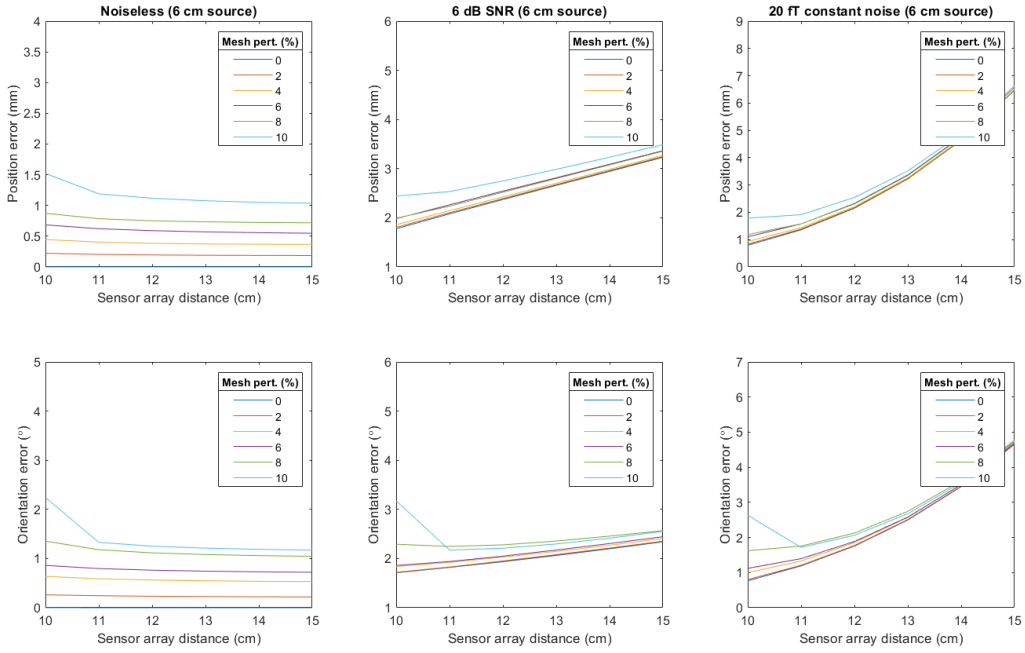

Figure 5.8: ECD fit results for a 6 cm source case. The description of this figure is similar to Figure 5.6.

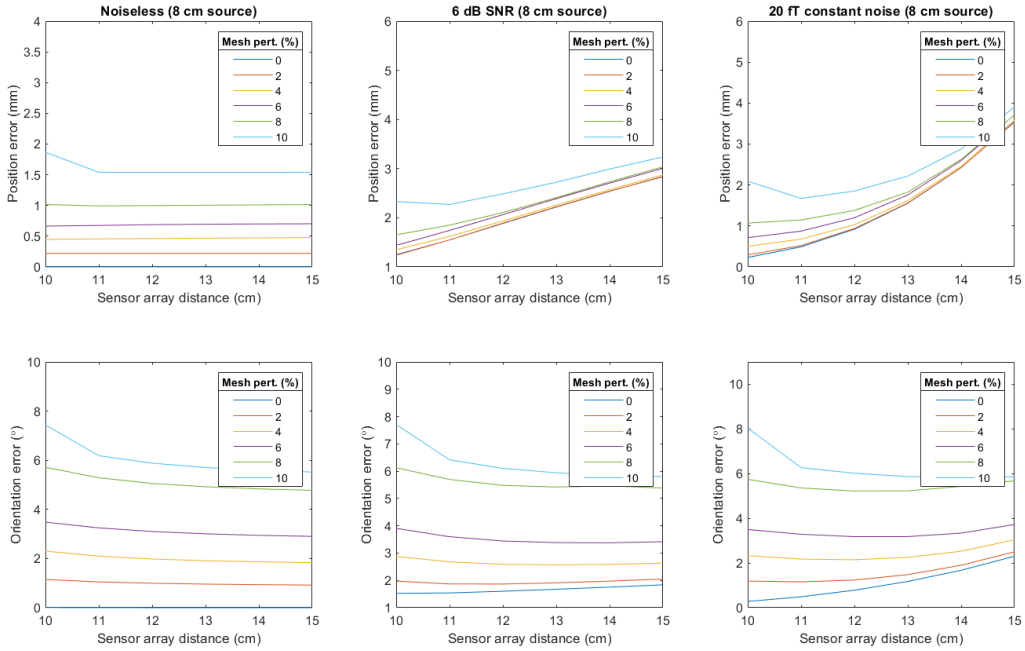

Figure 5.9: ECD fit results for a 8 cm source case. The description of this figure is similar to Figure 5.6.

typically have SNR < 6 dB. However, with the constant improvement of instrumentation and signal processing methods, noise may eventually become suppressed to levels that allow for the effects of the inaccurate noiseless signal to show. As such, it would be beneficial to continue the current efforts in developing methods that minimize BEM head geometry errors.

5.4 Analytical first-order errors for CC BEM: an aside

Here, as an aside, we show an outline for analytical calculations of the signal error due to small boundary perturbations in the CC approach.

From (5.22), we see that there are three terms dependent on the head model that affect the calculation of the magnetic field: the conductivities $\sigma_l^{\pm}$, the scalar electric potential $V(\mathbf{c}_l^m)$ (equivalently, the matrix $\mathbf{G}$), and the vector solid angle $\mathbf{\Omega}_l^m$. The latter two depend on the mesh accuracy, whereas the former depends on the conductivity values.

5.4.1 Perturbations to mesh vertices

First, we consider perturbations to V. By looking at the form of $\mathbf{G}$ (5.11), we see that there are two possible sources of error in the head model: the solid angle (i.e. vertex/triangle centroid perturbations), and the conductivity values of each region. Here, we offer analytical forms to compute the first-order errors due to each of these sources of error. Higher order corrections may be obtained with the help of e.g. Matlab or Mathematica.

The solid angle can be regarded as a scalar field in 12-dimensional space (3 coordinates per $\mathbf{r}$, $\mathbf{r}_1$, $\mathbf{r}_2$, $\mathbf{r}_3$). Perturbations to one of these 12 coordinates corresponds to perturbations in the x, y or z direction of one of the three vertices of the triangle ($\mathbf{r}_1$, $\mathbf{r}_2$, $\mathbf{r}_3$), or to the point of reference $\mathbf{r}$.

Let $\mathbf{r} = (x, y, z)$ and $\mathbf{r}_i = (x_i, y_i, z_i)$, where $i = 1, 2, 3$. For small perturbations, only the first-order expansion term is significant. If we let x be perturbed to become $x + \delta x$, $\delta\Omega$ (5.8) can be approximated as

$$\delta\Omega = \Omega\left(x + \delta x, y, z, x_1, \ldots, z_3\right) - \Omega\left(x, \ldots, z_3\right) \approx \left.\frac{\partial \Omega}{\partial x}\right|_{\mathbf{r},\mathbf{r}_1,\mathbf{r}_2,\mathbf{r}_3} \delta x. \tag{5.31}$$

Let the argument within the arctan of Ω be $P = P(x, \ldots, z_3)$. The right hand side of (5.31) can be evaluated by the chain rule,

$$\frac{\partial \Omega}{\partial x} = \frac{\partial \Omega}{\partial P}\frac{\partial P}{\partial x} = \frac{2}{1+P^2}\frac{\partial P}{\partial x}. \tag{5.32}$$

Due to the symmetric form of the solid angle Ω where the numerator obeys scalar triple product identity and the denominator has terms that all obey cyclic index permutations, we only need to evaluate 2 partial derivatives of P to obtain all 12 of them as follows.

First, evaluate one partial derivative with respect to any of the 3 coordinates of $\mathbf{r}$, and another with respect to any of the 9 coordinates of $\mathbf{r}_i$. Cyclic permutation of the coordinate indices $(x, y, z) \leftrightarrow (z, x, y) \leftrightarrow (y, z, x)$ gives us the other 4 partial derivatives with respect to the other 2 coordinates of $\mathbf{r}$ and $\mathbf{r}_i$. Permutation of vertex indices $(1, 2, 3) \leftrightarrow (2, 3, 1) \leftrightarrow (3, 1, 2)$ gives us the other 6 partial derivatives with respect to the coordinates of the other 2 triangle vertices. Note that if we extend to higher-order partial derivatives to obtain the second-order errors and beyond, symmetry considerations may still be utilized to reduce the total number of partial derivatives to evaluate. However, mixed partials mean that more than 2 partial derivatives need to be evaluated necessarily.

One may also interpret the 12 partial derivatives as a 1-1 correspondence between the index permutations and 12 coordinates. The 3 $\mathbf{r}$ coordinates correspond to the 3 cyclic permutations on the coordinate indices (x, y, z), whereas the 9 $\mathbf{r}_i$ coordinates correspond to the $3 \times 3 = 9$ possible pairings of the cyclic permutations the coordinate indices (x, y, z) and vertex indices $(1, 2, 3)$. If we denote the 3 coordinates of $\mathbf{r}$ as (x_1, x_2, x_3) and the 9 coordinates of $\mathbf{r}_i$ as x_j, $j = 4, \ldots, 12$, then the total perturbation of the solid angle is

$$\delta\Omega_l^m\left(\mathbf{c}_k^i\right) \approx \frac{2}{1+P^2}\left(\sum_{j=1}^{3}\left.\frac{\partial P}{\partial x_1}\right|_{\{\sigma_j^c\}}\delta x_j + \sum_{j=4}^{12}\left.\frac{\partial P}{\partial x_4}\right|_{\{\sigma_j^{c+v}\}}\delta x_j\right), \tag{5.33}$$

where $\sigma_j^c = (x_j, x_k, x_l)$ are the 3 possible coordinate index cyclic permutations, and σ_j^{c+v} are the 9 possible pairs of coordinate index and vertex index cyclic permutations. Any

small perturbation of a vertex results in perturbed centroids of its adjacent triangles (i.e. perturbed observation points $\mathbf{r}$), and a perturbation of their solid angles as well; these two cases correspond to the first and second sums in (5.33) respectively. Note that by construction of $\mathbf{G}$ (5.11), the first case (perturbed centroids) contributes nonzero row entries to the additive perturbative matrix $\delta\mathbf{G}$, whereas the second case (perturbed vertices) contributes nonzero column column entries.

We now want to see how this affects $\mathbf{V}$. Let $\mathbf{A} \equiv (\mathbb{I} - \mathbf{G} + \mathbf{e}\mathbf{c}^T)$ and $\tilde{\mathbf{A}} \equiv \mathbf{A} + \delta\mathbf{G}$. If $\tilde{\mathbf{A}}$ is non-singular, then [138]

$$\tilde{\mathbf{A}}\tilde{\mathbf{A}}^{-1} = (\mathbf{A} + \delta\mathbf{G})\,\tilde{\mathbf{A}}^{-1} = I \tag{5.34}$$

$$\implies \mathbf{A}^{-1} = \left(I + \mathbf{A}^{-1}\delta\mathbf{G}\right)\tilde{\mathbf{A}}^{-1} \tag{5.35}$$

$$\implies \tilde{\mathbf{A}}^{-1} - \mathbf{A}^{-1} = -\mathbf{A}^{-1}\delta\mathbf{G}\,(\mathbf{A} + \delta\mathbf{G})^{-1}\,. \tag{5.36}$$

Therefore, errors in potential are given by

$$\delta\mathbf{V} = -\mathbf{A}^{-1}\delta\mathbf{G}\,(\mathbf{A} + \delta\mathbf{G})^{-1}\,\mathbf{V}_\infty. \tag{5.37}$$

Next, we consider the first-order perturbation to the vector solid angle (5.24). It depends only on the coordinates of the triangles' vertices, and may thus be obtained in a straightforward manner,

$$\delta\mathbf{\Omega}_l^m \approx \sum_{i=1}^{3}\left[\sum_{j=1}^{9}\frac{\partial\left(\gamma_{i-1} - \gamma_i\right)}{\partial x_j}\delta x_j\right]\mathbf{r}_i. \tag{5.38}$$

5.4.2 Perturbations to conductivity

We now consider perturbations to $\sigma^{\pm}$, which are conductivity values within the layers of the head model. This is an easier case to deal with, since we may simply add a perturbative

constant $\delta\sigma$ to each σ. For the conductivity term within $\mathbf{G}$, we have

$$\begin{aligned}\delta\sigma_{k,l} &= \frac{\sigma_l^- + \delta\sigma_l^- - \sigma_l^+ - \delta\sigma_l^+}{\sigma_k^- + \delta\sigma_k^- + \sigma_k^+ + \delta\sigma_k^+} - \frac{\sigma_l^- - \sigma_l^+}{\sigma_k^- + \sigma_k^+} \\ &= -\frac{\left(\sigma_l^- - \sigma_l^+\right)\left(\delta\sigma_k^- + \delta\sigma_k^+\right) + \left(\sigma_k^- + \sigma_k^+\right)\left(\delta\sigma_l^+ - \delta\sigma_l^-\right)}{\left(\sigma_k^- + \sigma_k^+\right)^2 + \left(\sigma_k^- + \sigma_k^+\right)\left(\delta\sigma_k^- + \delta\sigma_k^+\right)}.\end{aligned} \tag{5.39}$$

Equations (5.33) and (5.39) together define the total perturbative matrix $\delta\mathbf{G}$ for small vertex perturbations and arbitrary conductivity inaccuracies,

$$\delta G_{k,l}^{i,m} = -\frac{1}{2\pi}\left[\delta\sigma_{k,l}\Omega_l^m\left(\mathbf{c}_k^i\right) + \sigma_{k,l}\delta\Omega_l^m\left(\mathbf{c}_k^i\right)\right]. \tag{5.40}$$

The first-order error of the total magnetic field due to small perturbations in vertex coordinates and head model conductivities is thus

$$\delta\mathbf{B}\left(\mathbf{r}\right) \approx \frac{\mu_0}{4\pi}\left\{\sum_{l=1}^{N_S}\left(\sigma_l^- - \sigma_l^+\right)\sum_{m=1}^{N_l}\left[\delta V\left(\mathbf{c}_l^m\right)\boldsymbol{\Omega}_l^m + V\left(\mathbf{c}_l^m\right)\delta\boldsymbol{\Omega}_l^m\right] \right. \tag{5.41}$$

$$\left. + \sum_{l=1}^{N_S}\left(\delta\sigma_l^- - \delta\sigma_l^+\right)\sum_{m=1}^{N_l} V\left(\mathbf{c}_l^m\right)\boldsymbol{\Omega}_l^m\right\}, \tag{5.42}$$

with its terms given by (5.33), (5.37), (5.38), (5.39), and (5.40).

Chapter 6

NEAR-OPTIMAL SENSOR SELECTION

MEG sensor array design has predominantly been driven by the application of Nyquist sampling theory, which dictates that higher spatial frequencies can be resolved by decreasing the distance between sensors. This is observed in the signal-level case in Chapter 4 as well; more accurate flux evaluations are obtained with a higher number of cubature sampling points. There is thus a general consensus that an increase in the total number of sensors can improve signal resolution [15, 147]. Moreover, higher array densities also prevent signal aliasing [86, 132], improves source localization accuracy in the beamforming framework [155], and has the ability to extract more information from the signal in general (under a Shannon information theory framework) [88, 111], thus it appears to be especially relevant for the next-generation OPM sensor arrays that can be measure higher resolution signals with its closer sensor distances.

However, having denser sensor arrays also presents a few issues. For one, there may be insufficient space on the subject's head to physically accommodate a large number of sensors. For example, infant MEG using OPM sensors will require a denser sensor array due to the decreased sensor distances measuring higher resolution signals (see Section 4.1); their smaller heads may not be able to fit the required amount of sensors. It may additionally be uncomfortable for a subject to wear a dense sensor array, especially if it becomes increasingly heavy [70], or if it takes a long time to set up. The manufacturing costs of a large quantity of sensors may also be high, and can result in compromised testing procedures during development phases where constructing expensive and dense sensor arrays are impractical.

In this chapter, we demonstrate that for focal neural activity that exhibit low-dimensional signal patterns in some basis choice, it is possible to identify a few optimal sensor locations

that can reasonably reconstruct full-state MEG signals for accurate source localization. This is a deviation from the Nyquist sampling consideration above, and alleviates the aforementioned issues that can arise with having dense sensor arrays. To date, there have been some discussions into using a limited number of sensors [110, 123], but only few methods exist to evaluate which sensors are most capable of accurately reconstructing measured signals or localizing sources [10, 73, 103]. Full-state reconstructions with limited sensors has the additional capability of interpolating/extrapolating to regions inaccessible for measurements, for example, areas obstructed by electronic components.

We will first formally state the problem statement, then review the singular value decomposition (SVD), signal reconstruction, and QR pivoting algorithm, which allow for the selection of optimal sensor locations. Then, simple examples of reconstructions of phantom data using selected MEG sensors are performed as proof of concept that sparse sensor arrays may be used in MEG. All the data that we used in this chapter are available on the Brainstorm website (http://neuroimage.usc.edu/brainstorm).

In Figure 6.1, a summary of the procedure utilizing QR pivoting for sensor selection and source reconstruction (blue arrows) is shown alongside the traditional approach (green arrows). QR pivoting, which will be further discussed in Section 6.4, has been widely used in applications including fluid flows, sea surface temperature monitoring, and face image recognition [22, 57, 83, 100]. It is computationally efficient and is one of the most common paradigms for monitoring engineering and physical systems.

We note here that a natural application to sensor selection is sensor array designs. In MEG, sensor layouts are primarily guided by physical/hardware considerations [70], or simply made to sample the head uniformly in some way [110, 123]. For instance, a hexagonal sampling lattice has be shown to be the optimally sparse sampling grid under the above mentioned Nyquist sampling consideration [86]. With informed sensor selection techniques, optimal sensor placement locations can be determined from a dense sensor array, so that sensors can be placed in a principled manner at certain regions of the head based on the neural activity itself. This may be more effective than utilizing a universal, uniformly-spaced

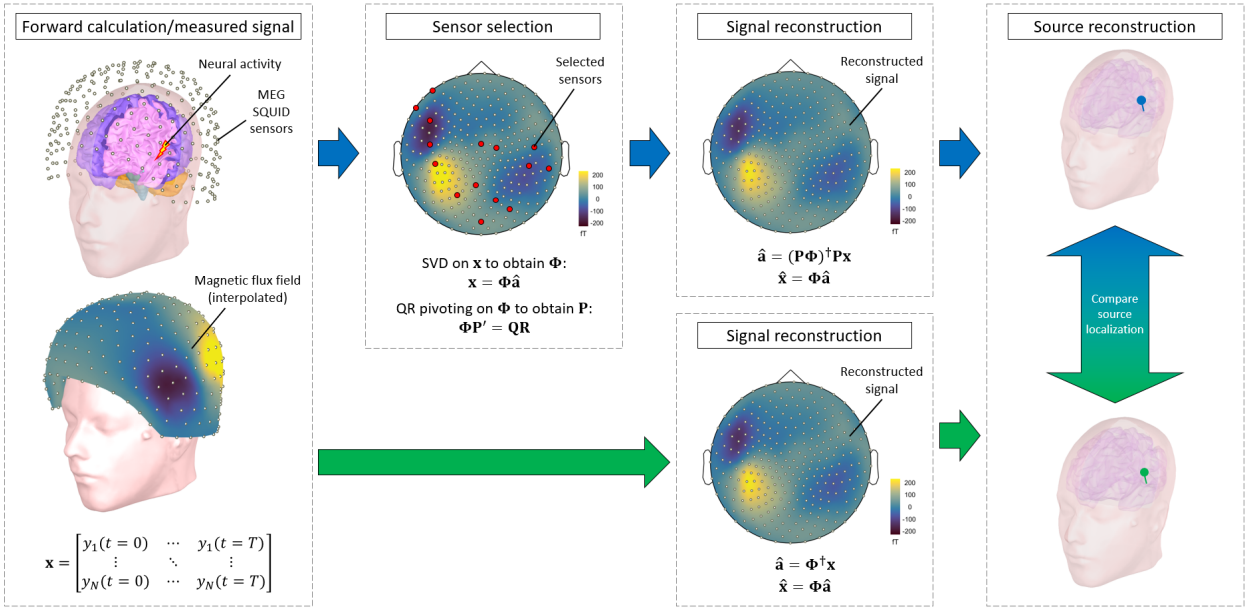

Figure 6.1: (Green arrows) Usual pipeline for signal reconstruction and source localization that utilizes the entire sensor array. (Blue arrows) Proposed pipeline for full-state signal reconstruction and source localization with sparse sampling. Principled sensor selection can be done using QR pivoting on a low-dimensional SVD basis representation of a prior/simulated dataset. $\mathbf{x}$ denotes the full-state signal measurement, $\mathbf{\Phi}$ denotes the rank-r truncated left singular SVD basis of $\mathbf{x}$, $\hat{\mathbf{a}}$ denotes corresponding the (noisy) coefficients of $\mathbf{\Phi}$, and $\mathbf{P}$ (obtained from $\mathbf{P}'$) denotes the permutation matrix that selects rows of $\mathbf{\Phi}$.

sensor design; in fact, there have been discussions into sparser and more effective MEG sensor placements recently [73, 101], since certain OPM sensors can be placed on the head flexibly.

6.1 Problem statement

Our goal is to select a subset of optimal sensors that is able to sparsely sample the signal, yet still be able to reconstruct the full-state signal adequately well.

Let the full-state signal be $\mathbf{x} \in \mathbb{R}^{n \times m}$, where n is the total number of sensors, and m is the number of temporal samples. Also let $\boldsymbol{\eta} \in \mathbb{R}^{n \times m}$ be an additive independent identically distributed Gaussian noise $\mathcal{N}(0, \sigma^2)$. The signal may be represented by some basis $\mathbf{\Phi} \in \mathbb{R}^{n \times k}$,

$$\mathbf{x} = \mathbf{\Phi a} + \boldsymbol{\eta} \equiv \mathbf{\Phi}\hat{\mathbf{a}} \tag{6.1}$$

where k is the number of basis vectors/modes, and each column of $\mathbf{a} \in \mathbb{R}^{k \times m}$ contain the coefficients to each basis mode. We have also defined

$$\hat{\mathbf{a}} \equiv \mathbf{a} + \boldsymbol{\Phi}^{\dagger} \boldsymbol{\eta} \tag{6.2}$$

as the "noisy" coefficient/weights, where † denotes the Moore–Penrose pseudoinverse (in this case, the right pseudoinverse) [9, 52]. We want to find a matrix $\mathbf{P} \in \mathbb{R}^{p \times n}$ that picks out $p < n$ number of sensors to sample the signal, such that the full-state signal $\mathbf{x}$ can still be reconstructed accurately. Let us denote the reduced-state signal as $\mathbf{y} \in \mathbb{R}^{p \times m}$. The reduced-state signal is given by

$$\mathbf{y} = \mathbf{P}\boldsymbol{\Phi}\hat{\mathbf{a}} \equiv \boldsymbol{\Theta}\hat{\mathbf{a}} = \boldsymbol{\Theta}\mathbf{a} + \mathbf{P}\boldsymbol{\eta}, \tag{6.3}$$

where we have defined $\boldsymbol{\Theta} = \mathbf{P}\boldsymbol{\Phi}$. Evidently, $\mathbf{P}$ must be a permutation matrix with rows of canonical unit vectors that select the appropriate rows of $\boldsymbol{\Phi}$.

6.2 Low-rank subspaces and SVD

Many datasets and signals exhibit low-dimensional patterns in certain basis choices that may be exploited for easier computation. One such basis may be found via the SVD. SVD decomposes some signal $\mathbf{A} \in \mathbb{R}^{a \times b}$ into unitary matrices $\mathbf{U} \in \mathbb{R}^{a \times a}$ and $\mathbf{V} \in \mathbb{R}^{b \times b}$, and a diagonal matrix $\mathbf{S} \in \mathbb{R}^{a \times b}$ with non-negative entries (singular values),

$$\mathbf{A} = \mathbf{U}\mathbf{S}\mathbf{V}^{\dagger}, \tag{6.4}$$

where the singular value entries in the diagonal of $\mathbf{S}$ are arranged in decreasing order.

By the Eckart-Young theorem [19, 35], if we approximate $\mathbf{A}$ by truncating $\mathbf{U}$ and $\mathbf{V}$ of its SVD to the first r columns, then it is the optimal rank-r least-squares approximation of $\mathbf{A}$. In other words, the columns/modes of $\mathbf{U}$ and $\mathbf{V}$ with higher corresponding singular values have higher dominance in representing the entire signal. If a signal's SVD has only few significant singular values, then it can be well-approximated by just the first few modes of $\mathbf{U}$

and $\mathbf{V}$, reducing the signal from a high-dimensional subspace to a low-dimensional subspace.

Note that when $a > b$ (overdetermined), the lower $(a-b) \times b$ submatrix of $\mathbf{S}$ is necessarily null. Hence, we only need to consider the first b columns of $\mathbf{U}$ and $\mathbf{V}$. When $a < b$ (underdetermined), the rightmost $a \times (b-a)$ submatrix of $\mathbf{S}$ is null, hence we only need to consider the first a rows of $\mathbf{V}$. In any case, only the square submatrix of $\mathbf{S}$ with non-negative diagonal elements is kept. These two cases are the *economy SVD*, and are utilized to simplify computation [93]. We will use the economy SVD for the rest of the chapter, i.e., only $r \leq b$ or $r \leq a$ significant modes for the overdetermined and underdetermined cases respectively are preserved.

Since the SVD bases reveal the latent, low-dimensional significant modes that best represent the signal, a few rows of a rank-r truncated $\mathbf{U}$ (corresponding to sensors) can be selected to optimally represent the small number of r significant modes. In our context for MEG, we perform the SVD decomposition on the full-state signal $\mathbf{x}$ so that a low-dimensional r-basis representation $\mathbf{\Phi} = \mathbf{U} \in \mathbb{R}^{n \times r}$, $n \geq r$ is obtained as desired. This allows for $p \geq r$ sensors to be selected from $\mathbf{\Phi}$.

We note that the optimal number of sensors p needed to be selected in relation to the number of modes r for the best sparse measurement is not trivial. In [23, 100], it was suggest that the optimal number may be approximately equal to the underlying rank of the system in the chosen basis. As such, the $p < r$ case will not be considered here; we want at least $p = r$ chosen sensors so that all r basis modes are represented by the $p \geq r$ sensors and are hence useful. A discussion of the underdetermined case where $p < r$ can be found in [125].

The observation that $p = r$ selected sensors may be optimal also indicates the importance of using a low-dimensional basis representation of the signal for the purposes of sparse sensor selection. For instance, if an L-degree truncated SSS basis matrix (see Section 4.1) is used in place of the r-truncated $\mathbf{U}$, then at least $(L+1)^2 - 1$ sensors need to be selected as opposed to r. As higher frequency signals are measured, higher L degrees (and hence more sensors) are required, in agreement with the Nyquist sampling framework. For SVD modes however, as long as the signal exhibits low-dimensional spatiotemporal patterns, the number of significant

modes r remains low, allowing for a small number of sensors to still be picked.

6.3 Coefficient estimation and signal reconstruction

In order to reconstruct the noiseless signal $\mathbf{\Phi a}$, we need to obtain the unknown coefficients $\mathbf{a}$. However, in practice, only the noisy coefficient $\hat{\mathbf{a}}$ can be obtained as an estimate of $\mathbf{a}$ via taking the pseudoinverse of $\mathbf{\Theta}$,

$$\mathbf{\Theta}^{\dagger}\mathbf{y} = \hat{\mathbf{a}} = \mathbf{a} + \mathbf{\Phi}^{\dagger}\boldsymbol{\eta} = \begin{cases} \mathbf{\Theta}^{-1}\mathbf{y}, & p = r \\ \left(\mathbf{\Theta}^{T}\mathbf{\Theta}\right)^{-1}\mathbf{\Theta}^{T}\mathbf{y}, & p > r. \end{cases} \tag{6.5}$$

To improve the estimate of $\hat{\mathbf{a}}$ and hence obtain an accurate full-state signal reconstruction, we may minimize the absolute determinant (or equivalently, the volume) of the error covariance matrix $\mathrm{Var}[\mathbf{a} - \hat{\mathbf{a}}]$. A direct calculation shows that

$$\mathrm{Var}\left[\mathbf{a} - \hat{\mathbf{a}}\right] = \sigma^2 \left(\mathbf{\Phi}^{T}\mathbf{\Phi}\right)^{\dagger} = \sigma^2 \left(\mathbf{\Theta}^{T}\mathbf{\Theta}\right)^{-1}, \quad p \geq r, \tag{6.6}$$

where we have used the fact that $\mathbf{\Phi}^{\dagger} = \mathbf{\Theta}^{\dagger}\mathbf{P}$ from the definition of $\mathbf{\Theta}$. This tells us that to maximize this error covariance matrix, we may equivalently maximize the determinant of $\mathbf{\Theta}^{T}\mathbf{\Theta}$ (due to the inverse). This can be achieved by permuting its rows in an optimal manner using the pivoted QR algorithm (which will be discussed in the next section) so that it corresponds to ranking sensors that best represent the basis modes. Compactly written, this entire procedure is equivalent to finding an index set $\gamma = \{\gamma_1, \ldots, \gamma_p\} \subseteq \{1, \ldots, n\}$ such that

$$\gamma^{*} = \underset{\gamma, |\gamma| = p}{\mathrm{argmax}} \left|\det\left(\mathbf{\Theta}_{\gamma}^{T}\mathbf{\Theta}_{\gamma}\right)\right|, \quad p \geq r, \tag{6.7}$$

where $\mathbf{\Theta}_{\gamma} = \mathbf{P}_{\gamma}\mathbf{\Phi}$, and $\mathbf{P}_{\gamma}$ is the appropriate permutation matrix that selects and permutes the p rows of $\mathbf{\Phi}$ as dictated by γ.

Since $\mathbf{\Theta}^{T}\mathbf{\Theta}$ is square, its determinant is the product of its eigenvalues. Moreover, $\mathbf{\Theta}^{T}\mathbf{\Theta}$ is symmetric positive semidefinite, so its eigenvalues coincide with its singular values σ. We

know that the first r eigenvalues/singular values of $\boldsymbol{\Theta}^T\boldsymbol{\Theta}$ and $\boldsymbol{\Theta}\boldsymbol{\Theta}^T$ are identical, so (6.7) is equivalently

$$\begin{aligned}\gamma^* &= \underset{\gamma,|\gamma|=p}{\operatorname{argmax}} \left|\prod_{i=1}^{r} \sigma_i(\boldsymbol{\Theta}_\gamma^T\boldsymbol{\Theta}_\gamma)\right| = \underset{\gamma,|\gamma|=p}{\operatorname{argmax}} \left|\prod_{i=1}^{r} \sigma_i(\boldsymbol{\Theta}_\gamma\boldsymbol{\Theta}_\gamma^T)\right| \\ &= \underset{\gamma,|\gamma|=p}{\operatorname{argmax}} \left|\det\left(\boldsymbol{\Theta}_\gamma\boldsymbol{\Theta}_\gamma^T\right)\right|, \quad p \geq r. \end{aligned} \tag{6.8}$$

Note that the parentheses on the second and third equalities do not indicate multiplication, but instead they indicate that the singular values σ are that of $\boldsymbol{\Theta}^T\boldsymbol{\Theta}$ and $\boldsymbol{\Theta}\boldsymbol{\Theta}^T$ respectively.

In the $p = r$ case where $\boldsymbol{\Theta}$ is square, we know that $\det\boldsymbol{\Theta}^T = \det\boldsymbol{\Theta}$, so $\det\left(\boldsymbol{\Theta}^T\boldsymbol{\Theta}\right) = \det\boldsymbol{\Theta}^T\det\boldsymbol{\Theta} = (\det\boldsymbol{\Theta})^2$. We thus only need to maximize the determinant of $\boldsymbol{\Theta}$,

$$\gamma^* = \underset{\gamma,|\gamma|=p}{\operatorname{argmax}} |\det\boldsymbol{\Theta}_\gamma|, \quad p = r. \tag{6.9}$$

6.4 QR pivoting algorithm

We now summarize the steps of the QR pivoting algorithm, which will provide a solution to $\mathbf{P}_\gamma$ in (6.8) and (6.9). There are other sparse selection algorithms for high-dimensional problems [37, 38, 161], but the QR algorithm provides exceptional performance with minimal computational cost.

The QR pivoting algorithm was first introduced in [20], but its application towards greedy sensor selection has only been done recently in [19, 33, 100, 148]. It follows the usual QR algorithm that decomposes some matrix $\mathbf{A} \in \mathbb{R}^{a\times b}$ into a unitary matrix $\mathbf{Q} \in \mathbb{R}^{a\times a}$ and an upper triangular matrix $\mathbf{R} \in \mathbb{R}^{a\times b}$, except that at each iterative step, the column with the largest 2-norm is first selected and then swapped with the first column. The pivoted QR decomposition hence includes a column permutation matrix $\mathbf{P}' \in \mathbb{R}^{b\times b}$ that accounts for this added step,

$$\mathbf{A}\mathbf{P}' = \mathbf{Q}\mathbf{R}. \tag{6.10}$$

Consider the first iteration. The first step as mentioned is to select the column of $\mathbf{A}$ with the largest 2-norm, and then swap it with the first column. Assuming the column with largest 2-norm is the k^{th} column, this is equivalent to right multiplying $\mathbf{A}$ by the permutation matrix

$$\mathbf{P}_1 = \begin{bmatrix} \mathbf{e}_k & \mathbf{e}_2 & \dots & \mathbf{e}_{k-1} & \mathbf{e}_1 & \mathbf{e}_{k+1} & \dots & \mathbf{e}_b \end{bmatrix}, \tag{6.11}$$

where $\mathbf{e}_k \in \mathbb{R}^{b\times 1}$ denotes the k^{th} canonical basis vector, and $\mathbf{P}_1$ denotes the permutation matrix for the first iteration of the QR pivoting algorithm. After the swap, we apply a Householder transformation $\mathbf{Q}_1$ on the first column of the resulting $\mathbf{AP}_1$, which corresponds to a reflection of the vector with respect to its orthogonal subspace. Let $\mathbf{b}_1 \equiv \mathbf{a}_1 - \|\mathbf{a}_1\|\mathbf{e}_1$ where $\mathbf{a}_1$ is the first column of $\mathbf{A}$. The Householder transformation is

$$\mathbf{Q}_1 = \mathbf{I} - \frac{2\mathbf{b}_1\mathbf{b}_1^*}{\|\mathbf{b}_1\|^2}, \tag{6.12}$$

where $\mathbf{I} \in \mathbb{R}^{a\times a}$ is the identity matrix. A straightforward calculation shows that

$$\mathbf{Q}_1\mathbf{AP}_1 = \begin{bmatrix} \|\mathbf{a}_k\| & * & \dots & * \\ 0 & & & \\ \vdots & & \mathbf{A}^{(2)} & \\ 0 & & & \end{bmatrix}, \tag{6.13}$$

where $\mathbf{A}^{(2)} \in \mathbb{R}^{(a-1)\times(b-1)}$ is the submatrix of $\mathbf{A}$ excluding the first row and column. We denote $\mathbf{A}^{(k)}$ as the bottom right $(a-k+1)\times(b-k+1)$ submatrix of $\mathbf{A}$ (so $\mathbf{A} = \mathbf{A}^{(1)}$).

The same process is repeated for $\mathbf{A}^{(2)}$ and subsequent submatrices until $\mathbf{A}$ is decomposed into an upper triangular matrix. In order for the Householder transformation and permutation matrix at the k^{th} iteration to act on the appropriate submatrix $\mathbf{A}^{(k)}$, they must resemble the

form

$$\mathbf{Q}_k = \begin{bmatrix} \mathbf{I} & 0 & \dots & 0 \\ 0 & & & \\ \vdots & & \mathbf{Q}_k^{(k)} & \\ 0 & & & \end{bmatrix} \qquad \mathbf{P}_k = \begin{bmatrix} \mathbf{I} & 0 & \dots & 0 \\ 0 & & & \\ \vdots & & \mathbf{P}_k^{(k)} & \\ 0 & & & \end{bmatrix}, \tag{6.14}$$

with $\mathbf{I} \in \mathbf{R}^{(k-1)\times(k-1)}$. The application of a Householder transformation guarantees an upper triangular matrix due to the resulting form of (6.13) at the end of every iteration. In the case of $a > b$, this is achieved after b iterations, and in the case of $a \leq b$, it is achieved after a iterations.

For $a \leq b$, the final result will be

$$\mathbf{Q}_a \dots \mathbf{Q}_2\mathbf{Q}_1\mathbf{A}\mathbf{P}_1\mathbf{P}_2 \dots \mathbf{P}_a = \begin{bmatrix} \left\|\mathbf{a}_{k_1}^{(1)}\right\| & * & * & * & * & \dots & * \\ 0 & \left\|\mathbf{a}_{k_2}^{(2)}\right\| & * & * & * & \dots & * \\ 0 & 0 & \ddots & * & * & \dots & * \\ 0 & 0 & 0 & \left\|\mathbf{a}_{k_a}^{(a)}\right\| & * & \dots & * \end{bmatrix}, \tag{6.15}$$

i.e.,

$$\mathbf{R} = \mathbf{Q}_a \dots \mathbf{Q}_2\mathbf{Q}_1\mathbf{A}\mathbf{P}_1\mathbf{P}_2 \dots \mathbf{P}_a \tag{6.16}$$

$$\mathbf{P}' = \mathbf{P}_1\mathbf{P}_2 \dots \mathbf{P}_a \tag{6.17}$$

$$\mathbf{Q} = (\mathbf{Q}_a \dots \mathbf{Q}_2\mathbf{Q}_1)^\dagger . \tag{6.18}$$

The upper triangular result (6.15) has a diagonal dominant structure, since its diagonal entries are the greedily-obtained maximum column 2-norms at each iteration. Since the determinant of a triangular matrix is the product of its diagonal elements, this tells us that QR pivoting greedily maximizes the determinant of $\mathbf{R}(1:a, 1:a)$ (the first $a \times a$ submatrix

of $\mathbf{R}$). We have

$$|\det \mathbf{R}(1:a,1:a)| = \left|\det\left(\mathbf{Q}^\dagger \mathbf{A}\mathbf{P}'(:,1:a)\right)\right| = |\det\left(\mathbf{A}\mathbf{P}'(:,1:a)\right)|, \tag{6.19}$$

since $\mathbf{Q}^\dagger$ is unitary so $\left|\det \mathbf{Q}^\dagger\right| = 1$. For the $a = b$ case, this can be further simplified to become

$$|\det \mathbf{R}| = \left|\det\left(\mathbf{Q}^\dagger \mathbf{A}\mathbf{P}'\right)\right| = |\det \mathbf{A}|, \tag{6.20}$$

since for (square) permutation matrices, $|\det \mathbf{P}'| = 1$.

In our context, the goal is is to permute the rows of $\mathbf{\Theta}\mathbf{\Theta}^T$ or $\mathbf{\Theta}$ for the $p > r$ or $p = r$ case respectively, such that (6.8) and (6.9) are satisfied. For maximum sparsity, we consider only the $p = r$ case, so that a minimum number of sensors are required to adequately sample the r modes. We thus perform QR pivoting on $\mathbf{A} = \mathbf{\Phi}^T = \mathbf{U}^T$ (transposed since QR pivoting acts on columns) so that eventually, $\left|\det \mathbf{\Phi}^T(1:r,1:r)\right|$ as in (6.19) is greedily maximized, with (6.9) having the solution $\mathbf{P}_\gamma = \mathbf{P}'(1:n,1:r)$.

For the $p > r$ case, one way to approximately satisfy (6.8) is to maximize the determinant of $\mathbf{\Phi}\mathbf{\Phi}^T$. Performing QR pivoting on $\mathbf{A} = \mathbf{\Phi}\mathbf{\Phi}^T$ greedily maximizes (6.20); however, it has been shown in [125] that this is in fact not optimized to solve (6.8). It only provides a somewhat informed sensor selection that still has better performance than random sensor selection. In the same paper [125], an improved extended algorithm for sensor selection in the $p > r$ case is provided.

6.5 Signal reconstruction and source localization using QR-selected sensors

To evaluate the QR pivoting sensor selection algorithm and its performance in the context of MEG, we consider two example scenario datasets. The first is a standard phantom measurement, which allows us to test our method on a known ground truth. The second dataset is a binaural signal, which shows an application of our algorithm workflow to realistic experimental data. These datasets were obtained from the Brainstorm website

(http://neuroimage.usc.edu/brainstorm), and all data analyses performed on them were done with Brainstorm, which is documented and freely available for download online under the GNU general public license [141].

6.5.1 2000 nAm and 200 nAm phantom signals

The first dataset that we considered was a measurement performed by John Mosher (Epilepsy Center, Cleveland Clinic Neurological Institute, Cleveland, Ohio, USA) using a 306-channel Elekta Neuromag system (Megin, Helsinki, Finland) with a dry current phantom. The dataset is provided by Ken Taylor and John Mosher on the Brainstorm website (https://neuroimage.usc.edu/brainstorm/Tutorials/PhantomElekta).

The phantom contains 32 dipole sources located at 4 different distances from the origin (33.9 mm, 44.0 mm, 54.0 mm, and 63.9 mm), and is a well-established model for validating MEG systems and methods. We used two sets of measurements, one with the sources having dipole moments of 2000 nAm, and the other 200 nAm; they correspond to unrealistically high and realistic source strengths respectively.

The dipoles are sequentially activated, and 32 epochs, each corresponding to one dipole activation, are selected from each of the 2000 nAm and 200 nAm datasets to test the QR pivoting algorithm for sensor selection. We followed the tutorial provided on the above Brainstorm website for signal processing, except the epochs was kept at the original 1000 Hz sampling rate and not resampled to 100 Hz. Note that from here on, we will refer to these epochs as "datasets" still, for convenience.

6.5.1.1 Signal reconstruction

We first performed SVD on each of the 32 datasets for the 2 different source strengths to obtain the r-truncated left singular SVD basis matrix, as well as the singular value spectrum. QR pivoting algorithm was then performed on this basis matrix to select $p = r$ optimal sensors.

To show that the number of modes/sensors to keep cam ne estimated from the singular value curve, for each $r = 1, \ldots, n$ SVD basis truncation, we obtained the full-state signal

reconstruction $\hat{\mathbf{x}}_p$ for a $p = r$ QR-selected sensor measurement. This was done using (6.1) and (6.5). Then, the relative error (RE) was calculated via

$$\mathrm{RE}_p = \frac{\|\mathbf{x} - \hat{\mathbf{x}}_p\|}{\|\mathbf{x}\|}. \tag{6.21}$$

In Figure 6.2, the singular value spectrum and REs for the 200 nAm and 2000 nAm cases (each averaged over their 32 epochs) are shown.

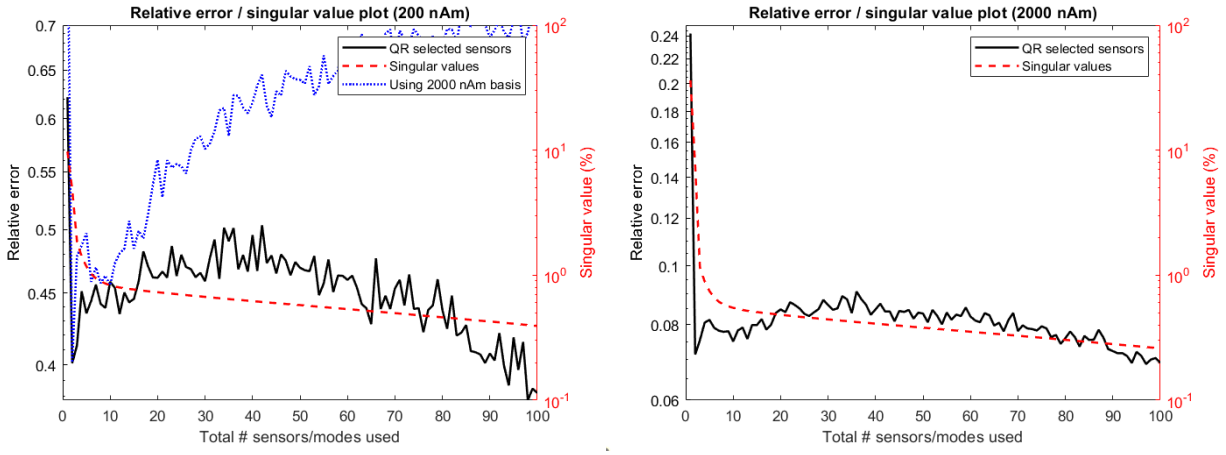

(a) (b)

Figure 6.2: All curves are averaged over the 32 phantom dipolar source results. (a) Plots for the 200 nAm case. The dashed red curve shows the singular value spectrum, and the solid black curve shows the RE of the reconstructed signals. The elbow of the singular value spectrum occurs at approximately 2-10 modes, with agrees with the minimum range of the RE curve. The RE curve increases afterwards, peaking at around 35 modes, before decreasing again. The blue dotted curve shows the RE when the 2000 nAm SVD basis was used for signal reconstruction. Again, low RE is observed between 2-10 modes before it increases, this time peaking much higher at a value above 35 modes. (b) Plots for the 2000 nAm case. The behavior of the curves are similar to the 200 nAm case.

Figure 6.2 highlights two important aspects of the data: (i) its low-dimensional structure, and (ii) its ability to be reconstructed with limited measurements. Specifically, this figure shows that for both high and low signal strengths, there exists a low-dimensional embedding

to global SVD modes. The elbow of the singular value curve for both 200 nAm and 2000 nAm cases appear to be at around 2-10 modes. Correspondingly, there is low RE within that domain, before RE increases to a peak at around 35 modes. This indicates that it is appropriate to truncate at the number of modes corresponding to the elbow of the singular value curve.

The behavior of the RE curve is expected and may be explained as follows. The first few significant SVD modes correspond to modes representing meaningful features of the signal (or "informative" modes), hence RE decreases. The subsequent modes correspond to noise, or are noisy modes [36, 47]. By including just a few of these noisy modes, the actual random noise in the signal cannot be projected onto them accurately, thus error increases. If we continue increasing the number of noisy modes used however, noise can be more accurately represented gradually, and error starts decreasing again. The observation that the 2000 nAm dataset (with higher SNR) has larger first few singular values also indicates that the first few significant modes are informative and indeed correspond to signals, whereas the subsequent modes correspond to noise.

To illustrate how very sparse sampling can yield results that capture the important underlying dynamics of the signal, we will use the 2-mode QR reconstruction with 2 sensors (which lies within the 2-10 informative mode range). Figure 6.3 shows the signals of one of the 200 nAm dipoles as an image plot. The original signal is on the left (OG), the 2-mode QR and 2-mode SVD reconstructions are in the middle column, and the first 2 SVD modes are in the rightmost column. The 2-mode QR reconstruction using 2 sensors yields comparable results to the 2-mode SVD reconstruction using all 306 sensors, signifying the redundancy of many sensors. Only 2 optimally-selected sensors that best represent the 2 SVD modes are required to reconstruct the signal. We also see that the first SVD mode resembles the original signal strongly, illustrating that it is an informative mode.

Figures 6.4 and 6.5 show the original (interpolated) magnetic flux field for each of the 32 dipole sources on the left, as well as the 2-mode QR reconstructed fields with the 2 selected sensors on the right. Similar to Figure 6.3, we see that the 2-mode QR reconstructed fields

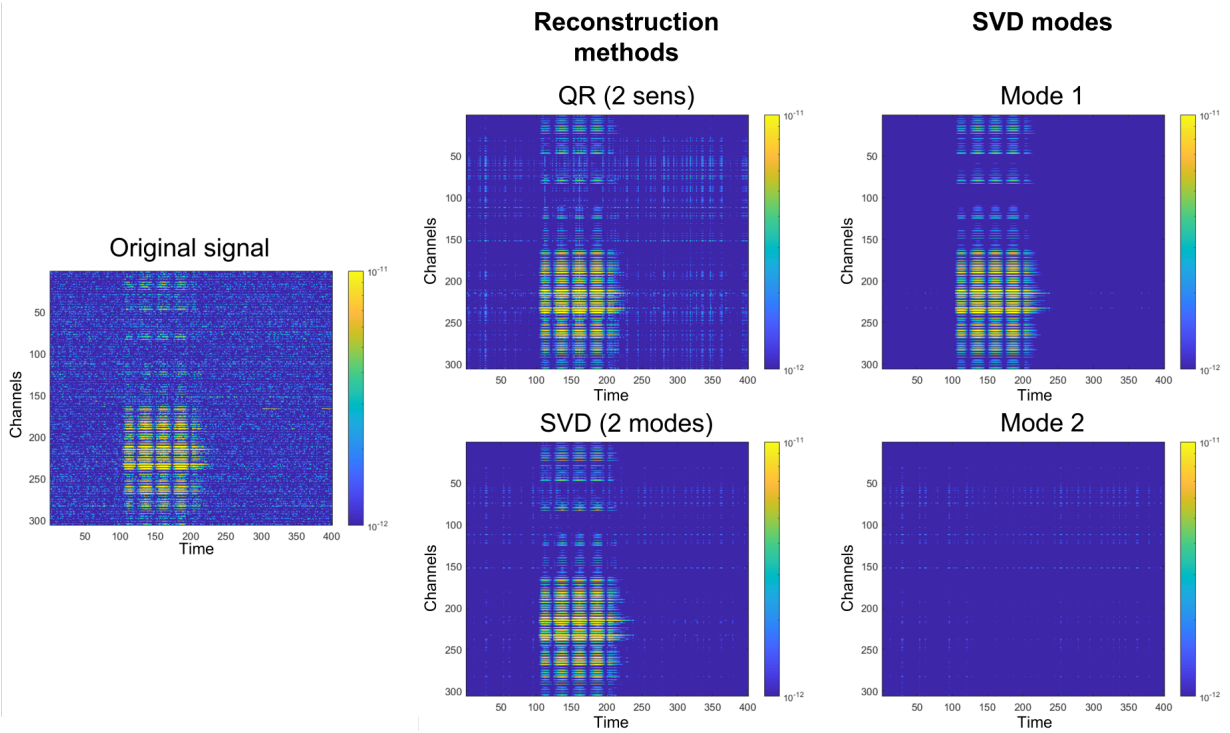

Figure 6.3: Image plots of the original signal (left column) and reconstructed signal (middle column) for a (-5.97,0,2.29) cm, 200 nAm phantom dipolar source. The 2-mode 2-sensor QR reconstruction has similar performance to the 2-mode 306-sensor SVD reconstruction, indicating the redundancy of dense sensor arrays. (Right column) Plots of the first 2 SVD modes. The first mode captures most of the spatiotemporal dynamics of the original signal, showing how low-dimensional signals only have a few significant and informative modes.

are visually similar to the original. The selected sensor positions also indicate that sensor selection is dependent on source location; at least one sensor close to the vicinity of source activity is always selected, and the 2 sensors selected across the rows of Figures 6.4b and 6.5b (which have same tangential coordinates but different radial depths) are generally placed in similar locations. As expected, for the stronger 2000 nAm case, the sensor locations are more consistently chosen due to the higher SNR that reveals the true dipolar signal pattern more clearly.

6.5.1.2 Source localization

Here, we investigate if performing ECD fits on full-state signals that are reconstructed from sparse measurements can result in accurate source localizations. The ECD fit function provided in Brainstorm was used for reconstructions of each of the 32 dipole datasets of both source strengths, and the absolute position and orientation errors relative to the true phantom dipoles were calculated.

Figures 6.6 shows the ECD position and orientation errors using QR and SVD reconstruction methods on the 200 nAm datasets, whereas Figure 6.7 shows the results for 2000 nAm datasets. The errors are plot with respect to dipole source distance from the origin, thus each data point is obtained by averaging the errors of the $32/4 = 8$ dipoles that have the same radial distance.

For the 200 nAm case in Figure 6.6, the 2-mode 2-sensor QR localization is comparable to both the 2-mode 306-sensor SVD and original localizations, again indicating the redundancy of sensors if working in the SVD basis. The 35-mode 35-sensor QR localization suffers from poorer results at deep source distances, which is to be expected given that it has passed the informative mode range into the region with higher RE (see Figure 6.2).

We also notice that in general, deeper sources had poorer source localization. This can be understood from previous discussions in Sections 4.1 and 4.2.1 – the source-to-sensor distance for deep sources are larger, which results in a lower resolution signal that have low spatial frequency components. These low l degree components cannot achieve solutions that are as

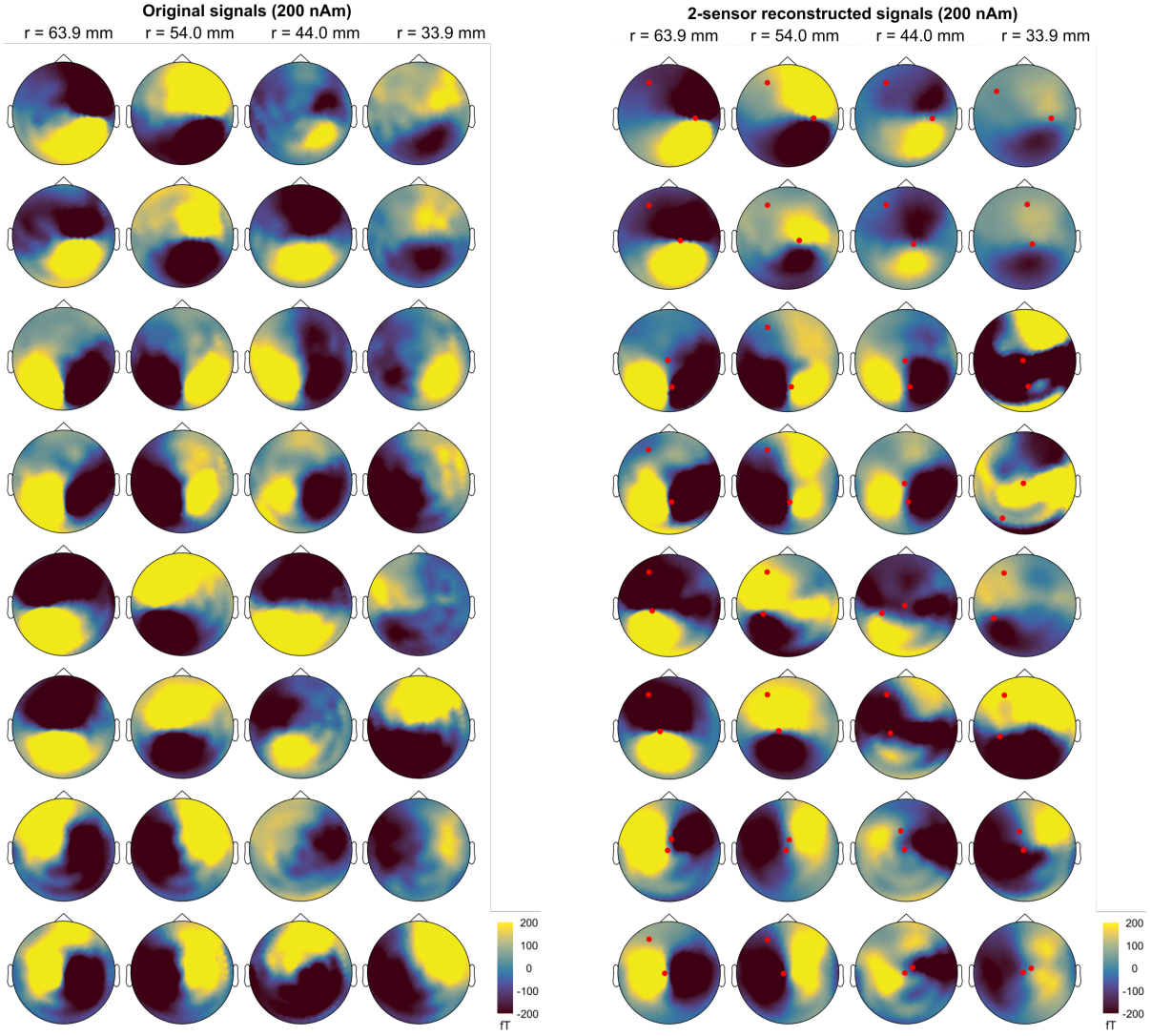

(a) (b)

Figure 6.4: (a) Original signals for each of the 200 nAm 32 phantom dipolar sources. (b) 2-mode QR reconstructed signals, with the 2 selected sensors indicated by the red dots. There is a high reconstruction accuracy of the signal patterns, and sensor selection appears to be source-dependent, with at least one always being selected close to the source activity.

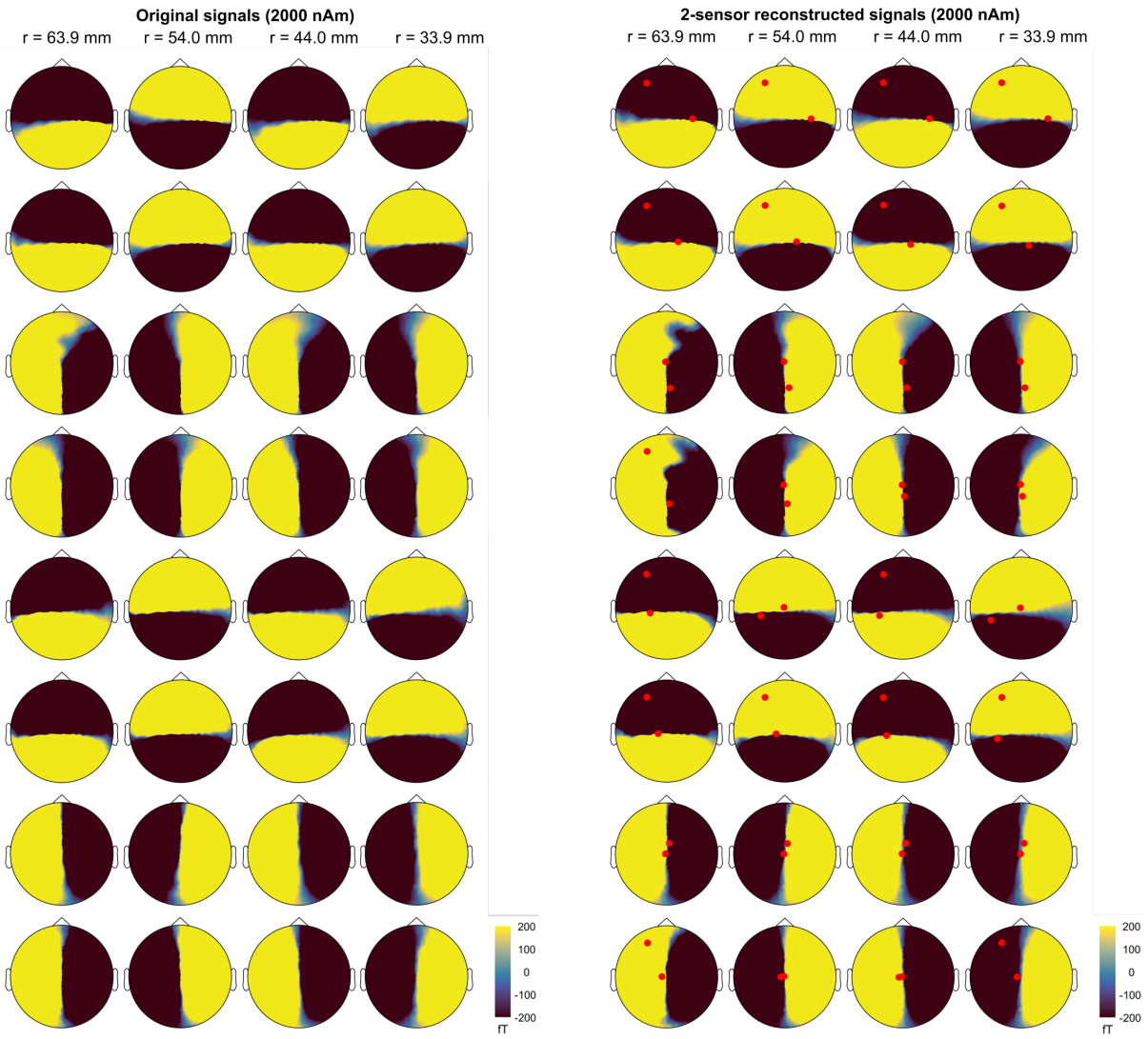

(a) (b)

Figure 6.5: (a) Original signals for each of the 2000 nAm 32 phantom dipolar sources. Note the more distinct dipolar field patterns due to the higher SNR. (b) 2-mode QR reconstructed signals, with the 2 selected sensors indicated by the red dots. There is a very high reconstruction accuracy of the signal patterns, and the selected sensors are nearly all identical for sources with the same tangential coordinates but at different depths.

accurate as higher l degree components due to their larger area of convergence that has a less steep descent into the true solution as seen in Figure 4.2.

For the 2000 nAm case in Figure 6.7, the unrealistically high SNR resulted in all the ECD fits performing identically well, with < 2 mm and $< 4.5°$ position and orientation errors respectively. Note that the behavior of the position error plot agrees with the high SNR ECD error plots in Section 5.3.4, i.e., deep and superficial sources have the highest errors. This may indicate some effects from BEM head model errors, but is not definitive.

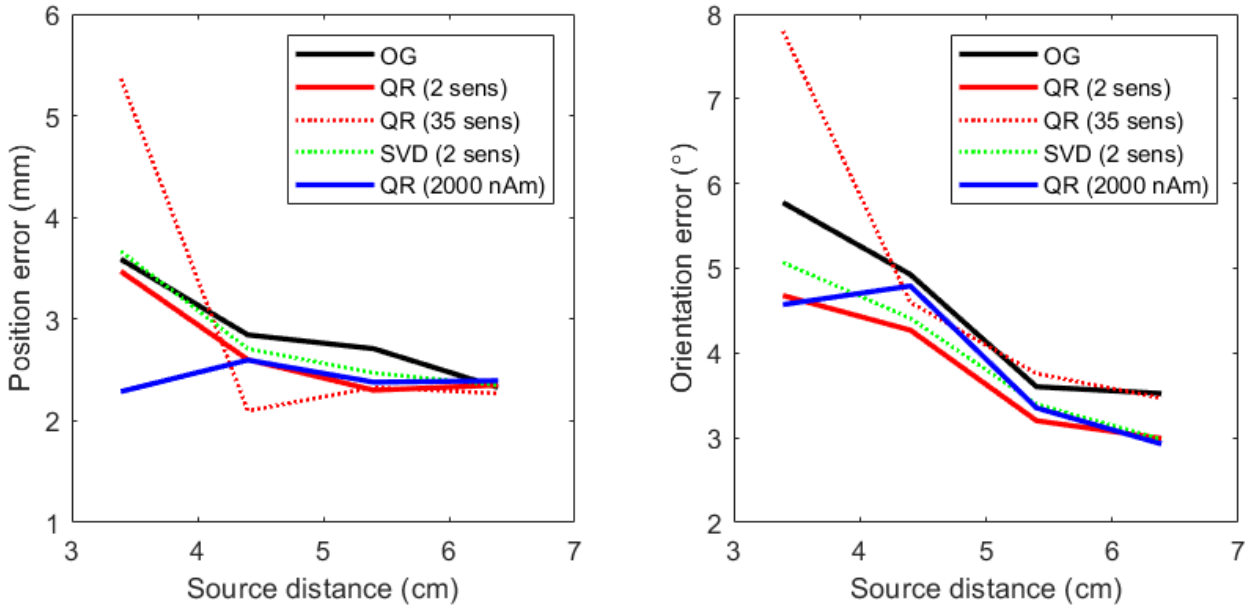

Figure 6.6: Position errors (left) and orientation errors (right) of ECD fits using various reconstructed 200 nAm signals. All cases except when using 2000 nAm basis had higher localization errors for deep sources, especially the 35-mode QR case, indicating that using more modes/sensors does not guarantee better performance. For more superficial sources, all cases including the 2-mode QR case had similar localization performance, indicating a redundancy in sensors.

6.5.2 Using 2000 nAm basis for 200 nAm signal

In reality, if we want to have a system of p sensors, we will need to obtain information about where to place them from either a simulation or prior datasets measured with a dense sensor

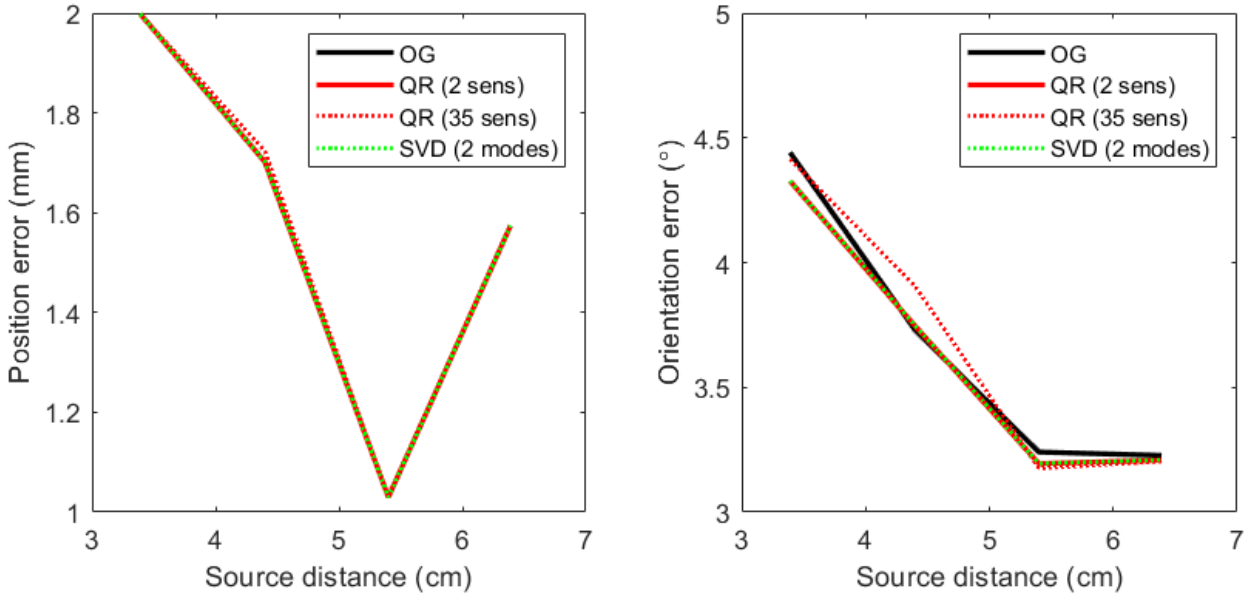

Figure 6.7: Position errors (left) and orientation errors (right) of ECD fits using 2000 nAm signals. All cases performed identically well due to the high SNR.

array. The basis matrix from a full-state signal is also required for a reconstruction from the p-sensor sparse measurement. As observed previously in Section 6.5.1.1, since sensor selection appears to be dependent on source location, the sources for these simulations/prior recordings will likely need to be approximately the same as what we expect in order to obtain the near-optimal p sensor selection.

Here, we verify that it is possible to attain an accurate full-state signal reconstruction and source localization if the optimal p sensor locations and SVD basis are both obtained from a simulation/prior dataset. The simulation/prior dataset that we used is the 2000 nAm dataset with all 306 sensors, which mimics an overly-ideal simulation with high SNR, whereas the optimal sparse p-sensor measurement were from the 200 nAm dataset.

The results are shown in the blue curves of Figures 6.2 and 6.6. In Figure 6.2, we see that the RE for the reconstructed signal in this case is comparable to using the 200 nAm basis (black curve) up to about 10 modes as expected, since these first few significant modes represent the identical clean signal. However, the RE increases rapidly afterwards. This may

be explained by how the subsequent modes for the 2000 nAm basis are cleaner and do not represent the noise of the 200 nAm signal well. If more 2000 nAm modes are included, the error eventually decreases since the noise becomes represented better gradually (as explained in Section 6.5.1). This occurs at a significantly higher number of modes than if the 200 nAm basis itself was used; if the plot is extended to beyond 100 sensors/modes, the blue curve eventually decreases.

The ECD errors for this case performs comparably to the original source localization methods, as seen in Figure 6.6. However, it is interesting to note that now, deep sources suffer from decreased position and orientation errors. This indicates that using a basis from high SNR signals may have noise suppression capabilities when reconstructing noisy data. Intuitively, this may be understood by the fact that we are interpolating data the p sparse sensor measurements based on the clean basis. Thus if a clean basis is used, less noise will be reconstructed, leading to an improved inverse model.

6.5.3 Sensor selection on binaural stimulation signal

To show the validity of the QR pivoting sensor selection algorithm on realistic measurements, we now consider a binaural stimulation dataset. It is a measurement done by Elizabeth Bock, Peter Donhauser, Francois Tadel, and Sylvain Baillet (MEG Unit Lab, McConnell Brain Imaging Center, Montreal Neurological Institute, McGill University, Canada) using a CTF 275 system with 274 axial gradiometers (https://neuroimage.usc.edu/brainstorm/DatasetIntroduction).

We followed the Brainstorm tutorial to identify the relevant epoch/dataset with dipolar-like activity for analysis. Like before, SVD was performed on the dataset, followed by QR pivoting on the SVD basis for sensor selection. Signal reconstruction and ECD source localization were then carried out.

The results are shown in Figure 6.8. In Figure 6.8a, the singular value spectrum now does not have a distinct elbow and decays gradually due to the more complex source configuration and higher noise levels. Due to the low SNR, there is no increase then decrease of RE as

more modes are gradually included, since all modes are likely noisy.

We estimate based on the singular value spectrum that 30 sensors/modes are sufficient for accurate reconstruction. The RE curve of the p-mode QR signal reconstruction follows the singular value curve, indicating again that selecting the number of sensors/modes based of the singular value curve is valid. An ECD fit was then done using both the original data and the 30-mode QR reconstructed signal; the result is visually presented in Figure 6.8b. The fit using the original data is displayed as a red dipole, whereas the fit using the 30-mode QR reconstructed signal is displayed as a green dipole. Their localization differences are small (hence the large overlap between the two dipoles), with a 1.41 mm position difference and a 0.80° orientation difference. This indicates that the localization performance using just 30 sensors is comparable to using the full array of 274 sensors.

6.6 Limitations and further comments

So far, our results suggest that it is possible to utilize sparse sensor array measurements in MEG to reconstruct full-state signals. We note that such signal reconstructions from sparse data relies heavily on the basis choice obtained from simulations/prior datasets. If the source configurations of these simulations/prior datasets do not resemble the actual source configuration, large reconstruction errors may occur. The above sensor selection algorithm thus works best for replicable or consistent source configurations.

Another limitation is that for sparse sensor arrays, there may be an increased importance in co-registration errors [160]. Without a full-head coverage, the signals may become more sensitive to sensor position errors, especially if it is a deviation away from an optimal position. An inaccurate full-state reconstruction may hence result. We also acknowledge the advantages to having sensor redundancy; having a dense sampling of the head gives a more comprehensive measurement of head activity without the need for signal reconstruction. Practically, more sensors also mean more backups in case of sensor failure.

As a final note, the sensor selection pipeline presented in this paper may also be extended to EEG, which has a similar mathematical formulation to MEG. It is also in theory possible to apply it to determine optimal sampling points across a sensor surface/volume (as opposed

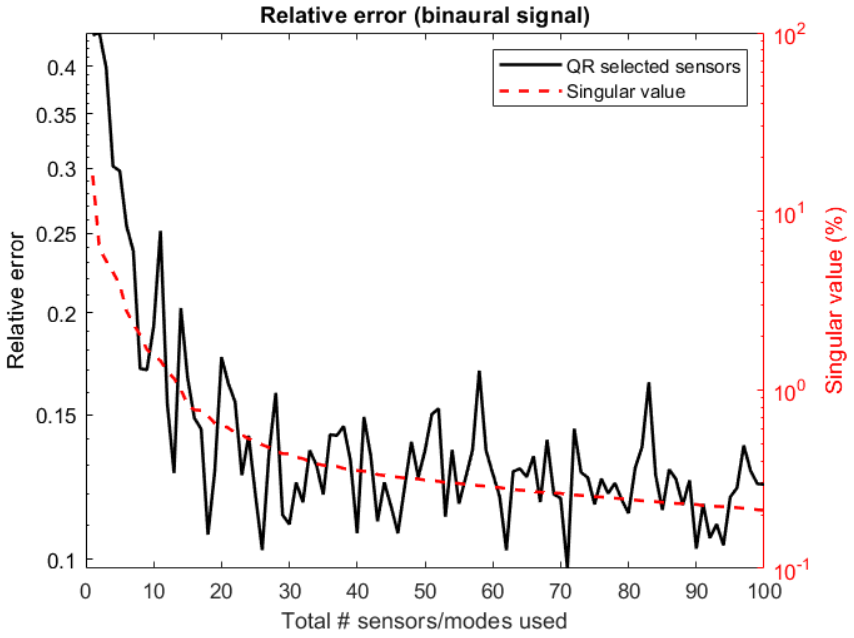

(a)

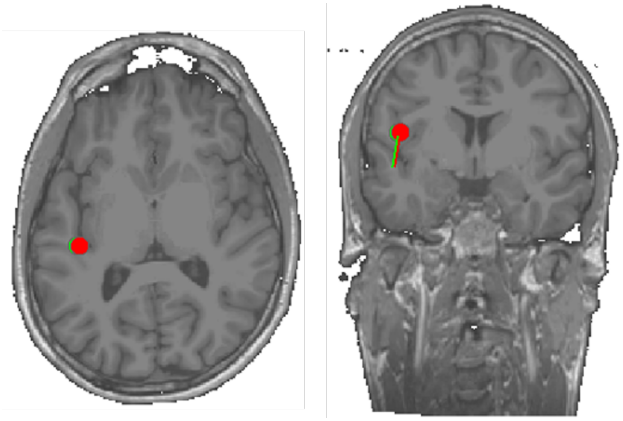

(b)

Figure 6.8: (a) RE plot for the p-mode reconstructed binaural signal (black curve), and the singular value plot of the full-state data (red curve). The RE plot follows the singular value spectrum, indicating that the number of modes/sensors can be selected from the latter. (b) Superior (left) and posterior (right) views of the head MRI. The ECD result using the full 274-sensor original signal (red) and 30-mode QR reconstructed signal (green) are shown. The performances are near-identical with a 1.41 mm and 0.80° discrepancy, indicating sensor redundancy.

to cubature sampling points as seen in Chapter 4), although its performance relative to current evaluation methods are a topic for future study.

Chapter 7

CONCLUSION

In this dissertation, we have evaluated the validity of cubature flux approximations and inaccurate BEM head models in relation to higher spatial resolution signals that are expected to be measured. We have also proposed using the QR pivoting algorithm for greedy optimal sensor selection as an alternative to the more common strive towards denser sensor arrays. In the process, the re-formulation and generalization of the quasi-static electromagnetic framework of MEG was done, which brought to attention a fundamental source of error that may significantly affect many aspects of MEG, such as source interpretations and sensor orientation considerations.

We will conclude with a brief summary of the main findings and contributions as follows.

A formula was derived for the electro-quasi-static magnetic scalar potential and magnetic field in a source-less region, which is shown to be the generalization of currently-used expressions in MEG. With our novel formulas, it is seen that radial current sources are magnetically silent. This tells us that open current segments have translationally non-invariant contributions, and thus any forward/inverse models and physical interpretations must be made cautiously with the origin choice in mind.

The magnetic flux calculation, which is typically done using cubature approximations, was simplified into a line integral form that can be more easily evaluated by software. For tangential circular sensors, a purely recursive and exact evaluation of each l-degree flux portion was derived. It was found that higher l-degree signal portions, decreased sensor array distances, and larger sensor surface areas had increased cubature approximation errors. 7-point and 9-point cubature approximations for circular and square sensors respectively are

likely sufficient for current SQUID-based MEG setups.

Higher spatial frequency signal portions were also found to be more sensitive to BEM head model errors. Thus, for signals with SNR $\geq$ 6 dB, closer sensors to the head are more sensitive to BEM head model inaccuracies due to their ability to resolve these inaccurate high spatial frequency components. This leads to increased signal and source localization errors. For signals with SNR $\leq$ 6 dB, the advantage of having a higher SNR when placing sensors closer to the head outweighs the effects of the inaccurate high spatial frequency signal components. Thus, signal error and source localization errors decrease.

We have also demonstrated that for MEG signals with latent low-rank SVD representation, a small number of optimal sensors can be selected such that they are able to reconstruct the full-state signal with high spatiotemporal fidelity. This is assuming that a basis can be obtained from prior datasets or simulations with similar underlying sources. The sensors selected depend on the source location, and ECD fits performed on the reconstructed signals resulted in comparable performances to using the original signal, indicating sensor redundancy.

BIBLIOGRAPHY

[1] Milton Abramowitz, Irene A Stegun, and Robert H Romer. Handbook of mathematical functions with formulas, graphs, and mathematical tables, 1988.

[2] Seppo P Ahlfors, Jooman Han, John W Belliveau, and Matti S Hämäläinen. Sensitivity of meg and eeg to source orientation. *Brain topography*, 23(3):227–232, 2010.

[3] Seppo P Ahlfors and Maria Mody. Overview of meg. *Organizational research methods*, 22(1):95–115, 2019.

[4] Lau M Andersen, Robert Oostenveld, Christoph Pfeiffer, Silvia Ruffieux, Veikko Jousmäki, Matti Hämäläinen, Justin F Schneiderman, and Daniel Lundqvist. Similarities and differences between on-scalp and conventional in-helmet magnetoencephalography recordings. *PLoS One*, 12(7):e0178602, 2017.

[5] George Backus, Backus George, Robert Ladislav Parker, Robert Parker, and Catherine Constable. *Foundations of geomagnetism*. Cambridge University Press, 1996.

[6] AI Bagić, RC Knowlton, DF Rose, et al. American clinical magnetoencephalography society clinical practice guideline 3: Meg-eeg reporting. jclinneurophysiol28: 362–363, 2011.

[7] Dale L Bailey, Michael N Maisey, David W Townsend, and Peter E Valk. *Positron emission tomography*, volume 2. Springer, 2005.

[8] Sylvain Baillet, John C Mosher, and Richard M Leahy. Electromagnetic brain mapping. *IEEE Signal processing magazine*, 18(6):14–30, 2001.

[9] João Carlos Alves Barata and Mahir Saleh Hussein. The moore–penrose pseudoinverse: A tutorial review of the theory. *Brazilian Journal of Physics*, 42(1):146–165, 2012.

[10] Leandro Beltrachini, Nicolas von Ellenrieder, Roland Eichardt, and Jens Haueisen. Optimal design of on-scalp electromagnetic sensor arrays for brain source localisation. *Hum. Brain Mapp.*, 42(15):4869–4879, 2021.

[11] Amir Borna, Tony R Carter, Anthony P Colombo, Yuan-Yu Jau, Jim McKay, Michael Weisend, Samu Taulu, Julia M Stephen, and Peter DD Schwindt. Non-invasive functional-brain-imaging with an opm-based magnetoencephalography system. *Plos one*, 15(1):e0227684, 2020.

[12] Amir Borna, Tony R Carter, Josh D Goldberg, Anthony P Colombo, Yuan-Yu Jau, Christopher Berry, Jim McKay, Julia Stephen, Michael Weisend, and Peter DD Schwindt. A 20-channel magnetoencephalography system based on optically pumped magnetometers. *Physics in Medicine & Biology*, 62(23):8909, 2017.

[13] Elena Boto, Richard Bowtell, Peter Krüger, T Mark Fromhold, Peter G Morris, Sofie S Meyer, Gareth R Barnes, and Matthew J Brookes. On the potential of a new generation of magnetometers for meg: a beamformer simulation study. *PLoS One*, 11(8):e0157655, 2016.

[14] Elena Boto, Sofie S Meyer, Vishal Shah, Orang Alem, Svenja Knappe, Peter Kruger, T Mark Fromhold, Mark Lim, Paul M Glover, Peter G Morris, et al. A new generation of magnetoencephalography: Room temperature measurements using optically-pumped magnetometers. *NeuroImage*, 149:404–414, 2017.

[15] Elena Boto, Zelekha A Seedat, Niall Holmes, James Leggett, Ryan M Hill, Gillian Roberts, Vishal Shah, T Mark Fromhold, Karen J Mullinger, Tim M Tierney, et al. Wearable neuroimaging: Combining and contrasting magnetoencephalography and electroencephalography. *NeuroImage*, 201:116099, 2019.

[16] RM Brannon. Rotation, reflection, and frame changes. In *Orthogonal Tensors in Computational Engineering Mechanics*. IOP Publishing, 2018.

[17] Christoph Braun. Magnetoencephalography: a method for the study of brain function in neurosurgery. *Zeitschrift fur Medizinische Physik*, 17(4):280–287, 2007.

[18] Matthew J Brookes, Elena Boto, Molly Rea, Vishal Shah, James Osborne, Niall Holmes, Ryan M Hill, James Leggett, Natalie Rhodes, and Richard Bowtell. Theoretical advantages of a triaxial optically pumped magnetometer magnetoencephalography system. *NeuroImage*, 236:118025, 2021.

[19] Steven L Brunton and J Nathan Kutz. *Data-driven science and engineering: Machine learning, dynamical systems, and control*. Cambridge University Press, 2022.

[20] Peter Businger and Gene H Golub. Linear least squares solutions by householder transformations. *Numerische Mathematik*, 7(3):269–276, 1965.

[21] Robert M Chapman, RJ Ilmoniemi, So Barbanera, and GL Romani. Selective localization of alpha brain activity with neuromagnetic measurements. *Electroencephalography and clinical neurophysiology*, 58(6):569–572, 1984.

[22] Emily Clark, Travis Askham, Steven L Brunton, and J Nathan Kutz. Greedy sensor placement with cost constraints. *IEEE Sens. J.*, 19(7):2642–2656, 2018.

[23] Emily Clark, J Nathan Kutz, and Steven L Brunton. Sensor selection with cost constraints for dynamically relevant bases. *IEEE Sens. J.*, 20(19):11674–11687, 2020.

[24] David Cohen. Magnetoencephalography: detection of the brain's electrical activity with a superconducting magnetometer. *Science*, 175(4022):664–666, 1972.

[25] Keith S Cover, Jeroen PA Verbunt, Jan C de Munck, and Bob W van Dijk. Fitting a single equivalent current dipole model to meg data with exhaustive search optimization

is a simple, practical and very robust method given the speed of modern computers. In *International Congress Series*, volume 1300, pages 121–124. Elsevier, 2007.

[26] André Dachwitz. Accurate methods to compute the meg forward problem. Master's thesis, University of Münster, 2019.

[27] Moritz Dannhauer, Benjamin Lanfer, Carsten H Wolters, and Thomas R Knösche. Modeling of the human skull in eeg source analysis. *Human brain mapping*, 32(9):1383–1399, 2011.

[28] G Dassios, AS Fokas, and F Kariotou. On the non-uniqueness of the inverse meg problem. *Inverse Problems*, 21(2):L1, 2005.

[29] George Dassios and AS Fokas. The definite non-uniqueness results for deterministic eeg and meg data. *Inverse Problems*, 29(6):065012, 2013.

[30] JC De Munck. A linear discretization of the volume conductor boundary integral equation using analytically integrated elements (electrophysiology application). *IEEE Transactions on Biomedical Engineering*, 39(9):986–990, 1992.

[31] JC De Munck, Carsten H Wolters, and Maureen Clerc. Eeg and meg: forward modeling. *Handbook of neural activity measurement*, 19:192–248, 2012.

[32] Brian M de Silva, Krithika Manohar, Emily Clark, Bingni W Brunton, Steven L Brunton, and J Nathan Kutz. Pysensors: A python package for sparse sensor placement. *arXiv preprint arXiv:2102.13476*, 2021.

[33] Zlatko Drmac and Serkan Gugercin. A new selection operator for the discrete empirical interpolation method—improved a priori error bound and extensions. *SISC*, 38(2):A631–A648, 2016.

[34] Daniel Dumitru and John C King. Far-field potential production by quadrupole

generators in cylindrical volume conductors. *Electroencephalography and Clinical Neurophysiology/Evoked Potentials Section*, 88(5):421–431, 1993.

[35] Carl Eckart and Gale Young. The approximation of one matrix by another of lower rank. *Psychometrika*, 1(3):211–218, 1936.

[36] Brenden P Epps and Eric M Krivitzky. Singular value decomposition of noisy data: noise filtering. *Exp. Fluids*, 60(8):1–23, 2019.

[37] N Benjamin Erichson, Steven L Brunton, and J Nathan Kutz. Compressed dynamic mode decomposition for background modeling. *Journal of Real-Time Image Processing*, 16(5):1479–1492, 2019.

[38] N Benjamin Erichson, Sergey Voronin, Steven L Brunton, and J Nathan Kutz. Randomized matrix decompositions using r. *arXiv preprint arXiv:1608.02148*, 2016.

[39] A Steward Ferguson and Gerhard Stroink. Factors affecting the accuracy of the boundary element method in the forward problem. i. calculating surface potentials. *IEEE Transactions on Biomedical engineering*, 44(11):1139–1155, 1997.

[40] AS Ferguson, Xu Zhang, and Gerhard Stroink. A complete linear discretization for calculating the magnetic field using the boundary element method. *IEEE transactions on biomedical engineering*, 41(5):455–460, 1994.

[41] Marco Ferrari and Valentina Quaresima. A brief review on the history of human functional near-infrared spectroscopy (fnirs) development and fields of application. *Neuroimage*, 63(2):921–935, 2012.

[42] Gerald Fischer, Bernhard Tilg, Robert Modre, Friedrich Hanser, Bernd Messnarz, and Paul Wach. On modeling the wilson terminal in the boundary and finite element method. *IEEE Transactions on Biomedical Engineering*, 49(3):217–224, 2002.

[43] AS Fokas. Electro–magneto-encephalography for a three-shell model: distributed current in arbitrary, spherical and ellipsoidal geometries. *Journal of The Royal Society Interface*, 6(34):479–488, 2009.

[44] AS Fokas, IM Gel-Fand, and Y Kurylev. Inversion method for magnetoencephalography. *Inverse Problems*, 12(3):L9, 1996.

[45] AS Fokas and Y Kurylev. Electro-magneto-encephalography for the three-shell model: minimal l2-norm in spherical geometry. *Inverse Problems*, 28(3):035010, 2012.

[46] AS Fokas, Y Kurylev, and V Marinakis. The unique determination of neuronal currents in the brain via magnetoencephalography. *Inverse Problems*, 20(4):1067, 2004.

[47] Matan Gavish and David L Donoho. The optimal hard threshold for singular values is $4/\sqrt{3}$. *IEEE Trans. Inf. Theory*, 60(8):5040–5053, 2014.

[48] Nevzat G Gençer and I Oguz Tanzer. Forward problem solution of electromagnetic source imaging using a new bem formulation with high-order elements. *Physics in Medicine & Biology*, 44(9):2275, 1999.

[49] David B Geselowitz. On bioelectric potentials in an inhomogeneous volume conductor. *Biophysical journal*, 7(1):1–11, 1967.

[50] Gary H Glover. Overview of functional magnetic resonance imaging. *Neurosurgery Clinics*, 22(2):133–139, 2011.

[51] Daniel M Goldenholz, Seppo P Ahlfors, Matti S Hämäläinen, Dahlia Sharon, Mamiko Ishitobi, Lucia M Vaina, and Steven M Stufflebeam. Mapping the signal-to-noise-ratios of cortical sources in magnetoencephalography and electroencephalography. *Human brain mapping*, 30(4):1077–1086, 2009.

[52] Gene H Golub and Charles F Van Loan. *Matrix computations*. JHU press, 2013.

[53] Alexandre Gramfort, Martin Luessi, Eric Larson, Denis A Engemann, Daniel Strohmeier, Christian Brodbeck, Roman Goj, Mainak Jas, Teon Brooks, Lauri Parkkonen, et al. Meg and eeg data analysis with mne-python. *Frontiers in neuroscience*, page 267, 2013.

[54] Alexandre Gramfort, Martin Luessi, Eric Larson, Denis A Engemann, Daniel Strohmeier, Christian Brodbeck, Lauri Parkkonen, and Matti S Hämäläinen. Mne software for processing meg and eeg data. *Neuroimage*, 86:446–460, 2014.

[55] David J Griffiths. *Introduction to Electrodynamics, Fourth Edition*. Cambridge University Press, 2017.

[56] Flavio Grynszpan and David B Geselowitz. Model studies of the magnetocardiogram. *Biophysical journal*, 13(9):911–925, 1973.

[57] Sravan Gudivada and Adrian G Bors. Face recognition using ortho-diffusion bases. In *2012 Proceedings of the 20th European Signal Processing Conference (EUSIPCO)*, pages 1578–1582. IEEE, 2012.

[58] Hendra Gunawan, Oki Neswan, and Wono Setya-Budhi. A formula for angles between subspaces of inner product spaces. *Beiträge zur Algebra und Geometrie*, 46(2):311–320, 2005.

[59] Matti Hämäläinen, Riitta Hari, Risto J Ilmoniemi, Jukka Knuutila, and Olli V Lounasmaa. Magnetoencephalography—theory, instrumentation, and applications to noninvasive studies of the working human brain. *Reviews of modern Physics*, 65(2):413, 1993.

[60] Matti S Hämäläinen and Risto J Ilmoniemi. Interpreting magnetic fields of the brain: minimum norm estimates. *Medical & biological engineering & computing*, 32(1):35–42, 1994.

[61] Matti S Hamalainen and Jukka Sarvas. Realistic conductivity geometry model of the human head for interpretation of neuromagnetic data. *IEEE transactions on biomedical engineering*, 36(2):165–171, 1989.

[62] Riitta Hari, Sylvain Baillet, Gareth Barnes, Richard Burgess, Nina Forss, Joachim Gross, Matti Hämäläinen, Ole Jensen, Ryusuke Kakigi, François Mauguière, et al. Ifcn-endorsed practical guidelines for clinical magnetoencephalography (meg). *Clinical Neurophysiology*, 129(8):1720–1747, 2018.

[63] Riitta Hari and Aina Puce. *MEG-EEG Primer*. Oxford University Press, 2017.

[64] I Hashimoto, T Mashiko, T Mizuta, T Imada, K Iwase, and H Okazaki. Visualization of a moving quadrupole with magnetic measurements of peripheral nerve action fields. *Electroencephalography and Clinical Neurophysiology/Evoked Potentials Section*, 93(6):459–467, 1994.

[65] Jens Haueisen, Ceon Ramon, Michael Eiselt, Hartmut Brauer, and Hannes Nowak. Influence of tissue resistivities on neuromagnetic fields and electric potentials studied with a finite element model of the head. *IEEE Transactions on Biomedical Engineering*, 44(8):727–735, 1997.

[66] H von Helmholtz. Ueber einige gesetze der vertheilung elektrischer ströme in körperlichen leitern, mit anwendung auf die thierisch-elektrischen versuche (schluss.). *Annalen der Physik*, 165(7):353–377, 1853.

[67] Suzana Herculano-Houzel. The human brain in numbers: a linearly scaled-up primate brain. *Frontiers in human neuroscience*, page 31, 2009.

[68] Suzana Herculano-Houzel. The remarkable, yet not extraordinary, human brain as a scaled-up primate brain and its associated cost. *Proceedings of the National Academy of Sciences*, 109(supplement_1):10661–10668, 2012.

[69] EL Hill. The theory of vector spherical harmonics. *American Journal of Physics*, 22(4):211–214, 1954.

[70] Ryan M Hill, Elena Boto, Molly Rea, Niall Holmes, James Leggett, Laurence A Coles, Manolis Papastavrou, Sarah K Everton, Benjamin AE Hunt, Dominic Sims, et al. Multi-channel whole-head opm-meg: Helmet design and a comparison with a conventional system. *NeuroImage*, 219:116995, 2020.

[71] EW Hobson. On bessel's functions, and relations connecting them with hyper-spherical and spherical harmonics. *Proceedings of the London Mathematical Society*, 1(1):49–75, 1893.

[72] Bertrand Hochwald and Arye Nehorai. Magnetoencephalography with diversely oriented and multicomponent sensors. *IEEE transactions on biomedical engineering*, 44(1):40–50, 1997.

[73] Joonas Iivanainen, Antti J Mäkinen, Rasmus Zetter, Matti Stenroos, Risto J Ilmoniemi, and Lauri Parkkonen. Spatial sampling of meg and eeg based on generalized spatial-frequency analysis and optimal design. *NeuroImage*, 245:118747, 2021.

[74] Joonas Iivanainen, Matti Stenroos, and Lauri Parkkonen. Measuring meg closer to the brain: Performance of on-scalp sensor arrays. *NeuroImage*, 147:542–553, 2017.

[75] Joonas Iivanainen, Rasmus Zetter, Mikael Grön, Karoliina Hakkarainen, and Lauri Parkkonen. On-scalp meg system utilizing an actively shielded array of optically-pumped magnetometers. *NeuroImage*, 194:244–258, 2019.

[76] Risto J Ilmoniemi. The triangle phantom in magnetoencephalography. *J Jpn Biomagn Bioelectromagn Soc*, 22:44–5, 2009.

[77] Risto J Ilmoniemi and Jukka Sarvas. *Brain signals: Physics and mathematics of MEG and EEG*. Mit Press, 2019.

[78] RJ Ilmoniemi. The forward and inverse problems in the spherical model. *Biomagnetism: applications & theory*, 1985.

[79] Andreas A Ioannides. Magnetoencephalography (meg). In *Dynamic Brain Imaging*, pages 167–188. Springer, 2009.

[80] John David Jackson. Classical electrodynamics, 1999.

[81] Dieter Jaeger and Ranu Jung. *Encyclopedia of computational neuroscience*. Springer, 2015.

[82] Mainak Jas, Stephanie R Jones, and Matti S Hämäläinen. Whole-head opm-meg enables noninvasive assessment of functional connectivity. *Trends in Neurosciences*, 44(7):510–512, 2021.

[83] Balaji Jayaraman and SM Mamun. On data-driven sparse sensing and linear estimation of fluid flows. *Sensors*, 20(13):3752, 2020.

[84] GB Jeffery. The relations between spherical, cylindrical, and spheroidal harmonics. *Proceedings of the London Mathematical Society*, 2(1):133–139, 1917.

[85] Cort N Johnson, PDD Schwindt, and M Weisend. Multi-sensor magnetoencephalography with atomic magnetometers. *Physics in Medicine & Biology*, 58(17):6065, 2013.

[86] Jukka ET Kajola, Juha T Simola, and Visa A Vilkman. Sampling theory for neuromagnetic detector arrays. *IEEE Transactions on Biomedical Engineering*, 40(0):859, 1993.

[87] Keigo Kamada, Daichi Sato, Yosuke Ito, Hiroaki Natsukawa, Kazuhisa Okano, Natsuhiko Mizutani, and Tetsuo Kobayashi. Human magnetoencephalogram measurements using newly developed compact module of high-sensitivity atomic magnetometer. *Japanese Journal of Applied Physics*, 54(2):026601, 2015.

[88] PK Kemppainen and RJ Ilmoniemi. Channel capacity of multichannel magnetometers. In *Advances in biomagnetism*, pages 635–638. Springer, 1989.

[89] Leslie Gordon Kiloh, Alan J McComas, and John Walkinshaw Osselton. *Clinical electroencephalography*. Butterworth-Heinemann, 2013.

[90] Kiwoong Kim, Samo Begus, Hui Xia, Seung-Kyun Lee, Vojko Jazbinsek, Zvonko Trontelj, and Michael V Romalis. Multi-channel atomic magnetometer for magnetoencephalography: A configuration study. *NeuroImage*, 89:143–151, 2014.

[91] Reinhold Kleiner, Dieter Koelle, Frank Ludwig, and John Clarke. Superconducting quantum interference devices: State of the art and applications. *Proceedings of the IEEE*, 92(10):1534–1548, 2004.

[92] Svenja Knappe, Tilmann Sander, and Lutz Trahms. Optically-pumped magnetometers for meg. In *Magnetoencephalography*, pages 993–999. Springer, 2014.

[93] J Nathan Kutz. *Data-driven modeling & scientific computation: methods for complex systems & big data*. Oxford University Press, 2013.

[94] Benjamin Lanfer, Michael Scherg, Moritz Dannhauer, Thomas R Knösche, Martin Burger, and Carsten H Wolters. Influences of skull segmentation inaccuracies on eeg source analysis. *NeuroImage*, 62(1):418–431, 2012.

[95] Christopher Laohathai, John S Ebersole, John C Mosher, Anto I Bagić, Ai Sumida, Gretchen Von Allmen, and Michael E Funke. Practical fundamentals of clinical meg interpretation in epilepsy. *Frontiers in Neurology*, 12, 2021.

[96] Sarah Lloyd-Fox, Anna Blasi, and CE Elwell. Illuminating the developing brain: the past, present and future of functional near infrared spectroscopy. *Neuroscience & Biobehavioral Reviews*, 34(3):269–284, 2010.

[97] Nikos K Logothetis. What we can do and what we cannot do with fmri. *Nature*, 453(7197):869–878, 2008.

[98] Antti J Mäkinen, Rasmus Zetter, Joonas Iivanainen, Koos CJ Zevenhoven, Lauri Parkkonen, and Risto J Ilmoniemi. Magnetic-field modeling with surface currents. part i. physical and computational principles of bfieldtools. *Journal of Applied Physics*, 128(6):063906, 2020.

[99] Jaakko Malmivuo, Robert Plonsey, et al. *Bioelectromagnetism: principles and applications of bioelectric and biomagnetic fields*. Oxford University Press, USA, 1995.

[100] Krithika Manohar, Bingni W Brunton, J Nathan Kutz, and Steven L Brunton. Data-driven sparse sensor placement for reconstruction: Demonstrating the benefits of exploiting known patterns. *IEEE Control Syst.*, 38(3):63–86, 2018.

[101] Urban Marhl, Anna Jodko-Władzińska, Rüdiger Brühl, Tilmann Sander, and Vojko Jazbinšek. Transforming and comparing data between standard squid and opm-meg systems. *PloS One*, 17(1):e0262669, 2022.

[102] Kanta Matsuura and Yoichi Okabe. Selective minimum-norm solution of the biomagnetic inverse problem. *IEEE Transactions on Biomedical Engineering*, 42(6):608–615, 1995.

[103] Jason D McEwen and Yves Wiaux. A novel sampling theorem on the sphere. *IEEE Transactions on Signal Processing*, 59(12):5876–5887, 2011.

[104] Jan WH Meijs, Onno W Weier, Maria J Peters, and Adriaan Van Oosterom. On the numerical accuracy of the boundary element method (eeg application). *IEEE transactions on biomedical engineering*, 36(10):1038–1049, 1989.

[105] Philip M Morse and Herman Feshbach. Methods of theoretical physics. *American Journal of Physics*, 22(6):410–413, 1954.

[106] John C Mosher and Richard M Leahy. Recursive music: a framework for eeg and meg source localization. *IEEE Transactions on Biomedical Engineering*, 45(11):1342–1354, 1998.

[107] John C Mosher and Richard M Leahy. Source localization using recursively applied and projected (rap) music. *IEEE Transactions on signal processing*, 47(2):332–340, 1999.

[108] John C Mosher, Richard M Leahy, and Paul S Lewis. Eeg and meg: forward solutions for inverse methods. *IEEE Transactions on biomedical engineering*, 46(3):245–259, 1999.

[109] Gerd Muehllehner and Joel S Karp. Positron emission tomography. *Physics in Medicine & Biology*, 51(13):R117, 2006.

[110] Jukka Nenonen, Liisa Helle, Amit Jaiswal, Elizabeth Bock, Nicole Ille, and Harald Bornfleth. Sensitivity of a 29-channel meg source montage. *Brain Sci.*, 12(1):105, 2022.

[111] Jukka Nenonen, Samu Taulu, Matti Kajola, and Antti Ahonen. Total information extracted from meg measurements. In *International Congress Series*, volume 1300, pages 245–248. Elsevier, 2007.

[112] Guido Nolte, Thomas Fieseler, and Gabriel Curio. Perturbative analytical solutions of the magnetic forward problem for realistic volume conductors. *Journal of applied physics*, 89(4):2360–2369, 2001.

[113] Aapo Nummenmaa, Matti Stenroos, Risto J Ilmoniemi, Yoshio C Okada, Matti S Hämäläinen, and Tommi Raij. Comparison of spherical and realistically shaped boundary element head models for transcranial magnetic stimulation navigation. *Clinical Neurophysiology*, 124(10):1995–2007, 2013.

[114] Jussi Nurminen, Samu Taulu, Jukka Nenonen, Liisa Helle, Juha Simola, and Antti Ahonen. Improving meg performance with additional tangential sensors. *IEEE Transactions on Biomedical Engineering*, 60(9):2559–2566, 2013.

[115] John M Ollinger and Jeffrey A Fessler. Positron-emission tomography. *Ieee signal processing magazine*, 14(1):43–55, 1997.

[116] Wolfgang KH Panofsky and Melba Phillips. *Classical electricity and magnetism*. Courier Corporation, 2005.

[117] Roberto Domingo Pascual-Marqui et al. Standardized low-resolution brain electromagnetic tomography (sloreta): technical details. *Methods Find Exp Clin Pharmacol*, 24(Suppl D):5–12, 2002.

[118] William D Penny, Karl J Friston, John T Ashburner, Stefan J Kiebel, and Thomas E Nichols. *Statistical parametric mapping: the analysis of functional brain images*. Elsevier, 2011.

[119] Isaac Z Pesenson. Sampling, splines and frames on compact manifolds. *GEM-International Journal on Geomathematics*, 6(1):43–81, 2015.

[120] Dimitrios Piretzidis. Surface spherical harmonic functions visualization. https://www.mathworks.com/matlabcentral/fileexchange/44869-surface-spherical-harmonic-functions-visualization, 2022.

[121] Alain Plattner and Frederik J Simons. Spatiospectral concentration of vector fields on a sphere. *Applied and Computational Harmonic Analysis*, 36(1):1–22, 2014.

[122] Robert Plonsey. The nature of sources of bioelectric and biomagnetic fields. *Biophysical Journal*, 39(3):309–312, 1982.

[123] Bushra Riaz, Christoph Pfeiffer, and Justin F Schneiderman. Evaluation of realistic layouts for next generation on-scalp meg: spatial information density maps. *Sci. Rep.*, 7(1):1–12, 2017.

[124] Samantha Richerson, Mark Ingram, Danielle Perry, and Mark M Stecker. Classification of the extracellular fields produced by activated neural structures. *BioMedical Engineering OnLine*, 4(1):1–23, 2005.

[125] Yuji Saito, Taku Nonomura, Keigo Yamada, Kumi Nakai, Takayuki Nagata, Keisuke Asai, Yasuo Sasaki, and Daisuke Tsubakino. Determinant-based fast greedy sensor selection algorithm. *IEEE Access*, 9:68535–68551, 2021.

[126] TH Sander, J Preusser, R Mhaskar, J Kitching, L Trahms, and S Knappe. Magnetoencephalography with a chip-scale atomic magnetometer. *Biomedical optics express*, 3(5):981–990, 2012.

[127] Jukka Sarvas. Basic mathematical and electromagnetic concepts of the biomagnetic inverse problem. *Physics in Medicine & Biology*, 32(1):11, 1987.

[128] Michael Scherg. Fundamentals of dipole source potential analysis. *Auditory evoked magnetic fields and electric potentials. Advances in audiology*, 6(40-69):25, 1990.

[129] Heidi A Schlitt, L Heller, R Aaron, E Best, and DM Ranken. Evaluation of boundary element methods for the eeg forward problem: effect of linear interpolation. *IEEE transactions on biomedical engineering*, 42(1):52–58, 1995.

[130] Ralph Schmidt. Multiple emitter location and signal parameter estimation. *IEEE transactions on antennas and propagation*, 34(3):276–280, 1986.

[131] Olaf Sporns. *Networks of the Brain*. MIT press, 2016.

[132] Ramesh Srinivasan, Don M Tucker, and Michael Murias. Estimating the spatial nyquist of the human eeg. *Behavior Research Methods, Instruments, & Computers*, 30(1):8–19, 1998.

[133] Matti Stenroos. The transfer matrix for epicardial potential in a piece-wise homogeneous

thorax model: the boundary element formulation. *Physics in Medicine & Biology*, 54(18):5443, 2009.

[134] Matti Stenroos and Olaf Hauk. Minimum-norm cortical source estimation in layered head models is robust against skull conductivity error. *NeuroImage*, 81:265–272, 2013.

[135] Matti Stenroos, Alexander Hunold, and Jens Haueisen. Comparison of three-shell and simplified volume conductor models in magnetoencephalography. *Neuroimage*, 94:337–348, 2014.

[136] Matti Stenroos, Ville Mäntynen, and Jukka Nenonen. A matlab library for solving quasi-static volume conduction problems using the boundary element method. *Computer methods and programs in biomedicine*, 88(3):256–263, 2007.

[137] Matti Stenroos and Aapo Nummenmaa. Incorporating and compensating cerebrospinal fluid in surface-based forward models of magneto-and electroencephalography. *PLoS One*, 11(7):e0159595, 2016.

[138] Gilbert Stewart and Ji-guang Sun. *Matrix perturbation theory*. Academic Press, 1990.

[139] Greg Stuart, Nelson Spruston, Bert Sakmann, and Michael Häusser. Action potential initiation and backpropagation in neurons of the mammalian cns. *Trends in neurosciences*, 20(3):125–131, 1997.

[140] M Stuart Lynn and William P Timlake. The numerical solution of singular integral equations of potential theory. *Numerische Mathematik*, 11(1):77–98, 1968.

[141] François Tadel, Sylvain Baillet, John C Mosher, Dimitrios Pantazis, and Richard M Leahy. Brainstorm: a user-friendly application for meg/eeg analysis. *Comput. Intell. Neurosci.*, 2011, 2011.

[142] Samu Taulu and Matti Kajola. Presentation of electromagnetic multichannel data: the signal space separation method. *Journal of Applied Physics*, 97(12):124905, 2005.

[143] Samu Taulu and Eric Larson. Unified expression of the quasi-static electromagnetic field: Demonstration with meg and eeg signals. *IEEE Transactions on Biomedical Engineering*, 68(3):992–1004, 2020.

[144] Samu Taulu, Juha Simola, and Matti Kajola. Applications of the signal space separation method. *IEEE Trans. Signal Process.*, 53(9):3359–3372, 2005.

[145] Michal Teplan et al. Fundamentals of eeg measurement. *Measurement science review*, 2(2):1–11, 2002.

[146] Tim M Tierney, Niall Holmes, Stephanie Mellor, José David López, Gillian Roberts, Ryan M Hill, Elena Boto, James Leggett, Vishal Shah, Matthew J Brookes, et al. Optically pumped magnetometers: From quantum origins to multi-channel magnetoencephalography. *NeuroImage*, 199:598–608, 2019.

[147] Tim M Tierney, Stephanie Mellor, George C O'Neill, Niall Holmes, Elena Boto, Gillian Roberts, Ryan M Hill, James Leggett, Richard Bowtell, Matthew J Brookes, et al. Pragmatic spatial sampling for wearable meg arrays. *Scientific reports*, 10(1):1–11, 2020.

[148] Lloyd N Trefethen and David Bau III. *Numerical linear algebra*, volume 50. SIAM, 1997.

[149] Sylvain Vallaghé and Maureen Clerc. A global sensitivity analysis of three-and four-layer eeg conductivity models. *IEEE Transactions on Biomedical Engineering*, 56(4):988–995, 2008.

[150] Adriaan Van Oosterom and Jan Strackee. The solid angle of a plane triangle. *IEEE transactions on Biomedical Engineering*, BME-30(2):125–126, 1983.

[151] Barry D Van Veen and Kevin M Buckley. Beamforming: A versatile approach to spatial filtering. *IEEE assp magazine*, 5(2):4–24, 1988.

[152] Barry D Van Veen, Wim Van Drongelen, Moshe Yuchtman, and Akifumi Suzuki. Localization of brain electrical activity via linearly constrained minimum variance spatial filtering. *IEEE Transactions on biomedical engineering*, 44(9):867–880, 1997.

[153] Dmitriĭ Aleksandrovich Varshalovich, Anatolij Nikolaevič Moskalev, and Valerii Kel'manovich Khersonskii. *Quantum theory of angular momentum*. World Scientific, 1988.

[154] Johannes Vorwerk, Jae-Hyun Cho, Stefan Rampp, Hajo Hamer, Thomas R Knösche, and Carsten H Wolters. A guideline for head volume conductor modeling in eeg and meg. *NeuroImage*, 100:590–607, 2014.

[155] J Vrba, SE Robinson, and J McCubbin. How many channels are needed for meg? *NCN*, 2004:99–99, 2004.

[156] John P Wikswo. Biomagnetic sources and their models. In *Advances in biomagnetism*, pages 1–18. Springer, 1989.

[157] H Xia, Andrei Ben-Amar Baranga, D Hoffman, and MV Romalis. Magnetoencephalography with an atomic magnetometer. *Applied Physics Letters*, 89(21):211104, 2006.

[158] Wan-Jin Yeo, Yao-Rui Yeo, and Samu Taulu. Towards analytical calculation of the magnetic flux measured by magnetometers. *Physics Letters A*, 411:127545, 2021.

[159] Andrew Zangwill. *Modern electrodynamics*. Cambridge University Press, 2013.

[160] Rasmus Zetter, Joonas Iivanainen, Matti Stenroos, and Lauri Parkkonen. Requirements for coregistration accuracy in on-scalp meg. *Brain Topogr.*, 31(6):931–948, 2018.

[161] Peng Zheng, Travis Askham, Steven L Brunton, J Nathan Kutz, and Aleksandr Y Aravkin. A unified framework for sparse relaxed regularized regression: Sr3. *IEEE Access*, 7:1404–1423, 2018.